INTERFERENCE MITIGATION EFFECTS ON SYNTHETIC APERTURE RADAR COHERENT DATA PRODUCTS

By

CAMERON H MUSGROVE

Bachelor of Science in Electrical Engineering
Oklahoma State University
Stillwater, OK
2005

Master of Science in Electrical Engineering
Oklahoma State University
Stillwater, OK
2007

Submitted to the Faculty of the
Graduate College of
Oklahoma State University
in partial fulfillment of
the requirements for
the Degree of
DOCTOR OF PHILOSOPHY
July, 2015

INTERFERENCE MITIGATION EFFECTS ON SYNTHETIC APERTURE RADAR COHERENT DATA PRODUCTS

Dissertation Approved:

Dr. James C. West

Dissertation Advisor

Dr. Charles F. Bunting

Dr. George Scheets

Dr. Daqing Piao

Dr. Andrew Arena

Dr. Richard Naething

ACKNOWLEDGMENTS

To my wife whose love and support made this possible, thank you and I love you. To my children, some day I hope you recognize the value in this work. I'm thankful for the support of my extended family, especially my grandad, who has always encouraged me to advance my education.

I thank my advisor, James West for always making time for me and encouraging me through this journey. I thank my manager, Bill Hensley, for helping me find the intersection of business and educational goals, and for maintaining a work environment to complete this work. I thank the Sandia University Part-Time program, especially Bernadette Montano, for supporting classwork and the ground work for selecting a topic. I thank Bill Hensley, Rusty Escapule, Richard Ormesher, Jason Payne, and Adam Tanuz for financial and programmatic support of this topic. I am thankful for the many fruitful discussions with very talented colleagues: Doug Bickel, Richard Ormesher, David Gentry, John Schilling, Ann Raynal, David Harmony, Robert Riley, Derek Tucker, Doug Thompson, and Armin Doerry. I am grateful for Richard Naething who provided encouragement, a sounding board for ideas, and served on my committee. And I thank my committee for their time and insightful comments.

This work was supported in part by the Laboratory Directed Research and Development program at Sandia National Laboratories, a multi-program laboratory managed and operated by Sandia Corporation, a wholly owned subsidiary of Lockheed Martin Corporation, for the U.S. Department of Energy's National Nuclear Security Administration under contract DE-AC04-94AL85000.

Name: CAMERON MUSGROVE

Date of Degree: JULY, 2015

Title of Study: INTERFERENCE MITIGATION EFFECTS ON SYNTHETIC APERTURE RADAR COHERENT DATA PRODUCTS

Major Field: ELECTRICAL ENGINEERING

Abstract:

Both radio frequency interference from sources external to the synthetic aperture radar system and techniques to mitigate radio frequency interference can degrade the quality of the image products. Often it is the second order data products derived from the images that are of the most value for a synthetic aperture radar system. Preserving the quality of these data products, in the presence of radio frequency interference, is paramount to maintaining the utility of the sensor.

This dissertation examines the effects of interference mitigation upon coherent data products of fine-resolution, high frequency synthetic aperture radars using stretch processing. Novel interference mitigation techniques are introduced that operate on single or multiple apertures of data that increase average coherence compared to existing techniques. A novel contrast metric is combined with existing image quality and average coherence metrics to compare multiple mitigation techniques. The characteristics of interference mitigation techniques that restore coherence are revealed.

TABLE OF CONTENTS

LIST OF FIGURES

Figure Page

LIST OF TABLES

Table Page

ACRONYMS

A/D analog to digital

CCD coherent change detection

CDF cumulative distribution function

CPI coherent processing interval

CWGN circular white Gaussian noise

DEM digital elevation model

IF intermediate frequency

IFSAR interferometric SAR

IPR impulse response

ISLR integrated sidelobe ratio

LFM linear frequency-modulated

LMS least-mean-square

MLE maximum likelihood estimator

PDF probability density function

PSLL peak sidelobe level

RCS radar cross-section

RF radio frequency

RFI radio frequency interference

ROC receiver operating characteristic

RVPE residual video phase error

SAR synthetic aperture radar

SINR signal-to-interference-plus-noise ratio

SIR signal-to-interference ratio

SNR signal-to-noise ratio

CHAPTER 1

INTRODUCTION

There are many possible sources of radio frequency (RF) interference for a radar system. This dissertation addresses unintentional RF emissions within the receiving bandwidth of a synthetic aperture radar. Fine-resolution synthetic aperture radar (SAR) systems require large amounts of bandwidth, e.g. 1GHz of bandwidth is required for 6 inch resolution. Bandwidth is a finite resource allocated by government agencies such as the NTIA and FCC in the United States. Typically radar systems can find large, contiguous frequency allocations at higher radar bands, such as X, Ku, and Ka, but in the future finding large, uninterrupted frequency bands, even at higher frequency radar bands may not be possible. To support increasing wireless data demands from a growing number of users, cell phone communications providers have been researching applications at higher frequencies, specifically 28GHz [1]. The public need for more bandwidth has created pressure upon the US Department of Defense to reduce their bandwidth allocations [2]. This means that as the military acquires more wireless systems, these systems will be required to cooperatively share spectrum or avoid interference with other military and civilian systems [3]. Therefore, it is expected in the future that RF systems, including intelligence and surveillance systems such as SAR, must be prepared to continue producing data products in the presence of interference. While much work has been done towards removing interference from SAR images, this dissertation seeks to preserve the unique characteristics of coherent data products that enable creation of elevation maps and change detection products.

RF interference can be very damaging to SAR data, particularly if the SAR system produces a coherent data product derived from SAR images. SAR images are not the same

as optical images and require some level of training to interpret, but the images can be coherently processed into very accurate height maps through interferometric SAR (IFSAR) processing, or into other products that have more utility than an optical image. IFSAR processing requires a high coherence between two images to reduce or limit errors in the height map [4]. RF interference can lower the coherence such that height maps cannot be produced from the data, and in some cases the interference mitigation technique itself can also lower the coherence.

Low frequency SAR systems (e.g. UHF band) have overcome RF interference issues [5–7], however these systems have different characteristics and requirements than a fine-resolution, high frequency (e.g. Ku band) SAR producing IFSAR and coherent change detection (CCD) products. One distinguishing characteristic is the structure of the interference signal within the radar data as a result of using stretch processing is much different than if the received data had been directly sampled. The structure of the interference signal can be key to detecting and removing it from the radar data. Another difference between low and high frequency systems is the terrain radar cross-section (RCS) characteristics require unique quality metrics for each frequency range. For example, at UHF band the scattering characteristics of grass is not observable in the same way as it is for Ku band because the features of the grass are much smaller than the UHF wavelength.

This dissertation examines the impact of interference mitigation techniques upon the coherence for a fine-resolution, single channel Ku band SAR, using stretch processing to produce coherent data products by making repeat collections at the same geometry.

1.1 Overview

This dissertation first provides background material on synthetic aperture radars, interference effects, and coherence. Then a review of existing interference mitigation approaches and the effects upon second order coherent data products are shown. Next, novel performance metrics are explained in detail that will be used throughout the dissertation to

compare the performance between different mitigation techniques.

Properly comparing different mitigation techniques requires some amount of similarity between each technique. An equalization mitigation method is presented that varies performance according to interference signal power. Whereas the performance of other mitigation methods in this dissertation depend upon interference signal bandwidth. Because of this difference, the equalization mitigation method is presented in its own chapter.

Because this dissertation assumes that multiple passes of a single channel radar are used to create second order coherent data products, interference mitigation algorithms can be restricted to either using a single pass of data or can use multiple passes. Therefore, interference mitigation algorithms are organized into separate chapters for single aperture and multiple aperture techniques. Typically the literature only considers the single aperture mitigation case. However, using multiple apertures can yield an average coherence increase for many cases.

CHAPTER 2

BACKGROUND

In this chapter the basic concepts of a synthetic aperture radar (SAR) are explained from range and cross-range resolution to coherence. These concepts are used throughout this document to define the characteristics of a fine-resolution, stretch processing synthetic aperture radar capable of producing coherent data products. The characteristics of the radar greatly influence the type of interference mitigation that can be applied (chapter 3), and help to understand the relevant performance metrics (chapter 4) used to compare interference mitigation techniques.

This chapter begins by discussing range and cross-range resolution for a spotlight mode synthetic aperture radar. Then linear frequency-modulated (LFM) waveform and stretch processing concepts are discussed followed by the deskew correction that repairs errors associated with using the LFM waveform with stretch processing. Next, basic performance characteristics for a SAR radar are discussed that include impulse response, noise equivalent reflectivity, and coherence. Finally, a model for RF interference is presented to make clear the effects stretch processing can have upon interference within SAR data.

2.1 Synthetic Aperture Radar

Within this section some basic concepts of radar and SAR are explained to clearly define the parameters of the SAR system modeled within this dissertation. Not all SAR systems follow these system design parameters, or nomenclature, as there are many possible implementations and variations.

A radar in its simplest description radiates microwave energy and receives the reflected

energy to measure the range of the object that reflected that energy. The radar can only measure range by comparing the time between transmitting energy and receiving energy; this is called the range dimension because the time difference measured indicates the range of a target from the radar. For many pulsed radar systems, the radar transmits a pulse, then receives the reflected pulse for a particular interval of time, and repeats. If the radar moves orthogonal to the range dimension between each interval, another dimension becomes available to resolve the location of targets; typically this is called the cross-range dimension because it is orthogonal to the range dimension. Many airborne SAR systems fly in one direction and point the radar to either side of the aircraft to obtain 2D information of targets. Likewise, adding another dimension of movement, such as collecting data at different heights, will create another dimension (e.g. height) with which to resolve the target.

A synthetic aperture radar (SAR) is a radar that creates a 2D representation (i.e. image) of the reflected energy over an area. In this way the source of the reflected energy is localized in space and represented accordingly in the image product. SAR images are made of both terrain and objects on the terrain; each has unique reflected energy characteristics. The interpretation of SAR images is determined by the scattering characteristics of the frequencies the radar used to collect the data. Fine-resolution, high frequency images are typically easier to interpret because small wavelengths interact and scatter with objects in a similar process to optical wavelengths. The quality of SAR images is determined by many factors of the radar system hardware and processing, but resolution is extremely important.

Resolution in the range dimension of a radar is the minimum distance between two targets for which it is still possible to distinguish the response from each other [8]. The range resolution, ρ_r, is mathematically determined by the pulse envelope (duration) τ and the speed of light as [8, 9]

$$\rho_r = \frac{c\tau}{2} \tag{2.1}$$

For a constant frequency pulsed radar, the bandwidth, BW, is defined as the inverse of the

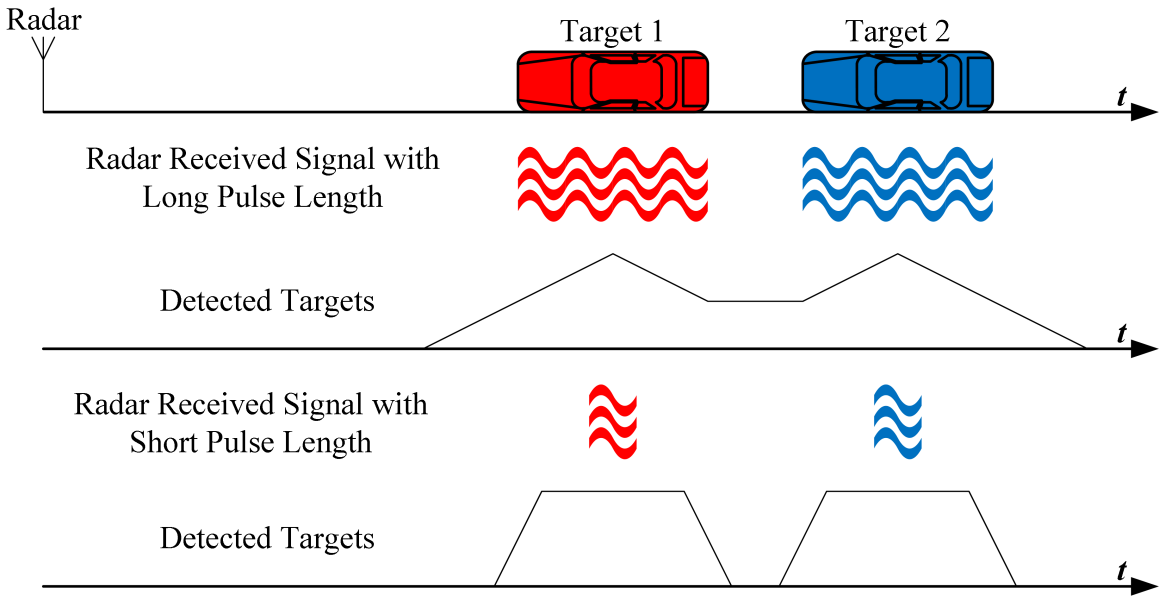

Figure 2.1: Range resolution determined by pulse length. The longer pulse is not able to clearly distinguish the two targets, while the shorter pulse is able to distinguish between two targets.

pulse envelope duration, $BW = 1/\tau$ [8]. The only factor that determines range resolution is the bandwidth of the received pulse; not the range to the target or the center frequency of the radar [9]. For example, Figure 2.1 illustrates the target resolving ability of a constant frequency pulsed radar for a both a short and long pulse duration; clearly the shorter pulse yields better distinction between targets. Notice for the constant frequency pulsed radar example in Figure 2.1, time and bandwidth are coupled such that a small pulse time is required for high bandwidth. The small time duration of the pulse limits the amount of signal power, reducing the sensitivity of the radar system. Typically, SAR systems use a pulse modulation technique to separate time and bandwidth so signal power is limited by bandwidth; this will be explained in a later section.

Without synthetic aperture processing, the radar's cross-range resolution is limited to its antenna beamwidth, β, much in the same way the size of a lens limits the resolving power of an optical system. Like range resolution, the cross-range resolution, ρ_a, is the minimum distance between targets for which the radar beam can isolate one target's echo response from the other target. Throughout this document the term 'azimuth' is used interchangeably

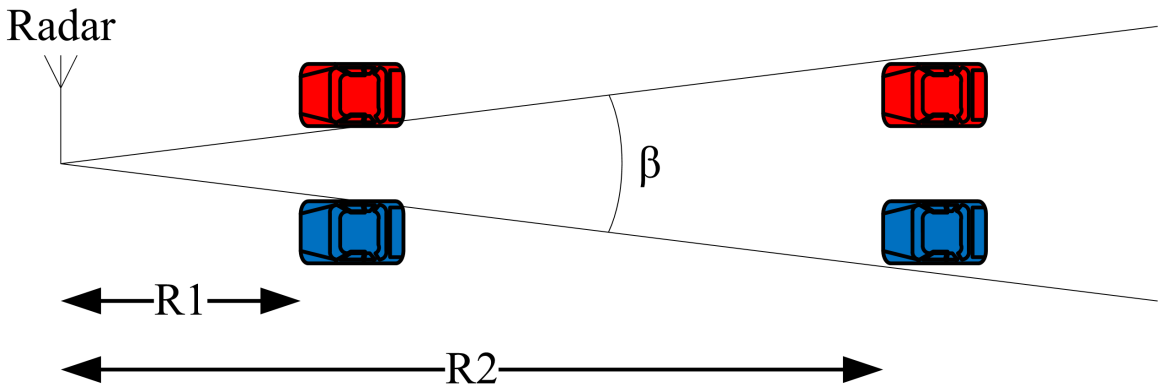

Figure 2.2: Cross-range resolution determined by radar beamwidth. Although the distance between each target is the same at both distances R1 and R2, at distance R1 the beam is able to distinguish the targets, while at distance R2 the beam is unable to distinguish an absence between the targets.

with 'cross-range'. The radar's antenna beam, much like a flashlight, expands over distance (range), r, and the resolution coarsens according to the simple expression [8]

$$\rho_a = 2r \sin\left(\frac{\beta}{2}\right). \tag{2.2}$$

Figure 2.2 illustrates the width of the antenna beam at a particular range must be able to uniquely illuminate one target from another to resolve separate targets. However, because radar wavelengths are much longer than visible light wavelengths, the size of a microwave antenna for a real-beam radar must be much larger than optical lenses for modest resolution. In most cases the physical size of a microwave antenna for fine-resolution will be larger than what is practical to build or fly on an airborne platform. Nominally, the 3dB beamwidth of an antenna, β, is related to its physical size, D, by the wavelength λ according to [10],

$$\beta \sim 0.89\frac{\lambda}{D}. \tag{2.3}$$

Inserting (2.3) into (2.2) results in the expression

$$\rho_a = 2r \sin\left(\frac{0.89\lambda}{2D}\right), \tag{2.4}$$

$$\rho_a \approx \frac{r\lambda}{D}, \tag{2.5}$$

where it is evident that the cross-range resolution is directly proportional to range and wavelength, and it is inversely proportional to the physical size of the antenna. Using (2.4), 6 inch cross-range resolution at 5 km distance and at Ku band (16.8GHz) would require an antenna aperture size of 1 km!

A synthetic aperture radar is named so because through signal processing it synthesizes a much larger antenna from many measurements made with a smaller antenna. The radar collects samples for a specific length along a path in space (called a synthetic aperture length) and makes adjustments to the phase of the data to synthesize a much larger aperture than the real antenna is capable of resolving. An important result from synthetic aperture radar processing is that cross-range resolution is no longer dependent upon range; it now only depends upon the length of the synthetic aperture collected at a particular range. Many details of SAR processing can be found in the literature such as [8–10].

A stripmap mode SAR collects data along a straight-line path while the antenna is locked to an angle perpendicular to the direction of travel. For this mode, cross-range resolution is limited by the antenna's beamwidth because the target is illuminated by the radar only while it is within the antenna's beamwidth. (Otherwise, there is no signal from objects outside the radar's beam.) In this collection geometry, resolution does not depend on range because the synthetic aperture length scales accordingly, by collecting more samples as range increases [10], therefore the cross-range resolution is limited by the antenna size according to

$$\rho_a = \frac{D}{2}. \tag{2.6}$$

In contrast to stripmap mode, spotlight mode SAR collects data along a straight-line

path while the antenna is pointed at a fixed point on the ground. For this mode, cross-range resolution is not dependent on the antenna beamwidth, but upon center frequency, λ, and the aperture angle, $\Delta\theta$, subtended by the flight path according to [9, 10],

$$\rho_a = \frac{\lambda}{4\sin\left(\frac{\Delta\theta}{2}\right)}. \tag{2.7}$$

A synthetic aperture radar collects data in both the range and cross-range dimensions. This data is collected and stored in a matrix data array. When enough data is collected to form an image, the data is called a coherent processing interval (CPI) [8]. The data collected while sampling a pulse (in the range dimension) is called fast-time samples because the time scale within a pulse is very fast, on the order of the speed of light [8]. The data collected across pulses (in the cross-range dimension) is called slow-time samples because the time between successive pulses is much slower than the speed of light [8].

2.2 Linear Frequency-Modulated Waveform

A linear frequency-modulated (LFM) (or chirp) waveform is a popular choice for radar systems, including SAR systems, because it decouples time and bandwidth. This is important so that signal to noise ratio can be increased by lengthening the pulse width without reducing bandwidth. The LFM waveform can be found in several sources in the literature, a few of the SAR specific sources include [9–11]. This dissertation follows the notation given by [11] to describe the chirp waveform as

$$X_T(t,n) = A_T\, rect\left(\frac{t-t_n}{T}\right)\exp j\left\{\omega_{T,n}(t-t_n) + \frac{\gamma_{T,n}}{2}(t-t_n)^2\right\} \tag{2.8}$$

where A_T is the transmitted amplitude, t is time, T is the transmitted pulse width, n is pulse number within synthetic aperture, $\omega_{T,n}$ is the transmitted center frequency at nth pulse, t_n is the time from the start of the aperture to the start of the current pulse n, and $\gamma_{T,n}$ is the

transmitted chirp rate of the nth pulse.

Typical radar processing uses a matched filter to resolve targets [12]. The matched filter can be implemented in one of two ways: correlation or stretch processing [8]. Although both are equivalent methods to implement a matched filter, there are important differences between the two methods, particularly for interference mitigation, that will be explored in later sections.

2.3 Stretch Processing

Stretch processing is used primarily to reduce the radar receiver's analog to digital (A/D) sampling requirements of the radar signal. It is most advantageous for radars with high bandwidth (fine range resolution) and small scene sizes. As scene size increases the sampling rate advantage from stretch processing decreases. Details on stretch processing can be found within several sources [8, 10, 11]. The development and nomenclature in this document follows [11]. Essentially, stretch processing mixes the complex conjugate of the transmitted chirp (i.e. matched filter) with the received radar signal before sampling. The time offset between the received chirp (reflected from a scatterer in the scene) and the local generated copy of the transmitted chirp (usually time referenced to the scene center range) after mixing produces a single tone with a frequency that represents the scatterer's range from the scene center. This process is also called deramping, because the ramp (or linear relationship between time and frequency) is removed by the mixer. For stretch processing, as the range swath increases so does the bandwidth and corresponding sampling rate requirements. The benefit of stretch processing is that sampling rate requirements can be reduced to less than the RF bandwidth when fine-resolution is desired over a small range swath.

A visual illustration is provided in Figure 2.3 of the received LFM waveform from the near and far edge returns of the range swath at RF bandwidth as a function of time in the top plot. The middle plot of Figure 2.3 shows a representation of the phase history data

after deramp/stretch processing. Notice the near and far edge returns have changed from RF bandwidth of frequencies to single tones after deramp. Also notes that the near and far edge returns exist for the same time but are skewed relative to each other. Mathematically, stretch processing is described in [11] (and many other sources, too) where the deramp chirp has the form

$$X_L(t,n) = rect\left(\frac{t-t_n-t_{m,n}}{T_L}\right)\exp j\left\{\omega_{T,n}(t-t_n-t_{m,n})+\frac{\gamma_{T,n}}{2}(t-t_n-t_{m,n})^2\right\}, \quad (2.9)$$

where T_L is the pulse width of the deramp chirp and $t_{m,n}$ is the time delay to a reference location for the nth pulse, which is usually the time delay from the radar to the center of the scene.

The deramped signal that is sampled by the radar is called the phase history and for stretch processing it is expressed in the form [11]

$$\begin{aligned} X_V(t,n) = A_R rect\left(\frac{t-t_n-t_{s,n}}{T}\right) rect\left(\frac{t-t_n-t_{m,n}}{T_L}\right) \\ \exp j\left\{\left[\omega_{T,n}+\gamma_{T,n}(t-t_n-t_{m,n})\right](t_{m,n}-t_{s,n})\right. \\ \left.+\frac{\gamma_{T,n}}{2}(t_{m,n}-t_{s,n})^2\right\} \end{aligned} \quad (2.10)$$

where $t_{s,n}$ represents the time delay of the target response from the start of the nth pulse.

Often it is useful to express the phase history in terms of range instead of time, particularly for calculating simulated phase histories based on geometry. Using the relations following [11],

$$\begin{aligned} t_{m,n} &= \frac{2}{c}\left|\mathbf{r}_{c,n}\right|, \\ t_{s,n} &= \frac{2}{c}\left|\mathbf{r}_{s,n}\right|, \\ r_{cs,n} &= \left|\mathbf{r}_{c,n}\right| - \left|\mathbf{r}_{s,n}\right|, \end{aligned} \quad (2.11)$$

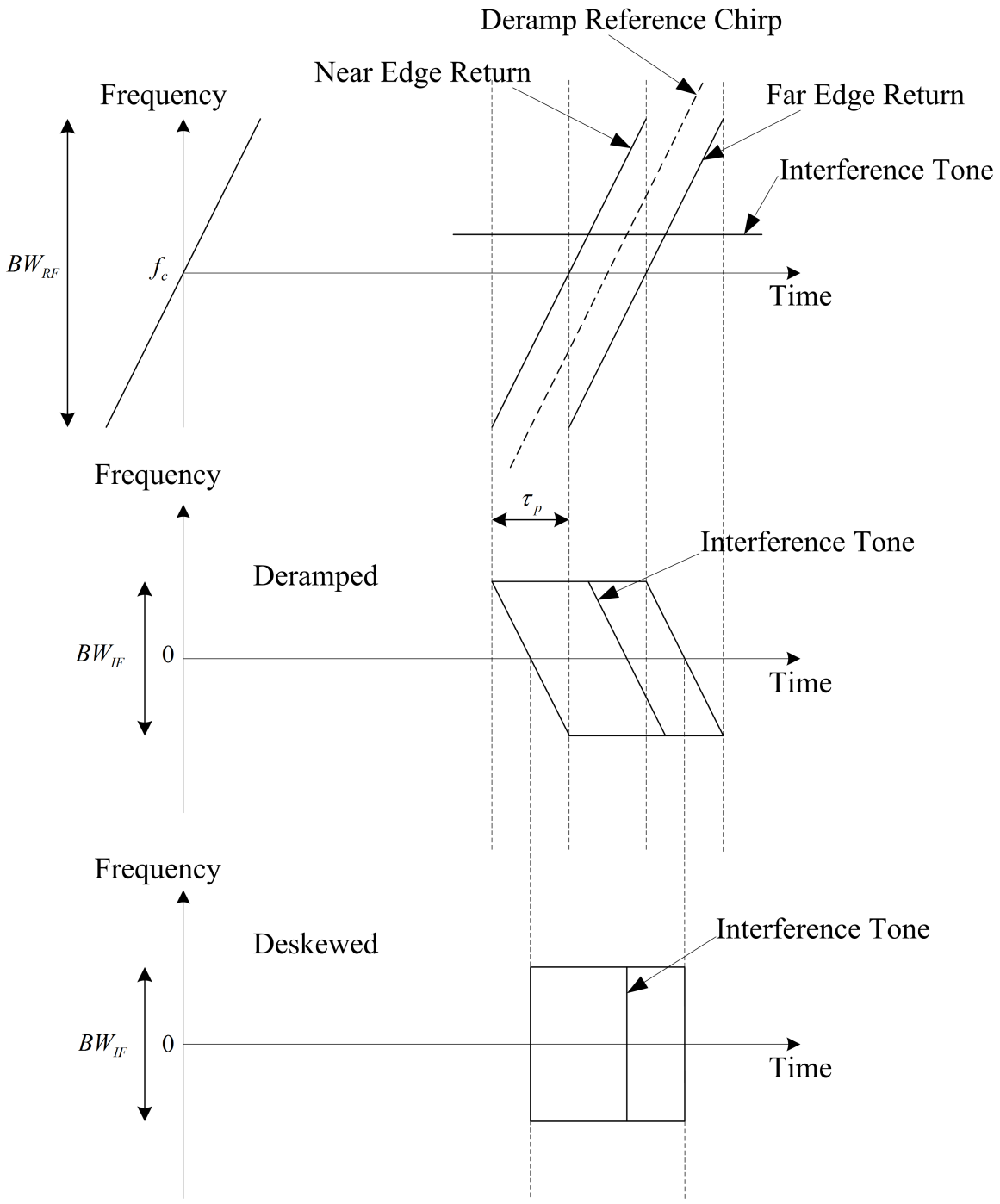

Figure 2.3: Illustrates stretch processing of a linear FM chirp waveform and the resulting data skew effect upon the phase history and a constant tone interference source (reproduced from [13]).

where $\mathbf{r}_{c,n}$ represents a vector from the scene center to the radar, $\mathbf{r}_{s,n}$ represents a vector from the scatterer to the radar, and $r_{cs,n}$ is a vector from the scene center to the scatterer. Essentially, the radar can only measure the delay to the scatterer, relative to a chosen scene center point, and the radar image indicates the scatterer's position relative to the scene center. The phase history notation can be changed from time to a digital, sampled signal by dropping the *rect* functions since the signal is time aligned by sampling and setting [11]

$$t - t_n - t_{m,n} = iT_{s,n} + \tau_n, \tag{2.12}$$

where $T_{s,n}$ is the fast-time sampling interval (i.e. the inverse of the sampling frequency) for the nth pulse and τ_n is a fast-time sampling delay of the nth pulse.

Using the above relations (2.11) and (2.12) in (2.10), the phase history expression can be rewritten as [11]

$$X_V(t,n) = A_R \exp j\left\{ \left[\omega_{T,n} + \gamma_{T,n}(iT_{s,n} + \tau_n)\right] \frac{2}{c} r_{cs,n} + \frac{2\gamma_{T,n}}{c^2} r_{cs,n}^2 \right\}, \tag{2.13}$$

where the phase term $\frac{2\gamma_{T,n}}{c^2} r_{cs,n}^2$ is called the residual video phase error (RVPE) and is an error byproduct from deramp processing. Depending on system parameters this term can be ignored, or it can be remedied by deskew processing [9–11].

The data sampled after stretch processing, X_V, particularly when stored as a CPI in a matrix, can be said to be in the spatial-frequency domain because in this form each pixel (or point target or scatterer) in the image exists as a sinusoid in this domain. The sinusoid's frequency is directly related to that pixel's differential range to the radar.

2.4 Deskew Processing

Deskew processing, also called residual video phase error (RVPE) correction, is covered in many sources, specifically [10, 11] contain detailed derivations. The RVPE is a

residual phase term from deramp processing. Each fast-time sample contains a spectrum of frequency information with a bandwidth equal to the intermediate frequency (IF) bandwidth because each echo pulse from each range cell in the patch returns a chirp at a slightly delayed time (delayed by the time equivalent of one range cell). This time delay is proportional to a frequency shift according to the chirp rate. The amount of image degradation from the RVPE depends on center frequency, aperture length, and distance [11]. The middle plot in Figure 2.3 from [13] visually describes the skew effect upon a single pulse phase history as an IF dependent horizontal shift.

Deskew processing can be summarized into the following steps. Because the RVPE is range dependent, (see the $r_{cs,n}^2$ phase term in equation (2.13)) the correction must be applied after the range is resolved by first applying a Fourier transform to the spatial-frequency domain data to resolve the data into a range dependent array.

The RVPE correction is calculated to be the complex conjugate of RVPE in equation (2.13) by using an estimate of the range. The range is only an estimate because the precise position of the scatterer is not known to the radar, but only estimated in increments according to the length of the FFT based on the IF bandwidth sampling. The correction is a direct multiplication of (2.14) to cancel the exponential RVPE term [11]. After correction, the inverse Fourier transform is applied to bring the data back to the spatial-frequency domain for resampling and image formation processing [11].

$$\exp -j\left\{\frac{2\gamma_{T,n}}{c^2}\hat{r}_{cs,n}^2\right\} \tag{2.14}$$

2.5 Impulse Response

The impulse response (IPR) of a radar system indicates the response of the system to an impulse input. Within an ideal SAR image, without aperture weighting, the impulse response is a sinc function in each dimension resulting from the bandlimited nature of the signal support (i.e. the Fourier transform of a sinusoidal pulse is a sinc centered at the

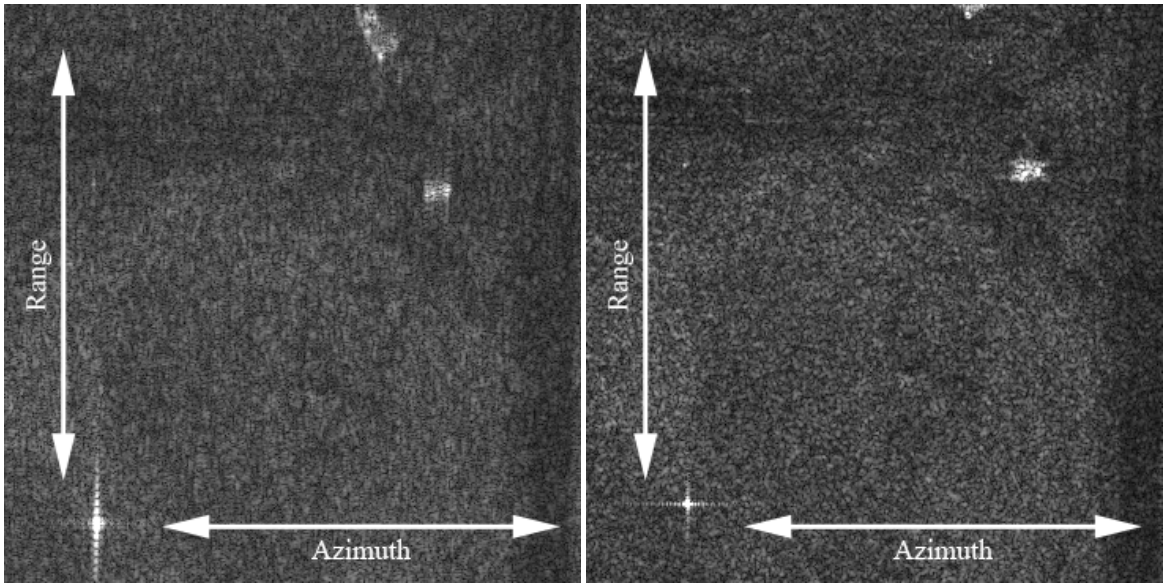

Figure 2.4: Left image shows a SAR image scene when IPR is poor. Right image shows a SAR image of terrain when IPR is good. A corner reflector is present in the bottom left of each image to measure IPR.

sinusoid frequency). The IPR in the range dimension usually represents the impulse function of the radar hardware, but can be affected by signal processing operations, such as interference mitigation. The cross-range or azimuth IPR depends upon the performance of the signal processing operations to process the image. The IPR generally indicates image quality. If the IPR has large sidelobes, it can indicate degraded image quality. For example, Figure 2.4 shows how in the left image large IPR sidelobes from terrain clutter can result in a SAR image that appears blurry when compared to the right image which has low sidelobes. In this example, both images have the same aperture weighting to control sidelobes, but the left image has distortion from interference mitigation. A corner reflector can be found in the bottom left corner of each image as a bright white cross in Figure 2.4. The cross appears because the sidelobes of the point target are a larger value than the background clutter. Notice that the left image's corner reflector has a line of dots in the vertical direction; this is the large sidelobe structure that causes blurring. The entire image appears blurry because every point in the left image has a line of dots in the vertical direction.

Figure 2.5a shows the ideal IPR response is a sinc function along either the range or

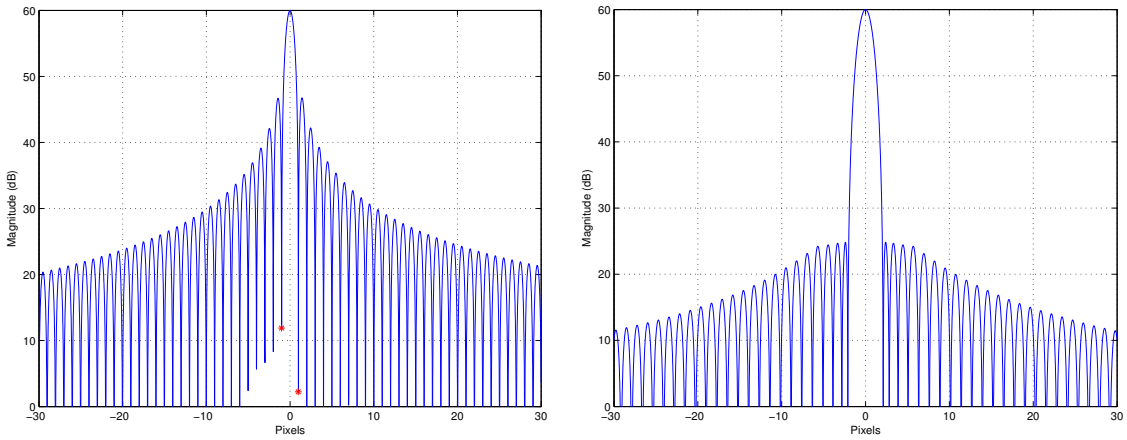

(a) No Weighting **(b)** Taylor Weighting

Figure 2.5: An example of an ideal IPR (a) without aperture weighting and (b) with Taylor window -35dB SLL and $\bar{n} = 4$.

azimuth dimension of a SAR image formed from rectangular frequency support. Many radar systems utilize a window function to suppress the -13dB sidelobes of the sinc function and the Taylor window is a popular choice [10]. The Taylor window is desirable because it allows tuning of the sidelobe level and number of constant level sidelobes while minimizing the IPR broadening compared to other windows [14]. Furthermore, the Taylor window with peak sidelobe level -35dB and $\bar{n} = 4$ is a nearly ideal window that maximizes mainlobe energy relative to sidelobe energy level [15]. Figure 2.5b shows an ideal IPR with a Taylor window applied to the data results in a much lower sidelobe level.

To compare one IPR to another IPR, metrics can be calculated to quantify the IPR shape including width, integrated sidelobe ratio (ISLR), and peak sidelobe level (PSLL). Because a SAR image is 2 dimensional, an IPR is made for each dimension: range and azimuth. The mainlobe width is simply a measurement of the width in pixels at particular values from the peak, typically 3dB and 18dB. The mainlobe width can be a measure of effective resolution within the image by encapsulating image processing choices such as oversampling and window function effects. Typically, the image is oversampled with respect to the resolution to produce a more aesthetically pleasing image. An image oversampling factor of 1.25 is

reasonable for most cases. The window function further broadens the oversampling factor so the measurable 3dB mainlobe width in pixels is a product of both factors. The ISLR is the ratio between the energy in the sidelobes to the energy in the mainlobe. Sidelobe structure can vary significantly between IPRs and across distance, therefore the ISLR is an accepted metric that provides a quantifiable comparison of sidelobes. The peak sidelobe level (PSLL) is exactly as it sounds, the peak sidelobe level from the mainlobe. For a sinc response, the PSLL is approximately -13dB.

For a Taylor window $\bar{n} = 4$ and SLL -35dB, the mainlobe is broadened by a factor of 1.1842 (after image oversampling by 1.25 the measureable 3dB width is 1.5 pixels), the ISLR is -36dB, and the PSL is -35dB. Figure 2.6 shows all of these metrics applied to an IPR from a SAR image where the range IPR is plotted on top and the azimuth IPR is plotted on the bottom of the figure. Occasionally, it is noticeable that the mainlobe doesn't appear centered in the IPR plot; the simple explanation for this is the upsampled IPR has a different peak location than the brightest image pixel. This effect occurs when the true IPR peak is located in between two image pixel center points.

2.6 Noise Equivalent Reflectivity

To encapsulate the performance of a SAR it is often practical to define the radar cross-section (RCS) value of noise for the image, called noise equivalent reflectivity or σ_N [16]. Using this factor it is straightforward to determine if an object is visible within a SAR image and its signal-to-noise ratio (SNR) by calculating its RCS and comparing it to σ_N. If its calculated RCS is greater than σ_N, it will be visible in the image, and the difference between the two values is the SNR. The importance of SNR as it relates to coherence will be made clear in later sections, here it it suffices to say that they are proportional to each other.

The noise equivalent reflectivity (σ_N) is not a constant value for a radar system [16]. As a radar specification, σ_N is defined as a maximum value over the specified region of

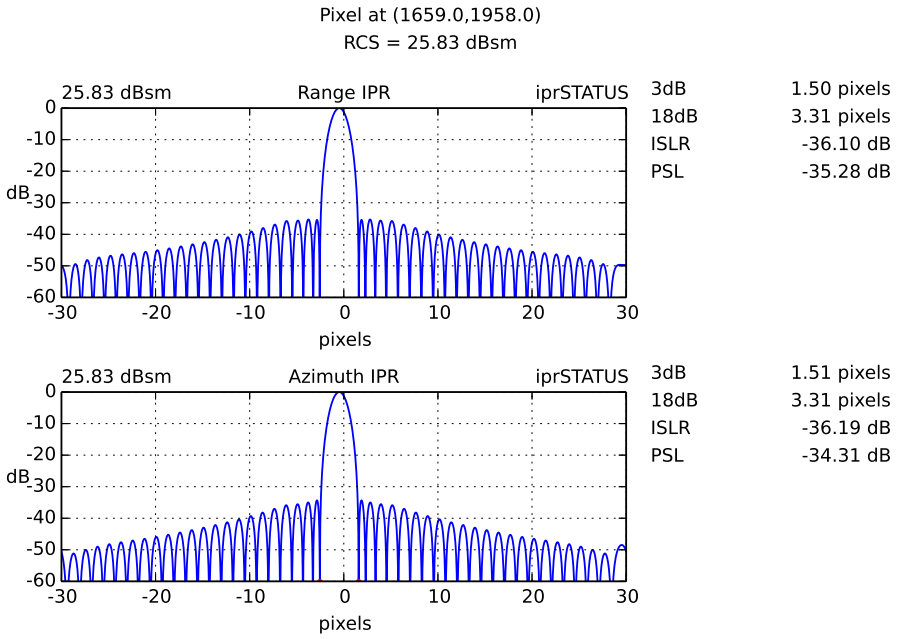

Figure 2.6: An example of an ideal IPR and calculated metrics with Taylor window -35dB SLL and $\bar{n} = 4$. The top plot is the range IPR, the bottom plot is the cross-range (or azimuth) IPR, and the metrics for each dimension are located to the right of each plot.

operation. Noise equivalent reflectivity varies with radar operating geometry, hardware, and image processing choices, the details of these relations are found in [16]. Since most of these parameters are fixed once a radar is in operation, the most important factor to determine σ_N is the effective duty factor. Stretch processing helps to increase the SNR by enabling longer pulse widths where geometry allows while maintaining RF bandwidth. At short ranges, transmitting more pulses than necessary within a sampling interval (called presumming) can also increase duty factor. These SNR trade-offs (and associated coherence impact) are important to consider when evaluating interference mitigation techniques, particularly the methods that don't transmit pulses to sample the interference signal.

2.7 Coherence

Coherence can have multiple connotations. In this document coherence can be considered a measure of the similarity (or difference) between two images. For example, coherence can be a useful metric to evaluate differences in image processing algorithms if one

is attempting to make a faster image formation implementation while retaining the same image quality. The ideal image can be cohered with the image made with the faster algorithm to assess the effects of the processing optimization. The coherence metric not only measures the magnitude between two images, but also includes the phase component in the comparison. The coherence measure is the complex cross-correlation of the two images, but is often computed using the maximum likelihood estimator (MLE) [4, 9, 17]

$$\hat{\mu}_n = \frac{\sum_{n=1}^{L-1} x_{1,n} x_{2,n}^*}{\sqrt{\sum_{n=1}^{L-1} |x_{1,n}|^2 \sum_{n=1}^{L-1} |x_{2,n}|^2}}, \tag{2.15}$$

where L is number of 'looks' or local pixels about n, $x_{1,n}$ is the nth pixel of image 1, and $x_{2,n}$ is the nth pixel of image 2.

There are many sources of loss, including SNR, phase errors, etc. [4, 17, 18]. The losses are multiplicative such that any one term can dominate the system coherence. Maintaining a high level of coherence is important for many radar systems because it can indicate the quality of data products produced by the radar system.

Coherent data sets can be created in a few different ways, depending upon the application. For height map creation, interferometric SAR (IFSAR) processing is necessary, but can be applied to different radar architectures. To eliminate temporal decorrelation effects it is desirable to use a multiple channel radar system where each channel is separated in height. Single channel systems can also create height maps if the flight geometry is adjusted between collections, usually a particular height separation. For coherent change detection products, it is the temporal decorrelation that is of interest, so only a single channel system that repeatedly flies the same collection geometry is all that is required.

The phase component of the coherence estimator when each image is collected under the right conditions, can be processed to measure the height of terrain and other objects to create a digital elevation model (DEM). This type of processing is called IFSAR. Today LIDAR systems are a popular choice for producing height maps, however these systems are

Figure 2.7: Example of a DEM created from IFSAR processing with Sandia National Laboratories' Rapid Terrain Visualization (RTV) system [20].

limited to clear weather unlike microwave systems. One of the most well-known IFSAR sensors is DLR's TanDEM-X [19], a spaceborne, X band radar that creates global DEMs. The reader is referred to [4, 9] for more information about IFSAR. An example of a DEM from Sandia National Laboratories' Rapid Terrain Visualization (RTV) system is shown in Figure 2.7.

Another application of the coherence estimator is interferometric change detection [9], also called coherent change detection (CCD), where the magnitude of the coherence estimator is calculated between two images collected from different passes (times) under the same parameters and geometry. Observe in Figure 2.8 that there are no perceptible changes between the top image Figure 2.8a and the middle image Figure 2.8b, however the changes are clearly visible in the CCD product in Figure 2.8c by mapping the magnitude of the coherence estimator, $|\hat{\mu}|$, to grayscale values. White indicates no change between images, $(|\hat{\mu}| = 1)$, while black indicates change has occurred, $(|\hat{\mu}| = 0)$. Figure 2.8c shows tire tracks from where a vehicle has traveled in the time between two images were collected.

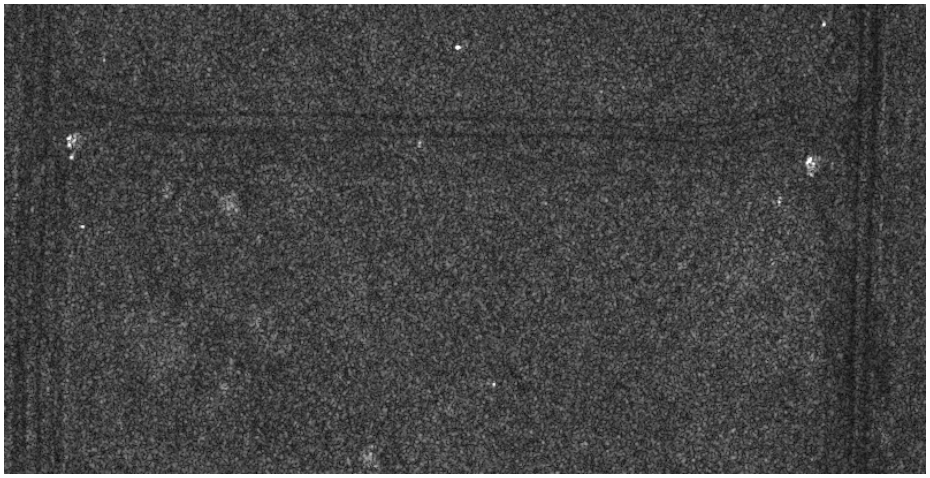

(a) Image from collect 1.

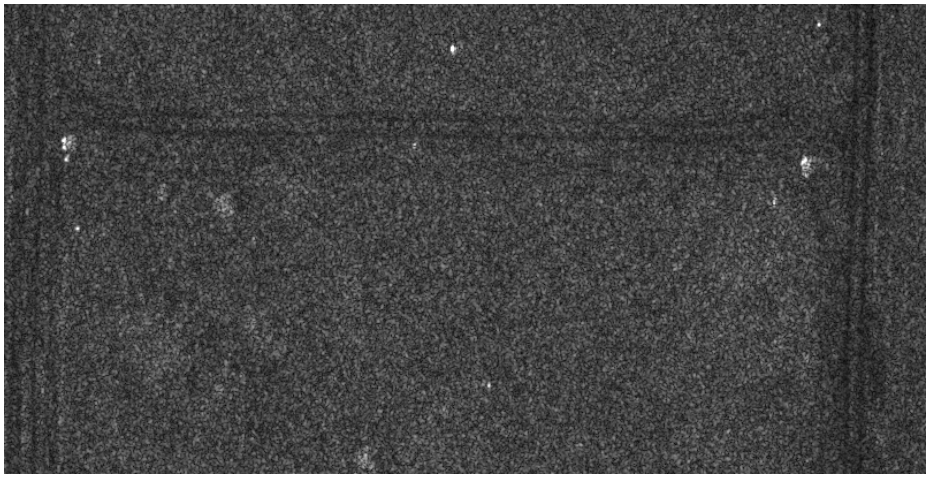

(b) Image from collect 2.

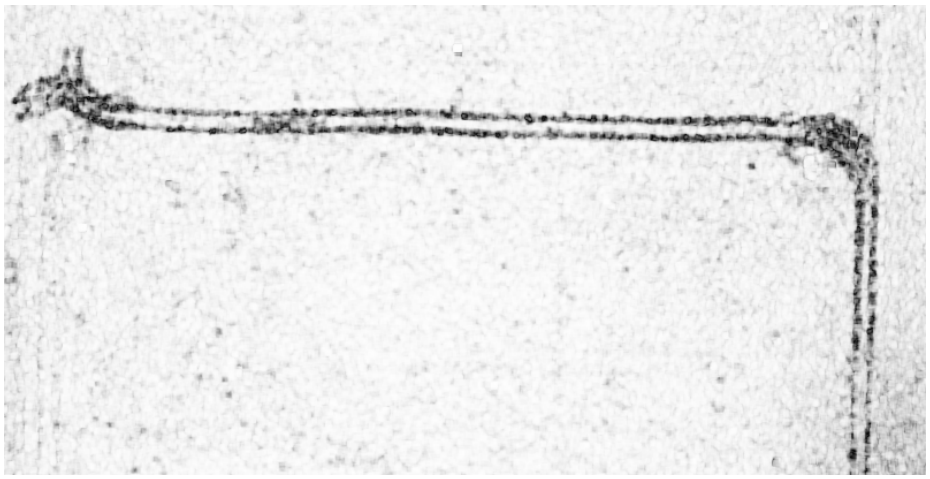

(c) Coherent change detection (CCD) image.

Figure 2.8: Example of a coherent change detection (CCD) product. The changes in (c) shown in black are not evident in the magnitude images.

2.8 Radio Frequency Interference

While there are many sources of radio frequency interference (RFI), many of them can be modeled as a single or collection of constant tones in the form

$$A_{tone} \exp j \left\{ \omega_{tone} \left(t - t_n - t_{m,n} \right) \right\}, \tag{2.16}$$

where A_{tone} is the amplitude and ω_{tone} is the frequency.

However, this form may not accurately describe the signal found within the radar data. For radars that use stretch processing, the interference tone is mixed with the complex conjugate of the transmitted chirp waveform in equation to produce the following signal within the phase history

$$\begin{aligned} X_{DRT} &= X_{tone} X_L^* \\ &= \exp j \left\{ \left(\omega_{tone} - \omega_{T,n} \right) \left(t - t_n - t_{m,n} \right) - \frac{\gamma_{T,n}}{2} \left(t - t_n - t_{m,n} \right)^2 \right\} \end{aligned} \tag{2.17}$$

where DRT subscript stands for deramped tone.

Additionally, due to stretch processing the interference tone is not present during all of the fast-time samples in the phase history, it is limited by the time equivalent of range swath (IF bandwidth) [6, 13]. This can visually be seen in the middle plot in Figure 2.3 by projecting the interference tone onto the time axis. From stretch processing, each fast-time sample contains a band of frequencies, the IF bandwidth. The center frequency of the band of frequencies moves with every fast-time sample along the RF bandwidth of the pulse. If the interference only occupies a single or small number of frequencies, then it will only appear in the fast-time data samples where that fast-time sample's band of frequencies includes the interference frequency. The center point of the interference energy within the fast-time samples is determined by interference and radar center frequency regardless of

the interference source timing relative to the radar pulse, according to [13]

$$\frac{\omega_{tone} - \omega_{T,n}}{\gamma_{T,n}}. \tag{2.18}$$

The interference expression X_{DRT} is non-zero in time from [6, 13]

$$\frac{\omega_{tone} - \omega_{T,n}}{\gamma_{T,n}} - \frac{\tau_p}{2} < t - t_n - t_{m,n} < \frac{\omega_{tone} - \omega_{T,n}}{\gamma_{T,n}} + \frac{\tau_p}{2} \tag{2.19}$$

Where the time it takes light to travel twice the distance of the range swath is τ_p.

Figure 2.9 verifies the interference tone within the fast-time phase history magnitude data occupies only a limited number of samples. Expanding the single pulse case to a 2D SAR image, Figure 2.10 shows only the image artifacts from a single tone interference source and six point targets.

Figure 2.11a shows that low amplitude single tone interference has little effect upon the impulse response (IPR). It does increase the ISLR, however the mainlobe and its width remains unchanged. Figure 2.11b shows the high amplitude single tone interference follows the trends of the low amplitude case by elevating the ISLR while leaving the mainlobe width unchanged. The primary concern for single tone interference is the increase in energy throughout the image. At low interference amplitude levels only the shadow regions will appear to be affected. However as interference energy increases the image degradation and associated image artifact levels increasingly obscure the terrain response.

It should be noted that the RCS measurements in Figure 2.11 are not calibrated to any specific reflector as typical RCS measurements. Because this is simulation, no actual hardware system values are used and all values are relative to each other except one. The RCS value is set by defining a maximum RCS to be represented within the SAR image and the number of bits to represent each pixel value. This dissertation defines 30dB to be the maximum RCS value and uses 16 bits for magnitude and 16 bits for phase. From this maximum point, all other RCS and magnitude measures are scaled.

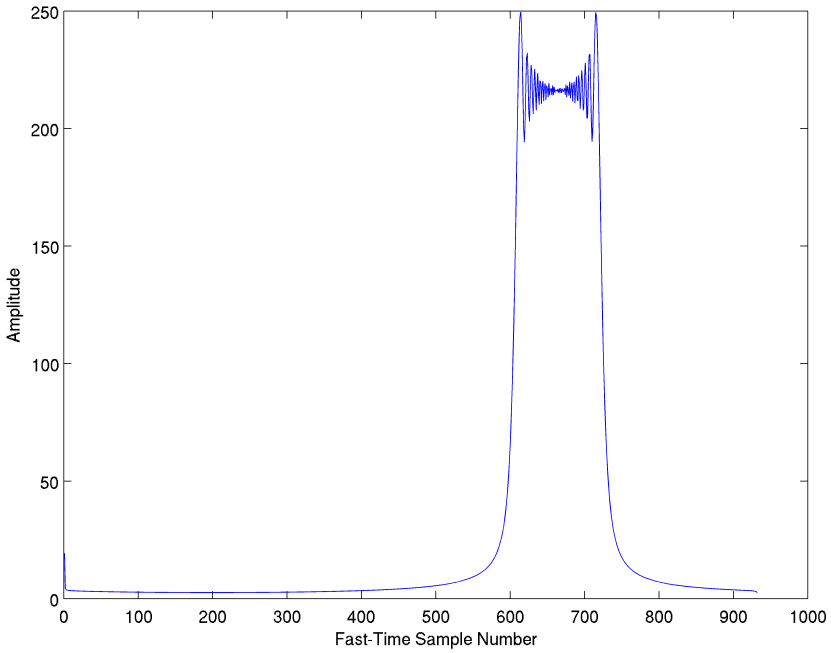

Figure 2.9: Single pulse phase history containing only a single tone interference source.

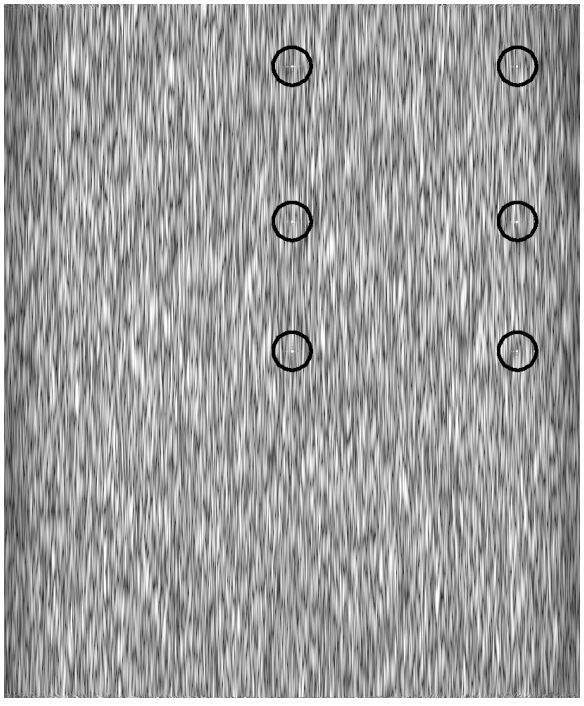

Figure 2.10: Image artifacts from a single tone interference source, image artifacts at RCS -10dB. Point targets are indicated by black circles.

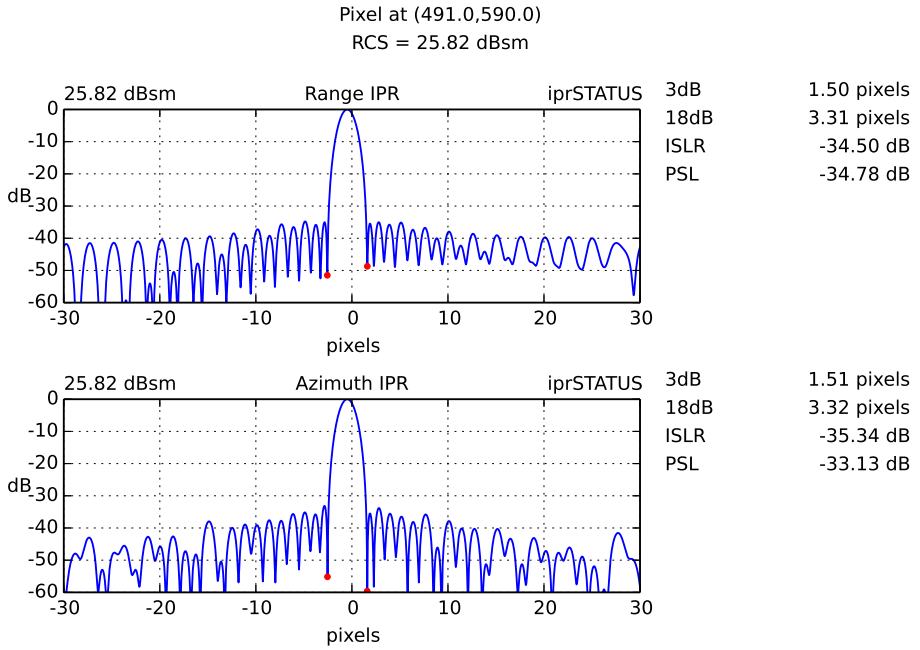

(a) Interference image artifacts RCS -25dB

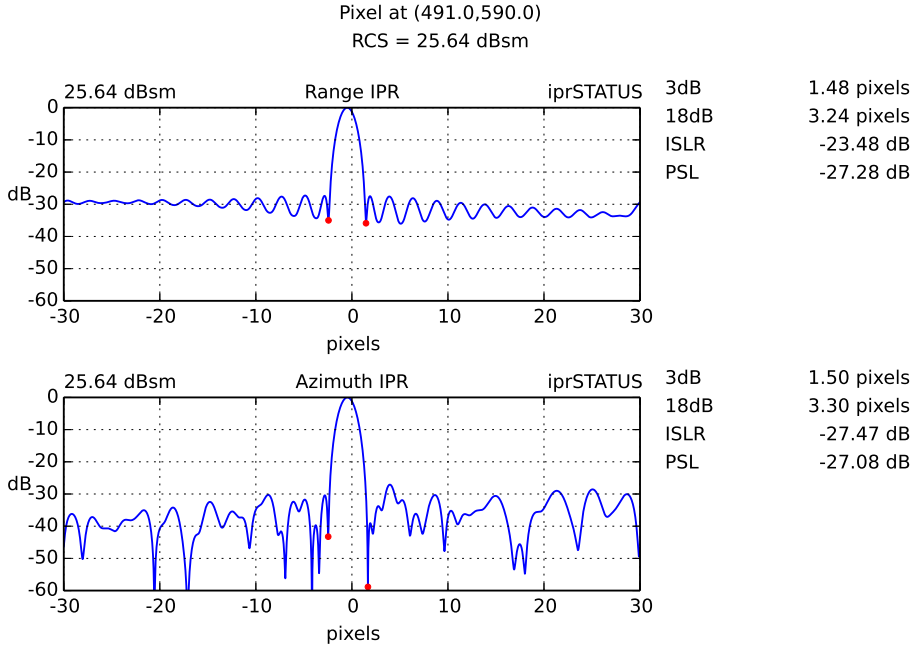

(b) Interference image artifacts RCS -10dB

Figure 2.11: IPR for point target with single tone interference source for (a) image artifacts at RCS -25dB and (b) image artifacts at RCS -10dB.

2.9 Summary

This background section has only touched on many subjects relevant to understanding SAR and the specifics of stretch processing used in this dissertation for fine-resolution, repeat pass collections. Hopefully this section serves as a refresher or to clarify the terms and concepts utilized throughout this document. The next chapter utilizes these concepts to demonstrate interference effects upon SAR imagery and the application of different mitigation strategies for stretch processing.

CHAPTER 3

INTERFERENCE EFFECTS AND MITIGATION APPROACHES

This dissertation seeks interference mitigation methods that improve the quality of coherent data products over existing techniques. Earlier it was explained there are many ways to make coherent data products (including IFSAR and CCD), but the method considered for this dissertation is repeat collections of the same area using the same flight geometry for each pass. Because there is a time separation between passes this also means that the interference source can change its characteristics between successive passes (e.g. change frequency or turn on/off). In this chapter it is assumed that the first pass is free of interference and the second pass contains interference; this assumption allows coherence to quantify image quality effects due to the interference and the mitigation.

This chapter begins by explaining how interference degrades the image and coherent data products. Then, an overview of many interference mitigation techniques are presented. Next, it is shown how typical LMS filtering and linear predictor algorithms do not apply to radars using stretch processing. Then the standard notch algorithm is presented as it is applied to radars using stretch processing and the coherence impacts of using this mitigation are revealed.

3.1 Image and Coherent Data Product Degradation from Interference

Earlier, it was shown that interference produces artifacts in SAR imagery. It is these artifacts themselves that decrease the estimated coherence value, $\hat{\mu}$. The mechanism for coherence reduction is a decrease in SNR. The interference energy is not the signal energy, therefore it adds to the noise energy. The interference energy can be combined with the

noise energy to define a signal-to-interference-plus-noise ratio (SINR) calculated as [4, 17]

$$\mu_{\text{SINR}} = \frac{\text{SINR}}{\text{SINR}+1}. \tag{3.1}$$

The interference signal energy is considered additive noise and can be observed in Figures 2.11a and 2.11b as contributing additional energy into the sidelobes of the IPR, but not distorting the IPR itself. The additional energy from interference can create both false correlations and false decorrelations; either case results in a poor coherent image product.

As an example of the effect of interference image artifacts upon a CCD, Figure 3.1 shows a simulation of a CCD product with a horizontal, linear decorrelation pattern and the resulting effects of increasing the interference power as ratio of the power of the phase history from the reflected radar signals to the power of the interference signal in the phase history domain, or signal-to-interference ratio (SIR). This simulation uses a single tone interference source consistent with the model described in section 2.8. As interference amplitude increases, Figure 3.1f shows that there is a point at which the original disturbance is no longer visible. This exact point varies according to many factors including the radar system, signal processing, and the interference signal characteristics.

Once the image artifacts from the interference exceeds an image and/or coherence degradation threshold that is unique for a particular radar and mission, a mitigation technique is required to remove the interference energy. The type of interference mitigation technique must be chosen carefully so that the mitigation is not worse than the interference itself. The remainder of this chapter discusses various techniques in the literature as they apply to multiple pass deramp SAR systems.

3.2 Interference Signal and Stretch Processing

For radars that use deramp or stretch processing, the deramp chirp signal spreads the spectrum of the interference while the IF filter limits the bandwidth. The resulting phase

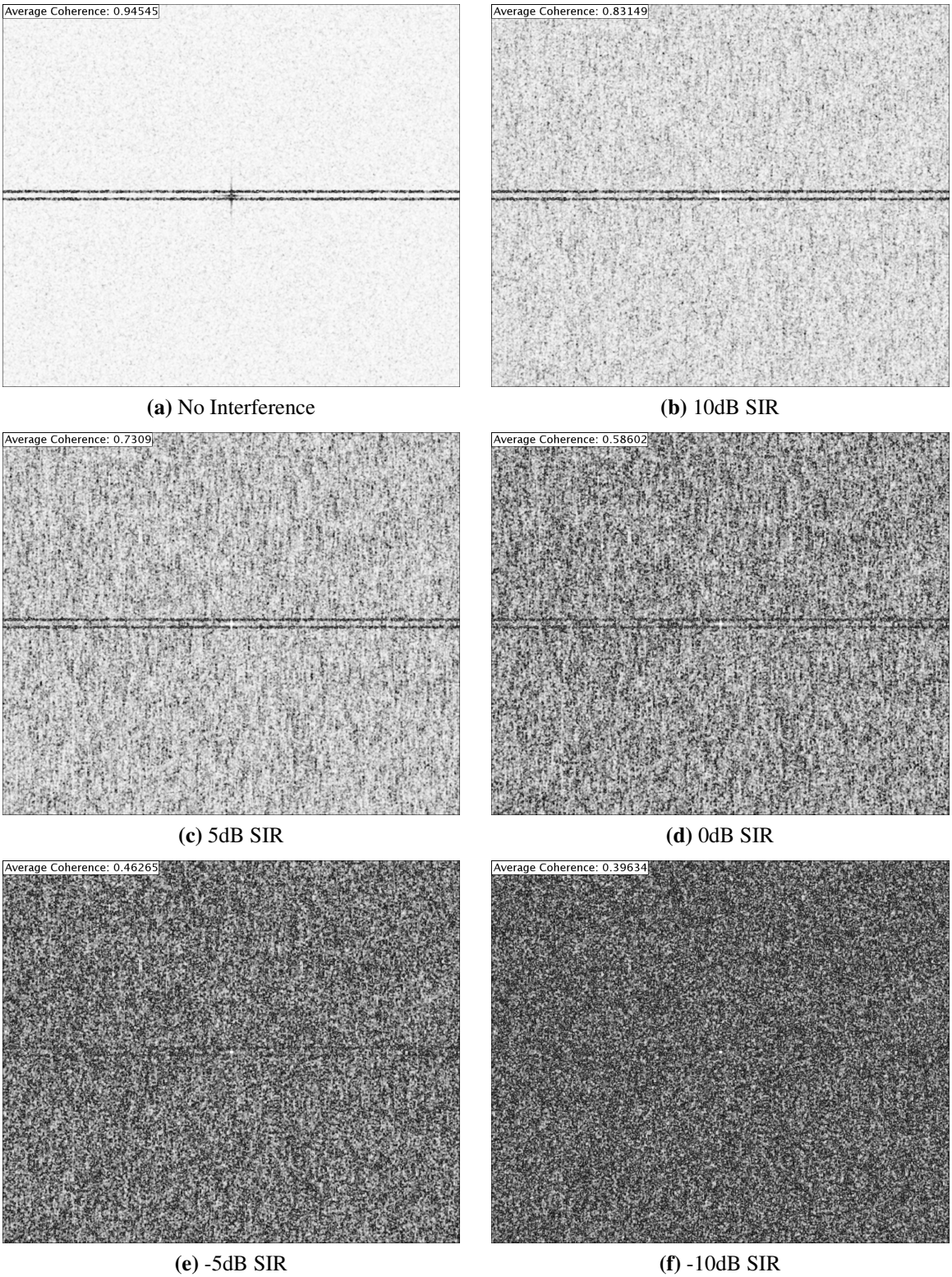

(a) No Interference **(b)** 10dB SIR

(c) 5dB SIR **(d)** 0dB SIR

(e) -5dB SIR **(f)** -10dB SIR

Figure 3.1: Simulation of the average coherence effects from a single tone interference source as interference signal power increases.

history for a single tone interferer is a signal limited in time duration to the patch range length as expressed earlier in section 2.8, equation (2.19). For many detection and mitigation techniques it is desirable to minimize the number of samples containing interference. It turns out that the deskew correction that removes the residual video phase error term from deramping also reduces the number of samples occupied by the interference by removing the residual chirp term of the deramped interference signal [6, 13]. The following development explains exactly how this cancellation occurs.

Recall from section 2.8 a constant tone interference source is limited in time. The time period for which X_{DRT} is non-zero will be represented as t_p. The expression for X_{DRT} in equation (2.17) becomes

$$X_{DRT} = \exp j\left\{(\omega_{tone} - \omega_{T,n})\, t_p - \frac{\gamma_{T,n}}{2} t_p^2\right\}. \tag{3.2}$$

For deskew processing the data is transformed from the spatial-frequency (time domain) to a range profile (frequency domain) by the Fourier transform before applying the phase correction [10, 11]. If it is assumed for the purpose of calculating the Fourier transform of

X_{DRT} that t_p is not limited, the Fourier transform of X_{DRT} is calculated as follows:

$$\mathscr{F}[X_{DRT}] = \int_{-\infty}^{\infty} \exp\left\{ j\left[(\omega_{tone} - \omega_{T,n})\, t_p - \frac{\gamma_{T,n}}{2} t_p^2 \right] \right\} e^{-j\omega t_p} dt_p.$$

Using substitution: $\omega_\Delta = \omega_{tone} - \omega_{T,n}$,

$$\begin{aligned}
\mathscr{F}[X_{DRT}] &= \int_{-\infty}^{\infty} \exp\left\{ -j\frac{\gamma_{T,n}}{2}\left(t_p^2 + \frac{2}{\gamma_{T,n}}(\omega - \omega_\Delta)\, t_p \right) \right\} dt_p, \\
&= e^{j\frac{1}{2\gamma}(\omega-\omega_\Delta)^2} \int_{-\infty}^{\infty} \exp\left\{ -j\frac{\gamma_{T,n}}{2}\left(t_p + \frac{1}{\gamma_{T,n}}(\omega - \omega_\Delta) \right)^2 \right\} dt_p.
\end{aligned}$$

Where: $x = \sqrt{\frac{j\gamma_{T,n}}{2\pi}}\left(t_p + \frac{1}{\gamma}(\omega - \omega_\Delta) \right)$,

$dt_p = \sqrt{\frac{2\pi}{j\gamma_{T,n}}}\, dx$, and

$\int_{-\infty}^{\infty} e^{-\pi x^2} dx = 1.$

$$\begin{aligned}
\mathscr{F}[X_{DRT}] &= \sqrt{\frac{2\pi}{j\gamma_{T,n}}} \exp j\left\{ \frac{1}{2\gamma_{T,n}} (\omega - \omega_\Delta)^2 \right\}, \\
&= \sqrt{\frac{2\pi}{j\gamma_{T,n}}} \exp j\left\{ \frac{1}{2\gamma_{T,n}} \left(\omega^2 - 2\omega\omega_\Delta + \omega_\Delta^2 \right) \right\}.
\end{aligned} \tag{3.3}$$

Since ω is limited in frequency to the IF bandwidth, and from stretch processing the image range extent is determined entirely by the IF bandwidth, ω can be expressed in terms of the range according to the relation $\omega = \left(\frac{2\gamma_{T,n}}{c}\right)\hat{r}_{cs,n}$, where $\hat{r}_{cs,n}$ approximates the range position over the image range extent. Substituting this relation into the first phase term of equation (3.3) produces the following form

$$\begin{aligned}
&\exp j\left\{ \frac{1}{2\gamma_{T,n}} \left(\frac{2\gamma_{T,n}}{c} \right)^2 \hat{r}_{cs,n}^2 \right\}, \\
&\exp j\left\{ \frac{2\gamma_{T,n}}{c^2} \hat{r}_{cs,n}^2 \right\}.
\end{aligned} \tag{3.4}$$

It should be clear that the phase correction applied for deskew processing in equation (2.14) will cancel the above phase term responsible for spreading the spectrum of the single tone interferer.

There are two benefits for applying the deskew processing to reduce the number of samples containing interference energy: one is mitigation techniques will modify less samples, and the second is that the samples containing interference have higher power and may be easier to detect.

3.3 Detection

There are many ways to detect interference but the theory is simple: find a domain where the interference signal is unique from the radar signal. Many detectors evaluate if a data sample has an unusually high power level in the frequency domain [21], or in the time sampled data [13]. For this dissertation the details of the detector or the particular interference characteristics matter little for evaluating the impact of different mitigation techniques. All practical detectors will be better or worse at detecting a particular signal at a particular power level, so there is a possibility for interference signal energy to pass through the detector. This can become problematic when measuring the average coherence values because it has been shown in Figure 3.1 that the interference signal itself is a source of decorrelation. In the case of residual interference energy changing based upon detector type, it is difficult to compare the relative effectiveness of different mitigation methods since each method has different interference energy to mitigate.

Whether by an interference detector or spectrum coordination requirements, in the end all that matters from a detector is that a region of spectrum has been identified to contain interference. For this dissertation an ideal detector is assumed that is able to completely detect all interference energy so that coherence effects from only the mitigation technique are evaluated.

3.4 Spectrum Sniffing

One simple and effective interference mitigation method used by several radars is to directly record the interference signal itself, without the radar return signal [5, 22]. For the

CARABAS radar, data is collected in bursts of pulses and within a burst the radar turns off the transmitter for one pulse to record only the interference signals [5]. Later during processing, a frequency filter is constructed with the interference signals previously recorded to remove interference in the other pulses within that burst [5]. Ferrell [22] describes a radar system that alternates between collecting data and collecting only interference signals to overcome time-varying characteristics of the interference signals.

A limitation for these techniques is that if the interference changes faster than the rate at which it is recorded, then it will not be removed. Another limitation is that recording only the interference signal requires not transmitting a radar pulse; this lowers the SNR of the system and may lower the achievable coherence of the radar system.

3.5 Coherent Estimation and Removal

Coherent estimation of the interference signal for direct subtraction from the radar echo data is a technique used by many in the literature. It is a desirable approach because if the estimated signal is accurate, there is minimal disturbance to the phase history signal. Many of these techniques use a simple model for the interference as a single or summation of tones for which the amplitude, frequency, and phase of each interference signal must be estimated. The signals from scatterers in the scene occupy the entire RF bandwidth of the radar and approximate bandlimited noise in contrast to the sinusoidal interference signals. As this is a challenging problem, and each radar is different, there are many approaches available. Typically most approaches estimate the frequency of the interference sources then solve for the amplitude and phase.

In an early paper by Braunstein [23], the performance between a maximum likelihood estimator, least-squares, and autoregressive models are compared. Miller [24] uses knowledge of the interference sources and develops a specifically tuned least-square estimator to calculate the interference signal. A phased-locked loop [25] and a gradual RELAX algortihm [26] has been used to estimate the interference signal [25].

The LMS adaptive algorithm can also be used to estimate the interference signal parameters based on the data. Potsis [27] directly uses the LMS algorithm to improve interference mitigation, while Golden [6] describes an iterative processing algorithm similar to LMS where the radar collects data of the interference signals only to estimate the frequency of the interference sources. Then with the frequencies known an iterative estimation algorithm, called Parametric Maximum Likelihood, calculates the amplitude and phase of each frequency within the data to be filtered [6].

An autoregressive approach utilizing a linear predictor is shown to yield good results [28].

The difficultly applying these techniques to deramp SAR is that the phase history information contains sinusoids that represent the scatterers in the scene while the interference is a chirped signal. Or the interference is only present for so few samples that it is difficult to estimate the amplitude and phase if the frequency of the interference was known or detectable.

3.6 Sidelobe Apodization

There are a several techniques to reduce the appearance of sidelobes in the SAR imagery by applying a weighting function (i.e. apodization) [29–32]. Doerry [33] took a unique approach to reduce sidelobe energy from interference mitigation by minimizing each pixel value between the original image with interference and the image where interference has been mitigated. In this way, the higher sidelobes from the mitigation's distortions are replaced with lower values from undistorted sidelobes and the fine mainlobe response is preserved in the mitigated image. This works because interference is additive to the image and does not corrupt the IPR as previously shown in Figure 2.11a.

Although, if the average RCS of the interference artifacts are of a high enough value, on the order shown in Figure 2.11b or Figure 3.1f, then the mitigated image may not receive any benefit from the original image.

3.7 Compressive Sensing

In recent years compressive sensing has been an active research area for the radar community. It is an attractive idea because it may allow less samples to be collected by the sensor to achieve the same, or similar, image quality. The application benefit is clear when considering the case where a digital camera collects RGB data values for every pixel of an image and then much of that information is lost through JPEG compression. A compressive sensing approach may yield the same quality JPEG image with fewer captured pixels or enable a higher quality image as if more pixels were captured by the sensor. Many radar applications apply compressive sensing techniques to augment missing data samples or repair undesirable image artifacts. Actually, repairing data distortions and correcting a poor IPR is not an entirely new concept, especially for radar. There are many spectral estimation algorithms applied to SAR imaging to reduce sidelobes and enhance resolution [29]. CLEAN [34] has been proven to repair point targets in SAR images [13], but it is not designed for SAR terrain (as will be demonstrated later).

Compressive sensing takes the approach that a signal has a sparse representation in some domain, then creates a mapping from the sparse domain to the final product that matches a constraint.

The difficulty for fine-resolution, deramp SAR is selecting an appropriate domain for sparsity. Many applications select a few of the brightest radar returns and zero the rest of the image values to create sparsity in the image domain. However, for change detection and height mapping applications, the clutter (i.e. terrain) values contain important information and cannot be simply zeroed out. Likewise, every sample of the phase history contributes to every pixel in the image, so zeroing data in the spatial-frequency domain will lose power and resolution. Also, many applications of compressive sensing require a random loss of data samples, whereas for a notching type of interference mitigation the samples corrupted with interference do not have to be randomly distributed throughout the phase history because the interference's frequency characteristics determine its location in

the phase history.

Most of the papers that have been published on compressive sensing for SAR have a priori knowledge of the number of point targets in the image, or there is no clutter/terrain required in the final image. Nguyen [35] has published a paper that uses a compressive sensing technique to repair the phase history from notching interference, but it is not an application of a fine-resolution, deramp SAR capable of change detection products.

This dissertation examines the mechanisms that influence coherence performance. It is with this understanding that these compressive sensing techniques need to be applied if they are to prove useful over other mitigation methods.

3.8 Least Mean Square Adaptive Filter

A very popular method to remove interference is to apply a least-mean-square (LMS) filter to remove the interference [7, 36–40]. This usually works well for the case when the interference signal is present throughout the entire recorded phase history data samples, such as direct sample radars. The drawback of the LMS filter is that it requires a start-up time, it is sensitive to the filter parameters, and it does remove a portion of the radar signal while filtering the interference.

The LMS filter uses a weighting of a number of previous samples (i.e. a filter) to predict the next sample value [41]. The filter becomes adaptive when the weighting changes each sample interval based upon the data output. Implementation of LMS requires setting three parameters: filter order (M), delay (Δ), and step-size (η) [41]. Then solving the equations

$$
\begin{aligned}
e(n) &= x(n) - y(n), \\
y(n) &= w^H(n)x(n-\Delta), \\
w(n+1) &= w(n) + \eta x(n)e^*(n).
\end{aligned}
$$

A block diagram of an adaptive LMS filter is shown below in Figure 3.2. Examples of

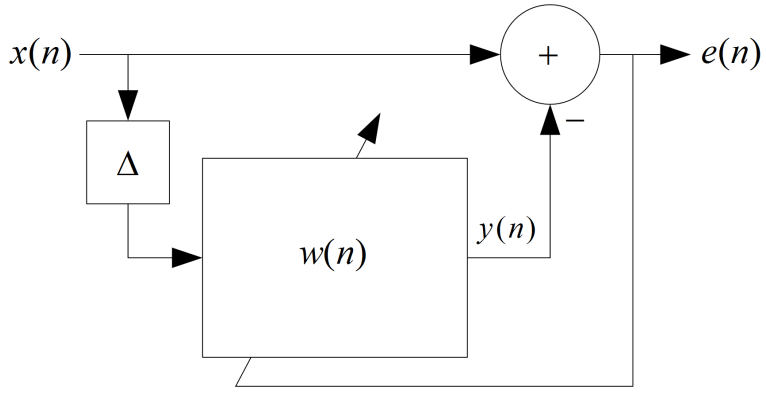

Figure 3.2: Block diagram of LMS filter.

applications of LMS filters applied to SAR data to remove interference can be found in [36–38].

Unfortunately, the LMS filter is unsuitable for radars with deramp processing for two reasons. The first is the sudden change found in deramp SAR data between the radar echo signal and the interference signal (see top plot of Figure 3.3 for one example). The step-size parameter η can help the filter adapt quickly to changing power levels, but there are limits to the step-size parameter values [41]. If η is too big, then the filter can overestimate values and grow unstable [41], however if η is too small then the signal cannot adapt quickly enough to the sudden amplitude increase from the interference, and the interference is not suppressed.

The second reason the LMS filter is unsuitable for deramp radars is that the LMS adaptive filter estimates the interference signal as a sinusoid [36, 38]. The deramped phase history itself is a sum of sinusoids, so the filter must uniquely identify the interference sinusoid from the sinusoids of all the other reflectors in the scene. But it has already been shown that the interference is actually a chirp signal unless deskew processing has removed the chirp while dramatically reducing the signal length. This is contrary to the assumption LMS filters make that the radar echo data is noise-like [36, 38].

A 1D simulation was made for a single point target at 15dB, clutter level of -13dB, and SIR of 0dB using the parameters in Table 3.1 below to approximate a typical point

target in typical terrain. Figure 3.3 shows the results of using MATLAB's normalized LMS filter from the DSP System toolbox with optimal LMS parameters from [36] where the filter order is 512, step-size is 0.1, and delay is 1 sample. The normalized LMS is slightly different than the LMS in that it weights the filter weight coefficient update by the energy in the input data [41]; practically this helps stabilize the filter.

Center Frequency	16.8GHz
Resolution	0.1524m
Scene Size	354m
Image Oversample Factor	1.5
Window Function	Taylor $\bar{n} = 4$ -35dB SLL

Table 3.1: LMS filter 1D simulation parameters

Figure 3.3 shows the radar signal contaminated with an interference signal, $x(n)$, in the top plot, the output of the filter, $y(n)$, in the middle plot, and the resulting filtered signal from subtracting the filter output from the original signal, $e(n)$, in the bottom plot. It should be evident the interference signal remains in the filtered signal, $e(n)$. The performance of the LMS filter is poor because the filter output contains too much of the original radar signal and not enough of the interference signal is estimated by the filter coefficients. From deramp processing, the interference is confined to the samples between approximately 1200 to 2000, while the filter output extends across the entire duration of the fast-time phase history, modifying every sample of data that does or does not contain interference. This modification of the radar signal may distort the image.

These filter parameters are most likely not optimal, but empirically changing their values has little effect on the overall results. However, to ensure that there is no error in the parameters and the implementation, a simulation is created where the same phase history data set is used, but now the interference exists over all of the fast-time samples. A complex sinusoid is added to the point target and clutter signal at a SIR of 0dB; the top plot of Figure 3.4 shows the interference signal now occupies all fast-time samples. The filter

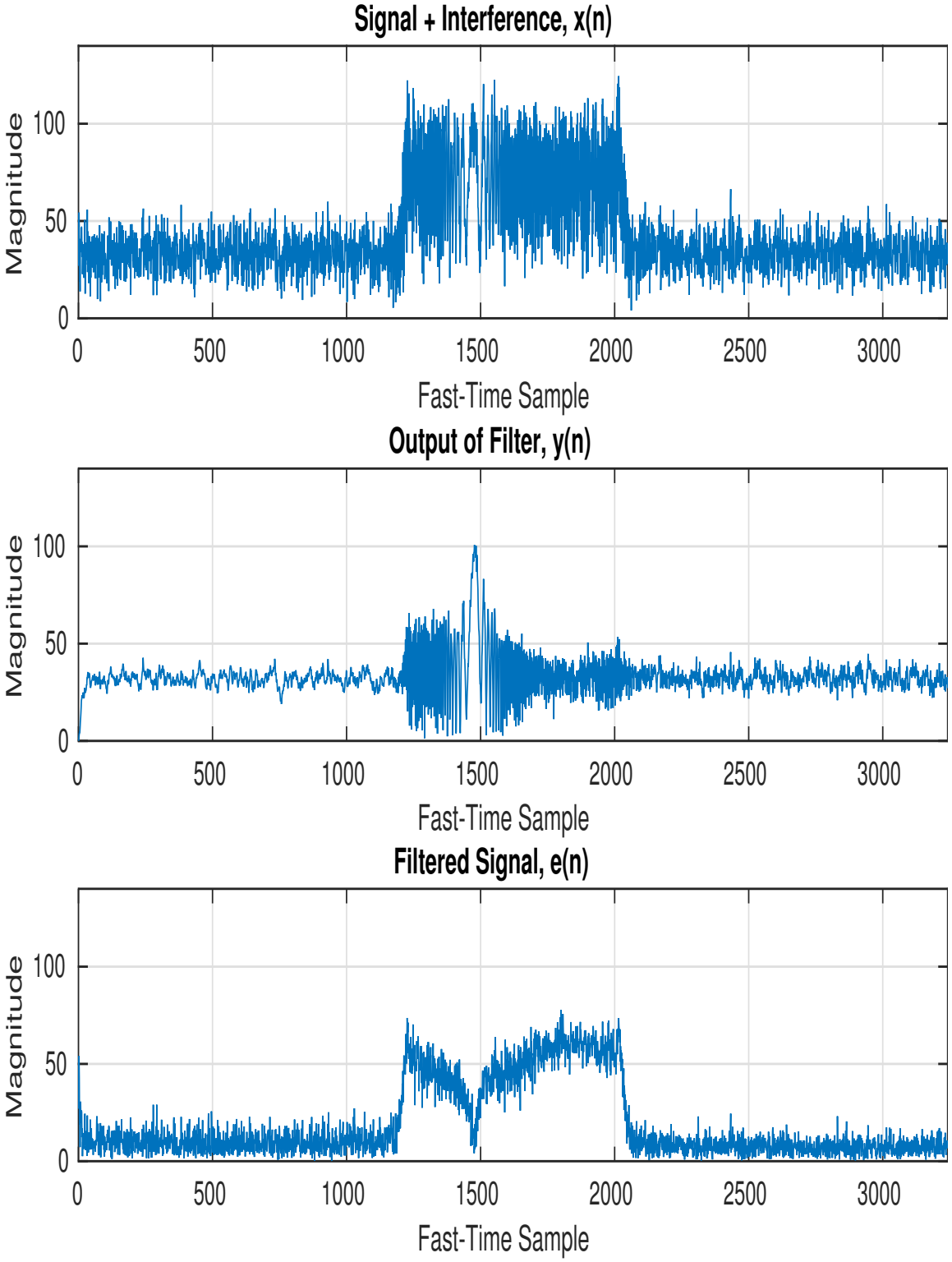

Figure 3.3: Normalized LMS filter results of a deramp radar for 15dB single target phase history in -13dB terrain/clutter with interference at a level of 0dB SIR.

output, $y(n)$, in Figure 3.4 (middle plot) shows the 'ramp-up' effect of the filter by the reduced magnitude in filter output from the starting data sample. This reduction results in un-suppressed interference signal in the first few samples of the filtered signal in Figure 3.4. But overall the LMS filter is able to remove the interference signal. It is curious to note that the signal level of the filtered signal in Figure 3.4 does not have the same magnitude as the original signal, shown in the top plot of Figure 3.3. However, the amplitude reduction effect consistent with [38] that reported similar amplitude reductions from using LMS adaptive filters.

3.9 Linear Predictor Filter

Another type of adaptive algorithm implementation is a linear predictor. Abend and McCorkle [28] use an autoregressive model for the interference that assumes the interference is a sinusoid. A MATLAB implementation was created to represent using a linear predictor filter. Figure 3.5 shows a block diagram of the implemented filter. First the linear predictor coefficients are estimated using MATLAB's signal processing toolbox function lpc. Then the filter coefficients are applied to the fast-time data samples, $x(n)$, to calculate an estimate of the interference within the fast-time data, $\hat{x}(n)$. Then the estimated interference is subtracted from the data to yield the filtered result, $e(n)$.

Applying the linear predictor to deramp data is not optimal because it is designed to identify sinusoids in data and the deramped radar signal itself is a summation of sinusoids. In fact, the deramped interference is a chirped sinusoid. If the data is deskewed, then the problem becomes finding the interference sinusoid of very short duration amongst the radar signal sinusoids. The linear predictor is conceptually very similar to the LMS filter but it differs in implementation by only requiring a single parameter, the filter order.

A simulation was created the same as the LMS filter example in the previous section, Figure 3.6 shows the results of applying an order 1 linear predictor to a 15dB single target phase history in -13dB terrain/clutter with an single tone interference source at a level of

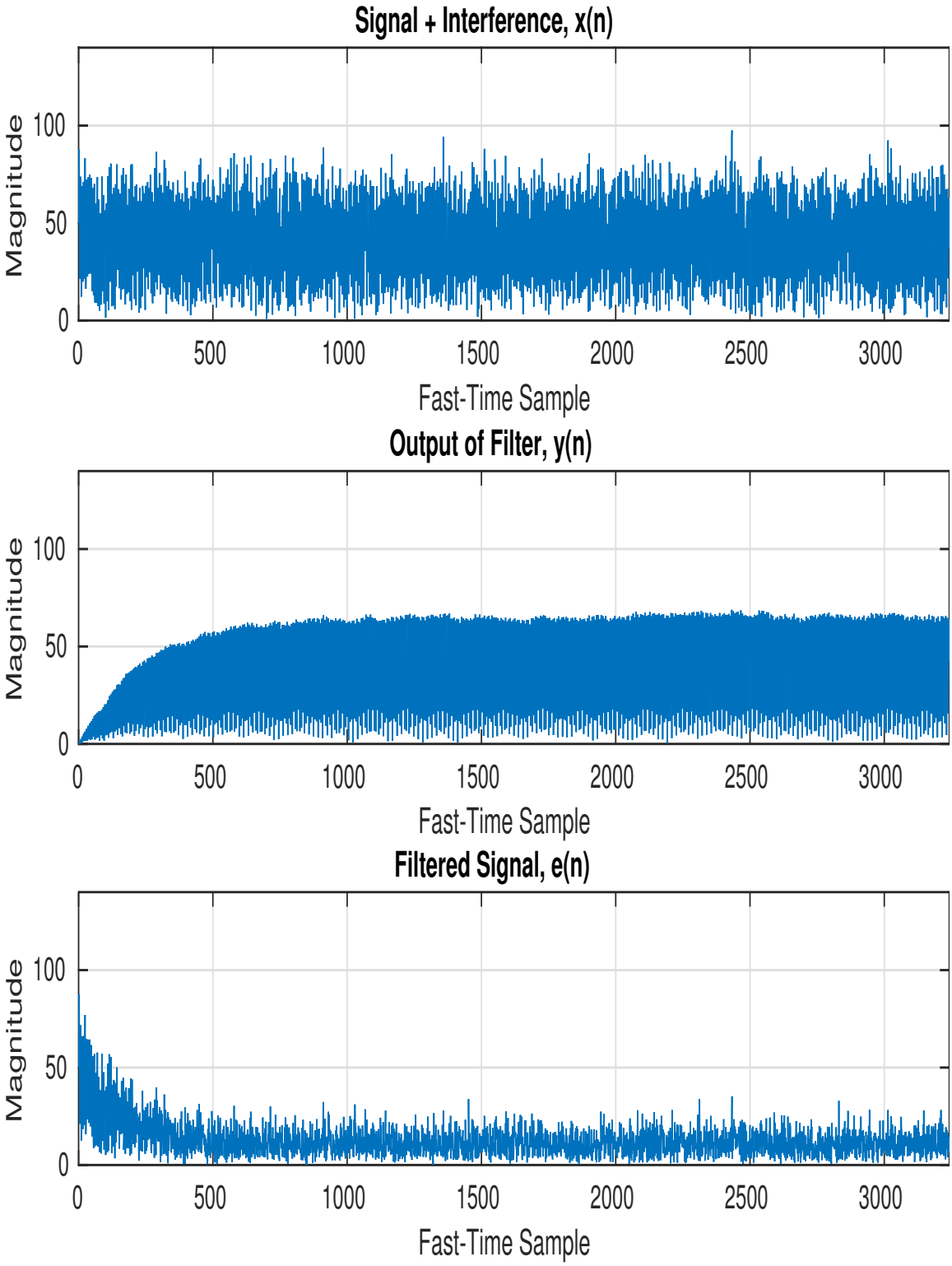

Figure 3.4: Normalized LMS filter results of a direct sample radar for a 15dB single target phase history in -13dB terrain/clutter with an interference source at a level of 0dB SIR.

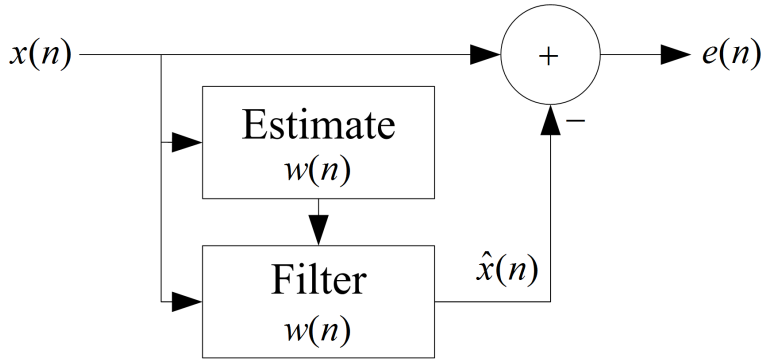

Figure 3.5: Block diagram of linear predictor filter implementation.

0dB SIR. The simulation parameters are identical to those used for LMS algorithm in Table 3.1. The simulation results are very similar to the LMS algorithm results in Figure 3.3.

To show how Abend and McCorkle's method [28] would work for a non-deramp radar, the interference source was replaced with a 1 MHz complex sinusoid with a duration over the entire fast-time data. Figure 3.7 shows that the filtered signal (in the bottom plot) has removed the interference because it is nearly the same magnitude as the data without interference in the top plot of Figure 3.6. Note that the linear predictor filtered signal has greater amplitude than the LMS filtered signal in Figure 3.4.

3.10 Standard Notch

A notch (or notch filter) in the phase history's spectral domain has been demonstrated to be effective at removing interference for direct sample SAR systems [21, 25, 42, 43]. A difficulty arises in applying the spectral notch to deramp SAR data in that the spectral filtering techniques to identify the frequency components of the interference use a Fourier transform of the data. A Fourier transform of a deramp SAR phase history yields the spectrum of IF frequencies and is also the range profile of the image. The chirp upon the interference signal from deramping spreads the interference signal across all IF frequencies (all ranges). An example of this is shown in Figure 3.8 where a single pulse of phase history data with and without interference has been Fourier transformed to reveal the IF spectrum (or range profile of the image). Comparing the two figures, the bright point targets are

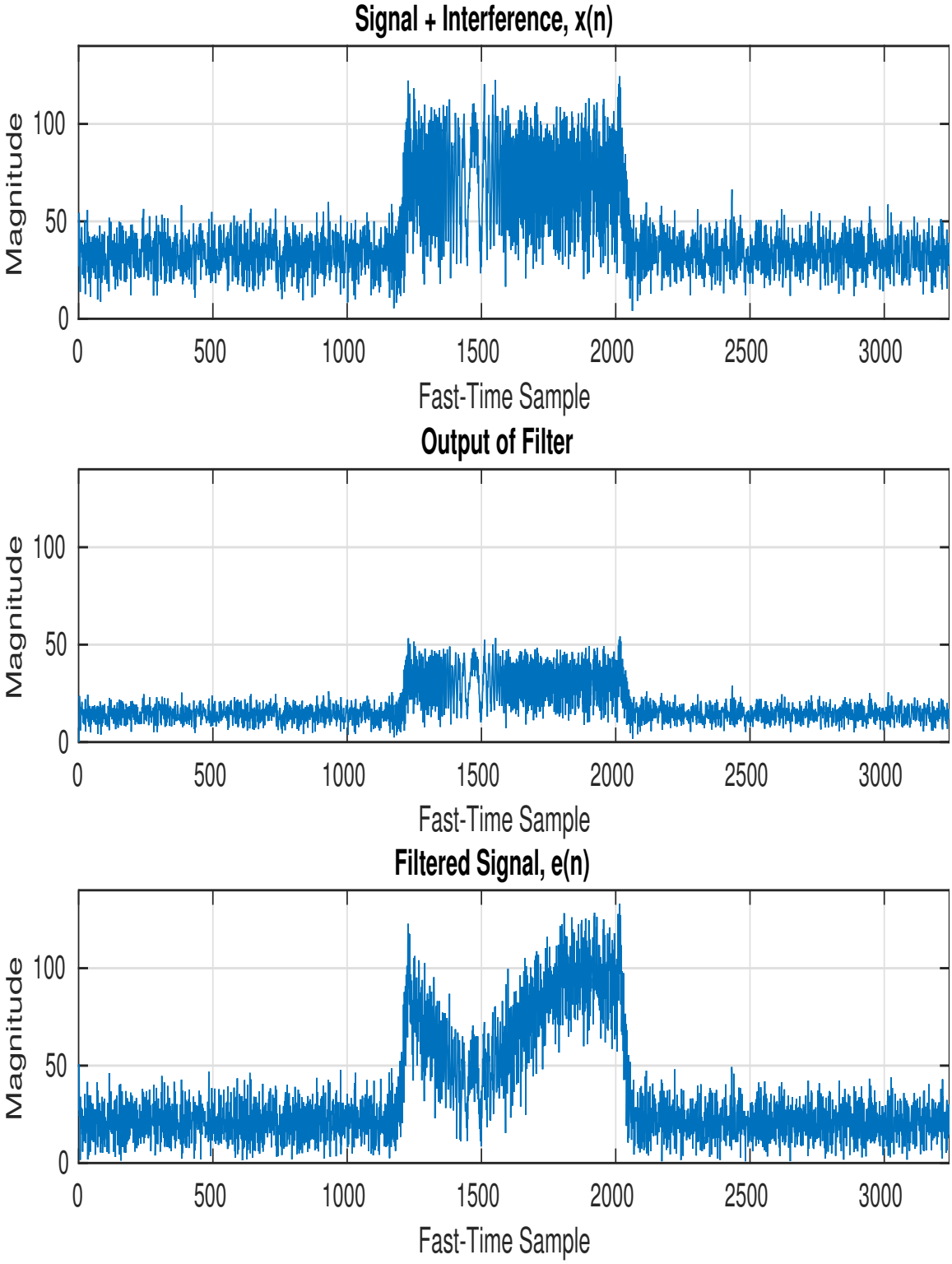

Figure 3.6: Linear predictor filter for stretch processing radar applied to 15dB single target phase history in -13dB terrain/clutter with interference at a level of 0dB SIR.

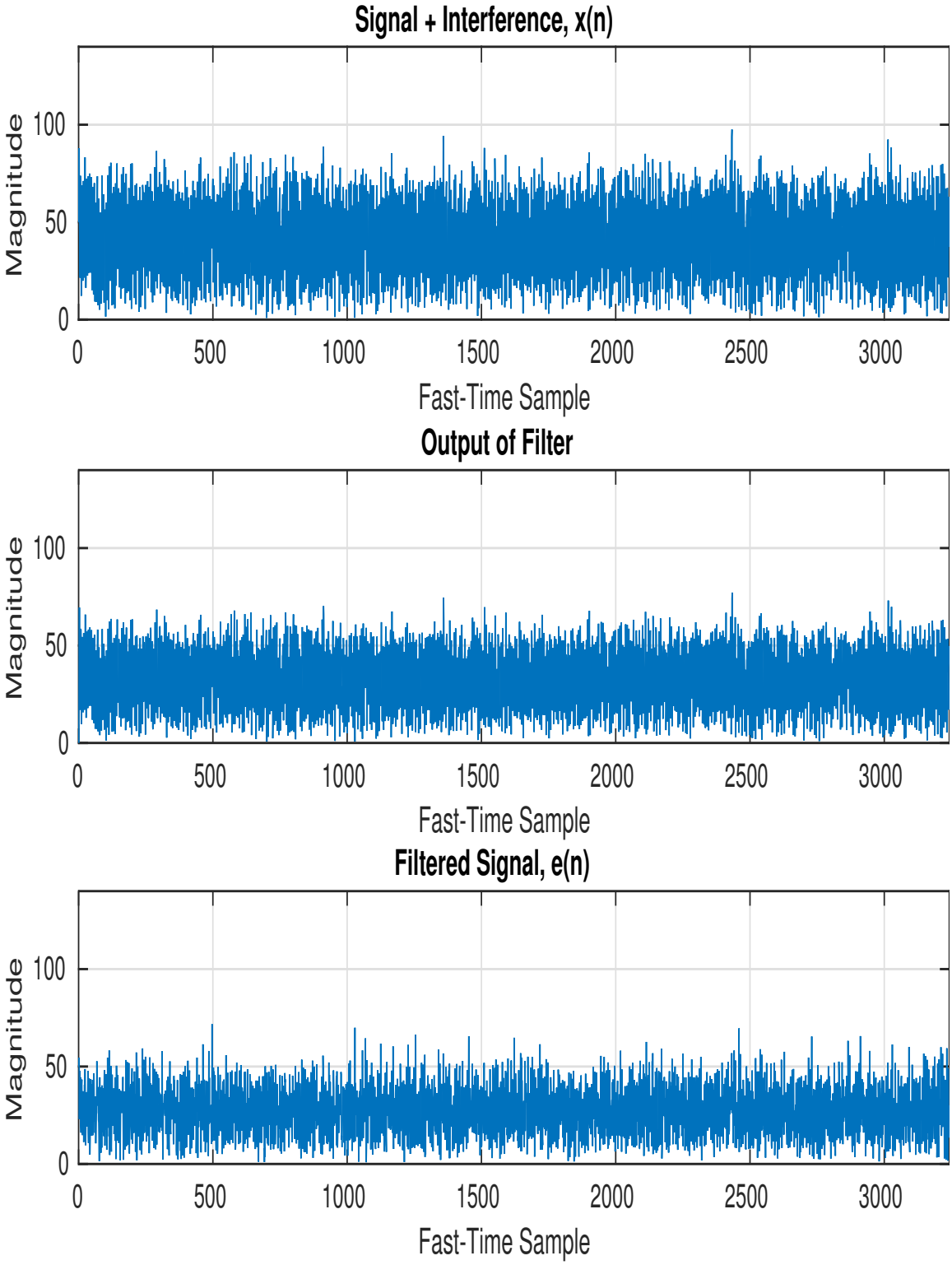

Figure 3.7: Linear predictor filter for direct sample radar applied to 15dB single target phase history in -13dB terrain/clutter with an interference source of 1MHz single sinusoid over full fast-time duration at a level of 0dB SIR.

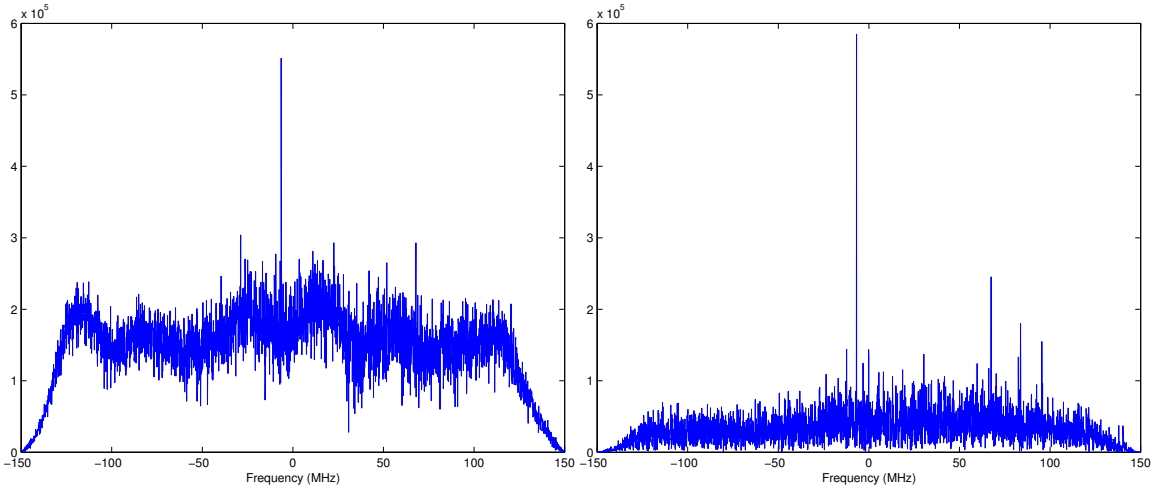

(a) With interference. **(b)** Without interference.

Figure 3.8: Comparison between the spectrum of phase history data (a) with and (b) without interference.

indicated by single spikes and appear in both figures, while in Figure 3.8a, the interference artifacts appear throughout the entire IF frequency band increasing the overall RCS of the image when compared to Figure 3.8b. Therefore identifying the frequency of interference for deramp data is not as straightforward as a Fourier transform.

For interference mitigation purposes, transforming the direct sample raw data into the spectral domain results in the interference signal occupying less data samples than in the time domain such that fewer data samples need to be notched. Deramp SAR data is nearly the opposite in that the interference occupies less samples in the time domain (i.e. fast-time) data samples. For deramp SAR, the best place to notch is the phase history domain.

For this dissertation the standard notch is defined as the notching approach used by Wahl et al. [13] for stretch processing radars where phase history data samples detected to contain interference are forced to a value of zero.

The standard notch requires an interference detector that makes a binary decision for each sample of data whether it contains or does not contain interference. Wahl et al. [13] describes a power threshold detector that identifies samples above a certain power as containing interference. An example of the magnitude of fast-time data samples containing

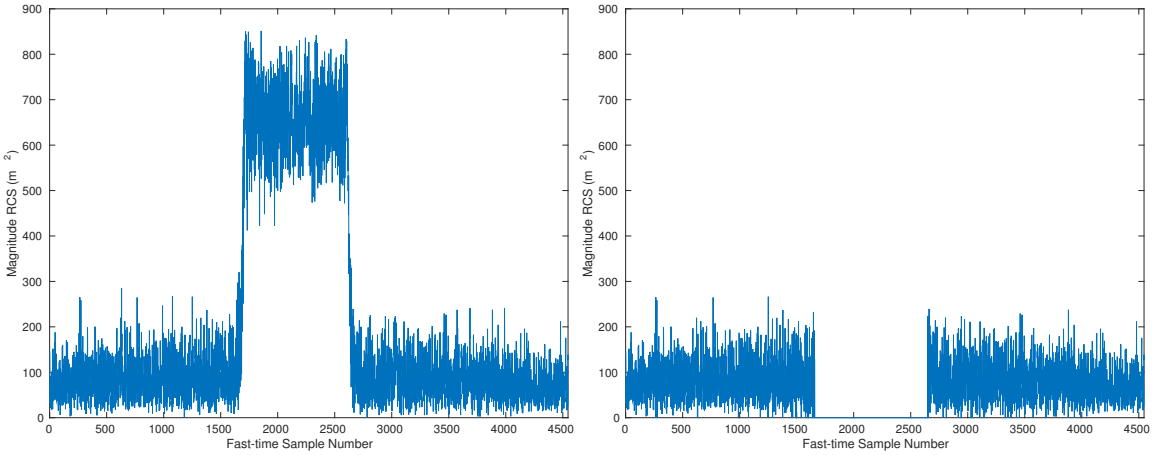

(a) Phase history data with interference **(b)** Standard notch applied

Figure 3.9: Example of applying the standard notch technique to deramp SAR data containing interference (a) before and (b) after.

interference is shown in Figure 3.9a where the interference is clearly visible as a dramatic increase in magnitude value extending from approximately sample numbers 1700 to 2700. Applying a power threshold detector as described in Wahl et al. [13] results in notching the large magnitude samples to zero, as shown in Figure 3.9b.

Because this dissertation is concerned with the coherence effects from the mitigation technique itself, it is sufficient to accept that a detector has determined that a certain percentage of samples at a particular location in the phase history contain interference.

Notching a few data samples is relatively benign to image quality. It is an accepted rule of thumb that notching less than 2% of the data samples is acceptable for radar systems [44]. Although there are probably other requirements, even for SAR, that ultimately determine the acceptable notching limit. To observe the effects of the standard notch upon a SAR image and its CCD, Figure 3.10 shows three cases: the first case has no notching applied, the second has 2% of samples notched, and the third case has 25% of samples notched. As more samples are notched, the image becomes darker due the signal power lost within the notch and the average coherence of the CCD image decreases. At 25% of samples notched the disturbance pattern from the vehicle is becoming difficult to identify and only gets worse as the notch increases. Eventually the notched image cannot be registered or

correlated to the previous image and no coherent data product can be produced.

3.10.1 Repairing Damage from Notch

There are many techniques available in the literature to repair the distorted IPR from notching. Wahl et al. [13] successfully repairs the IPR with a technique called CLEAN. CLEAN is a radio astronomy algorithm adapted to coherent microwave imaging to improve image quality [34]. The algorithm first assumes that the brightest pixel(s) in the image can be modeled as a point target. Then an ideal model of a point target response corrupted by a known mechanism (in this case the notch) is matched to the brightest pixel value and subtracted from the image. The process repeats until only pixel brightness values in the noise remain. The resulting summation of ideal point targets represents an image without noise and without IPR distortions. However for a SAR producing coherent data products the clutter is the most important feature of the image. Alternatively for SAR imaging, the summation of ideal point targets can be added back to the clutter/noise image to form a corrected image.

The CLEAN algorithm is successful at repairing point targets (as demonstrated in [13]), however CLEAN is unable to model SAR image terrain (or anything that isn't a point target). SAR image terrain is modeled as circular white Gaussian noise [4, 17], the same model as thermal noise. Therefore CLEAN cannot distinguish between clutter and thermal noise, and without a proper model for the clutter, CLEAN is unable to fit a model to the distorted data to repair the clutter IPR. For a SAR producing coherent data products, the clutter IPR and coherence is important to be able to resolve an accurate height map or to detect changes within the scene.

An example is shown in Figure 3.11 to illustrate the effect of applying CLEAN to the point targets of an image while the clutter remains distorted. For the image in Figure 3.11a point-like scatterers make up only a small portion of the image, and while CLEAN repairs the IPR of the point targets in the bottom left of the image by eliminating the range

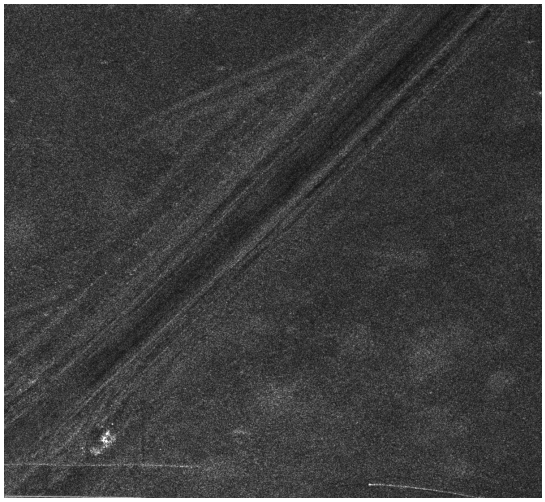

(a) Image, no samples notched

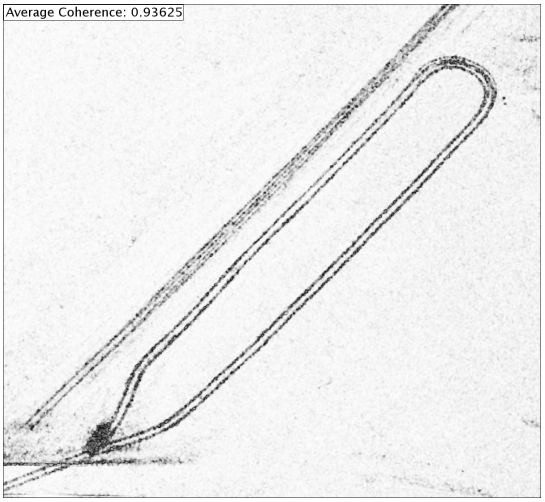

(b) CCD, no samples notched

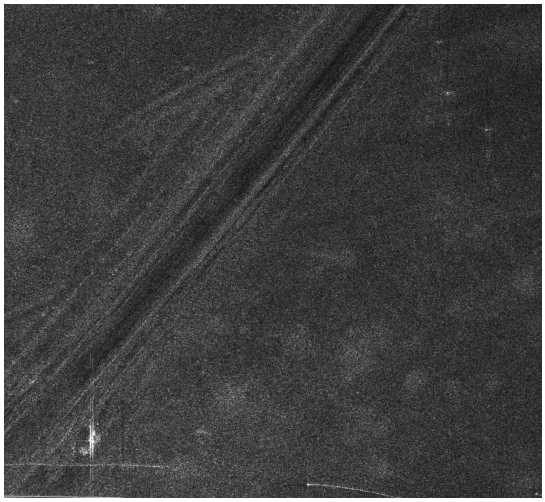

(c) Image, 2% samples notched

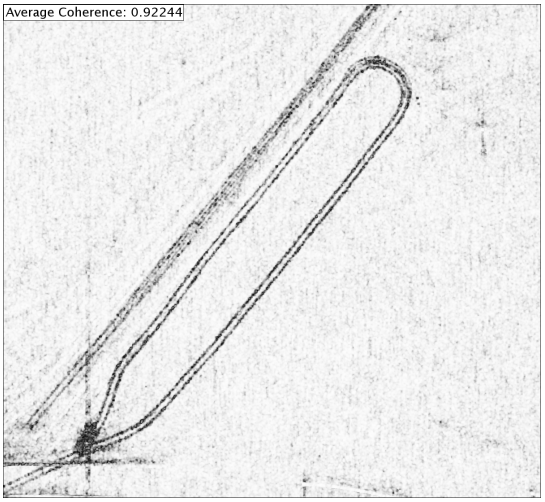

(d) CCD, 2% samples notched

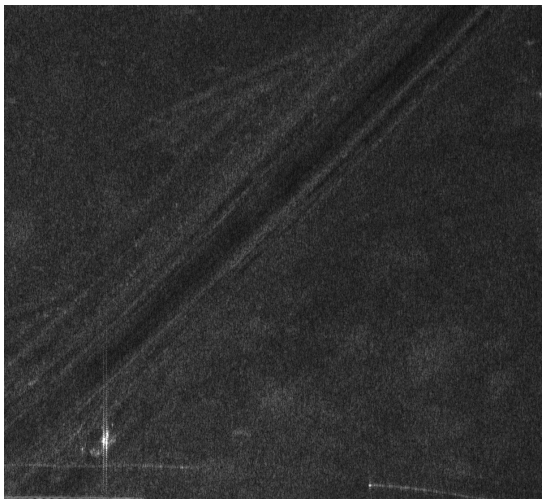

(e) Image, 25% samples notched

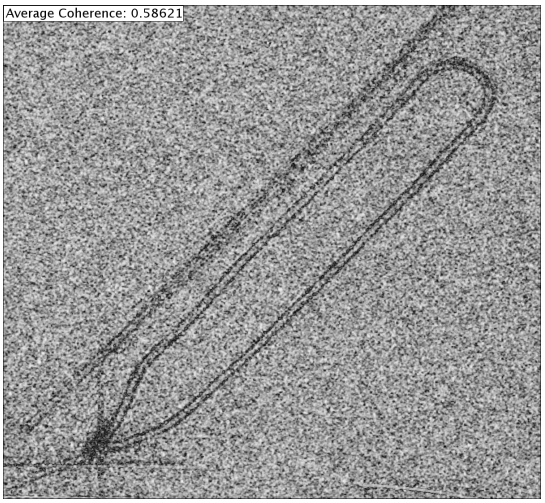

(f) CCD, 25% samples notched

Figure 3.10: Examples showing the effect of notching a SAR image and notching one image of a CCD image pair to mitigate interference.

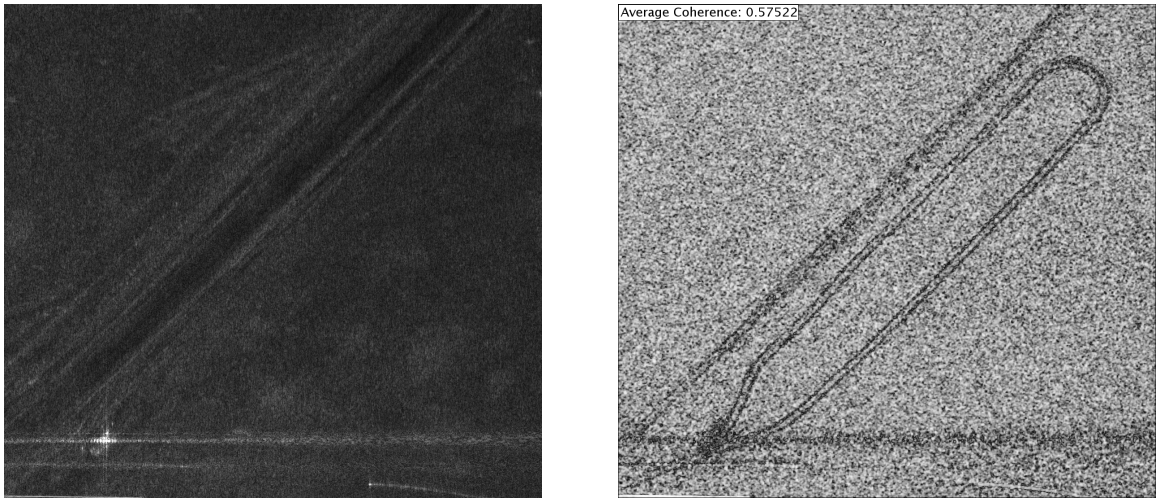

(a) Image repaired with CLEAN **(b)** CCD repaired with CLEAN

Figure 3.11: CLEAN applied to the second image of a coherent pair of images that has been notched 25% showing (a) the image and (b) CCD.

sidelobes (vertical streaks in Figure 3.10e are removed), the clutter/terrain in the rest of the image remains distorted. The CCD in Figure 3.11b is formed from another image from a previous pass without interference and confirms that the clutter is indeed distorted by comparing the overall coherence value to the 25% notch case in Figure 3.10f.

3.11 Summary

In this section, the mechanism for coherent product degradation by interference has been revealed as an additive, SINR loss that doesn't distort the image IPR. At a particular point this SINR loss needs to be mitigated to restore coherence. A few standard methods were demonstrated that do and do not apply to deramp SAR systems. It was shown that these mitigation methods themselves distort the image IPR and lower the average coherence. Attempts to repair the IPR distortion from interference mitigation for the clutter/terrain within the image are unsuccessful. This dissertation will explore in the following chapters the mechanisms and mitigation methods to improve or restore coherence.

CHAPTER 4

PERFORMANCE METRICS

The evaluation of the quality of second-order products (i.e. CCDs) can be highly subjective. It really depends on who is looking for what features under a particular set of conditions. A major factor in the quality measure can be attributable to maximizing the average coherence value. However, maximizing the average coherence value is not a sufficient quality metric by itself. Coherence measures the 'sameness' between two images; it matters little if each image has a 'good' IPR so long as the IPR is the same. To compare the effectiveness of different interference mitigation techniques, this dissertation will use several quantitative measures. These metrics include IPR, average magnitude coherence, and a statistical contrast metric. Each metric has particular strengths and weaknesses that will be discussed in detail throughout this chapter.

4.1 IPR

Inevitably, the image IPR is disturbed when the phase history samples are modified. Depending on how the phase history samples are modified results in a desirable or undesirable IPR according to the radar system specifications. The ideal IPR for a deramp SAR image is the result of a multiplication of a constant tone with a rectangular window that results in a sinc function after applying a Fourier transform. The rectangular window represents the finite sampling of the constant tone. Typically, the -13dB sidelobes of the resulting sinc are judged to adversely affect image quality and a window function is applied to the data to reduce sidelobe level [9, 10, 15].

Any effective perturbations to the amplitude of the phase history data resulting from

interference mitigation affect the sidelobe level and structure in a similar way to a window function. Exactly how the IPR is affected is complicated to predict [15], but quantifiable by typical IPR measures including peak sidelobe level (PSLL), mainlobe width, and integrated sidelobe ratio (ISLR). Each of these measures are technically explained in section 2.5. Mainlobe width is directly related to image resolution and the choice of window function or perturbations to the phase history envelope from interference mitigation can increase the mainlobe, introduce ripples, and decrease effective image resolution. PSLL is a measure of the highest sidelobe level and usually indicates how bright the sidelobes of each reflection will appear. If the PSLL is above or close to the average surrounding values, then the sidelobe itself can be visible and indicate a false target or obscure a dimmer target. ISLR is a measure of the average sidelobe level and can indicate how clearly a target can be resolved. ISLR is related to PSLL, but different in that it is a measure of total energy within the sidelobes of a scatterer response. If the ISLR is a small value, most of the energy from the scatterer is located in the mainlobe and the scatterer will be easier to localize. However, if the ISLR is large $(> 0\text{dB})$, then the sidelobes have as much or more energy than the mainlobe and it can be difficult to localize the position of the scatterer.

For situations where a large amount of the data is perturbed, ISLR may not be a reliable predictor of image quality. ISLR requires defining a mainlobe separate from the sidelobe; it becomes difficult to isolate one from the other as the sidelobes increase and the mainlobe distorts. Typically, the first nulls of the IPR define the mainlobe, but if the mainlobe is distorted, as shown in Figure 4.1a and Figure 4.1b, the mainlobe width can be less than 'normal' therefore some mainlobe energy is counted as sidelobe energy. This phenomenon becomes important when evaluating image quality to localize a target. Although Figure 4.1a has a lower ISLR, the corresponding image in Figure 4.1c shows the target as a bright streak where it is difficult to locate the target or identify any nearby targets. While the higher ISLR in Figure 4.1b shows that the total energy outside of the first nulls is higher, the overall level of the far sidelobes is much lower than Figure 4.1a. Figure 4.1d shows the

lower sidelobes at far distance from the point target can help to localize the point target and resolve nearby scatterers.

4.2 Average Magnitude Coherence

As previously shown in section 2.7 the coherence estimator produces a complex value. When averaged over an area, or the entire image, the magnitude of the coherence estimator can be used as a metric for the similarity between images. For example, average magnitude coherence can compare the performance of different image processing algorithms against a true, or optimal result [45]. Additionally, maximizing coherence is important to IFSAR performance [4].

Coherence encompasses many data collection and signal processing factors, including choice of window function and flight geometry [17, 18]. In the case of interference, several mechanisms can reduce coherence depending on the chosen detector and mitigation method. The aforementioned references are guides to understanding the underlying mechanisms in a synthetic radar system that impact coherence. The absolute performance (i.e. maximum achievable coherence) can only be judged for a particular radar system, imaging a particular target, and interpreted by a particular detector. Coherence is a multiplicative factor of individual loss factors that can be represented as a product of the individual coherence loss factors [4, 17, 46]:

$$\mu = \mu_{snr} \cdot \mu_{temporal} \cdot ... \mu_{ipr}, \tag{4.1}$$

where the coherence due to SNR is represented by μ_{snr}, $\mu_{temporal}$ is the coherence due to temporal changes between images, and μ_{ipr} is a loss due to IPR mismatch. There are many more coherence loss factors for a real SAR system than are represented here that can be found in the literature [4, 17, 18, 46].

This dissertation evaluates the coherence impact related to the signal processing op-

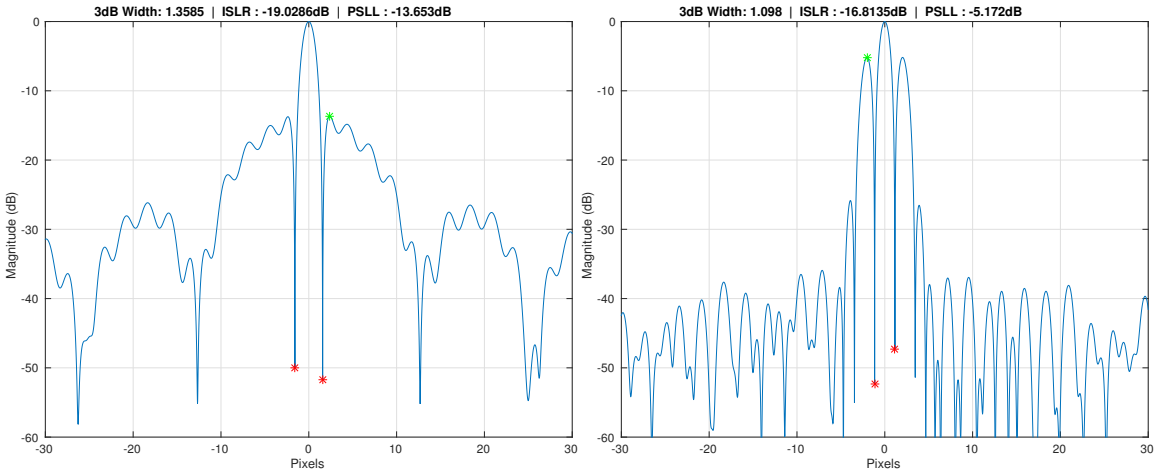

(a) Low ISLR **(b)** High ISLR

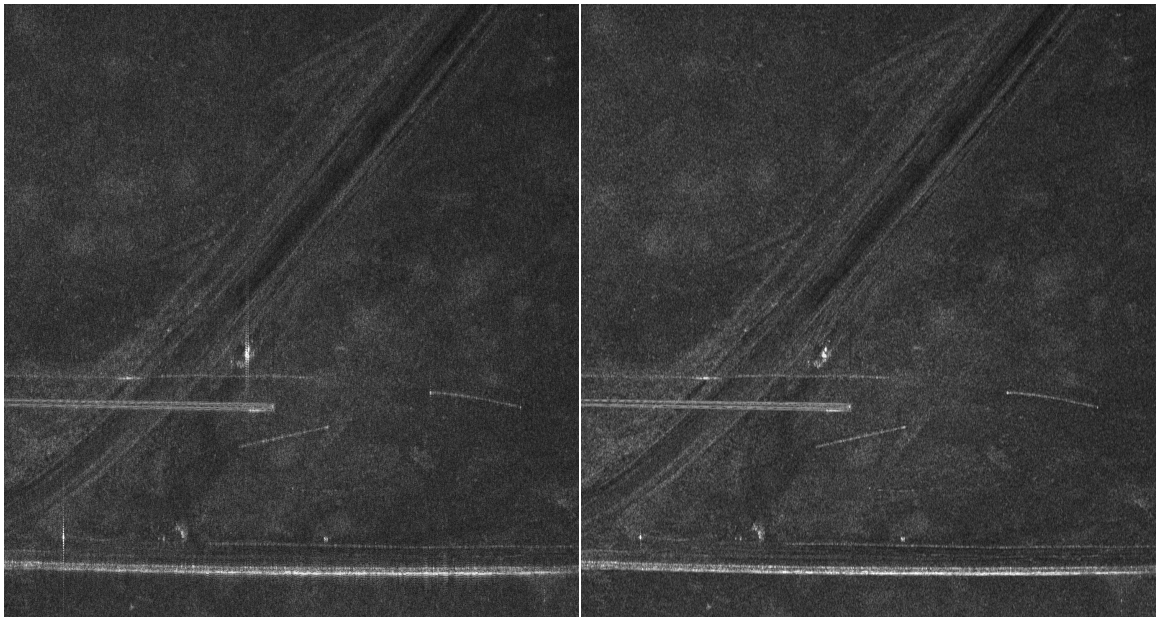

(c) Low ISLR **(d)** High ISLR

Figure 4.1: Example showing a lower ISLR does not necessarily mean a target is better localized than a high ISLR when phase history is distorted.

erations to mitigate interference. Therefore, only the relative performance between each mitigation method, all other factors being equal, is important to compare different mitigation techniques. While the literature [4,17,18] discusses and analyzes methods to maximize coherence, this dissertation needs only to compare the relative coherence impact of the different mitigation methods; the absolute maximum achievable coherence of the radar system matters little when comparing the performance of different mitigation methods.

For this dissertation all of the system coherence losses are held constant and combined into one term, μ_x, for all comparisons such that the final coherence impact is attributable to the mitigation itself and expressed as

$$\mu = \mu_x \cdot \mu_{mitigation}, \tag{4.2}$$

where $\mu_{mitigation}$ term encapsulates the coherence impact of the mitigation method. All effort in this dissertation will be to measure the change in coherence of the $\mu_{mitigation}$ term.

The $\mu_{mitigation}$ term encapsulates many facets of image quality and coherence, including IPR quality and SNR. A straightforward measurement of the average magnitude coherence value is a direct method of quantifying the value of $\mu_{mitigation}$ when all other factors are equal. Image simulations of synthetic clutter are helpful to remove the coherence losses associated with phase errors from motion, autofocus, and registration differences.

Within image simulations, the SNR value of the system is precisely controlled by adjusting the clutter and noise variance. However, a reduction in average coherence magnitude due to SNR can be observable due to the additional energy from the interference signal. It is well documented in [9, 17] that the SNR, or in the case of interference the SINR, has a direct relationship to coherence. When comparing multiple mitigation techniques, the average magnitude coherence value can indicate a level of un-mitigated interference by a lower SINR.

Another mechanism for reduced average magnitude coherence is a difference between

image IPRs from the mitigation method. Bickel [17] discusses the many factors that can cause IPR mis-match between images. Different interference mitigation techniques contribute in different ways to the mechanisms described in [17]. But the overall effect of the mitigation that is important is the cumulative coherence loss because it may limit the achievable coherence of the radar system.

Maximizing coherence is important, but the true coherence value itself is an important performance indicator of the maximum likelihood coherence estimator. Bickel [17] shows that high coherence reduces the bias and variance of the coherence estimator. But it requires particular applications to determine if a certain level of coherence is sufficient. For example, IFSAR applications use the coherence magnitude as an indicator of the quality of an IFSAR pair [4] by indicating the amount of phase noise. Phase noise directly translates to inaccuracy in height estimates; the lower the coherence, the noisier the phase, the more error in the height values.

While average magnitude coherence can indicate similarity between images, it cannot measure image quality in all cases. It is possible to get high coherence from poor images, and likewise low coherence from high quality images. The IPR metrics can quantify image quality when compared against an ideal IPR, but it is another matter if the image meets system specifications. For CCD applications to be useful the changed regions need to be distinguishable from the unchanged regions. Maximizing coherence will primarily affect the unchanged regions; leaving the changed regions dominated by temporal decorrelation. Interpretation of the distinction between changed and unchanged regions can be highly subjective, so there should be a contrast metric to quantify the separation between regions.

4.2.1 Measuring Average Coherence

The actual computation of average coherence is a straightforward sample mean of the magnitude of the coherence value estimates. However to compute the coherence estimate using equation (2.15) requires setting the number of local averaging pixels, N, and a large

enough image to achieve a stable estimate of the average coherence. It has been the author's experience that coherence value deviations on the order of thousandths are difficult to observe with the eye, therefore an image size is desired that allows deviation on the order of thousandths.

A simple simulation was created to compute the average magnitude coherence as a function of image size. The clutter power was set at -28dB and the noise level set to -38dB yielding a 10dB SNR. The ideal coherence value is calculated according to [17]

$$\mu_{SNR} = \frac{\text{SNR}}{\text{SNR}+1}, \tag{4.3}$$

which using a 10dB SNR calculates a coherence value of 0.9091. The clutter and noise statistics both follow circular white Gaussian statistics and were computed independently for each image calculation 96 times for each image size. The simulation was repeated 3 times to test the effect of changing the number of local pixels used in the coherence estimator. Figure 4.2 shows the results of the simulation for local pixel averages of 25, 49, and 81 pixels. As the number of local pixels averaged increases, the bias in the coherence estimate is reduced as predicted in [17]. Furthermore, by evaluating 96 cases for each image size a reasonable estimate of the standard deviation can be made. Figures 4.2b, 4.2d, and 4.2f show the coherence deviation amount for 3 standard deviations about the mean value. According to Figures 4.2b, 4.2d, and 4.2f, an image size of 100m by 100m is sufficient.

4.3 Statistical Contrast Metric

A CCD can indicate which parts of the image have changed and not changed in the time between two data sets were collected. The contrast of the CCD can determine how clear this distinction can be made by any given detector. Intuitively humans can use grayscale color values mapped to coherence values to distinguish between areas of change and no change. To develop a quantitative contrast measure, first it is necessary to re-examine how

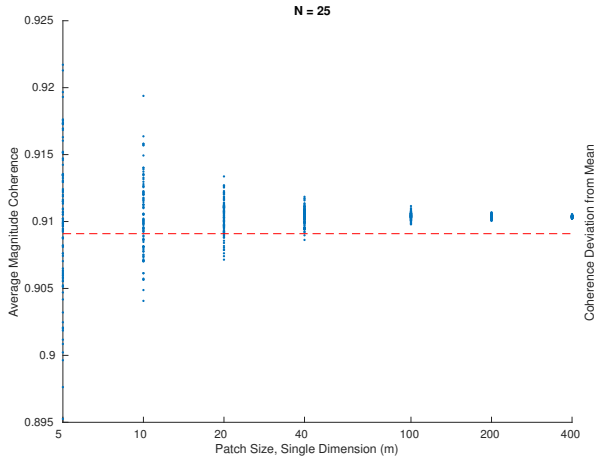

(a) Scatter plot of estimated coherence, N=25

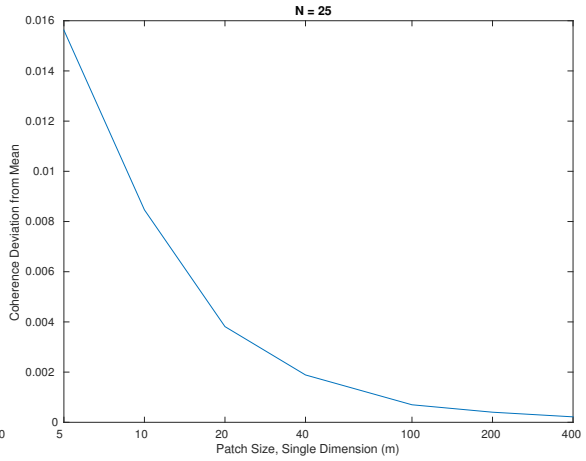

(b) Deviation from mean coherence, N=25

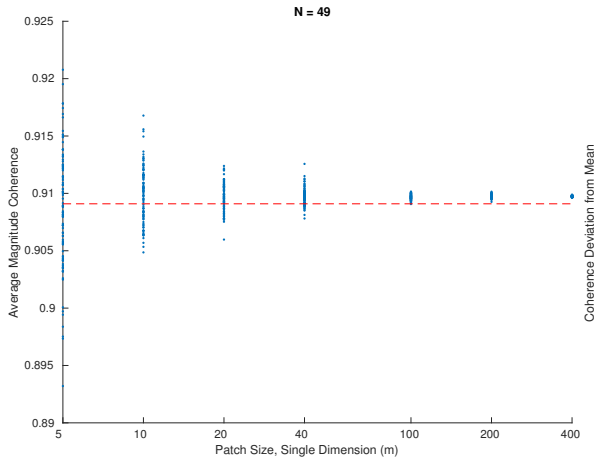

(c) Scatter plot of estimated coherence, N=49

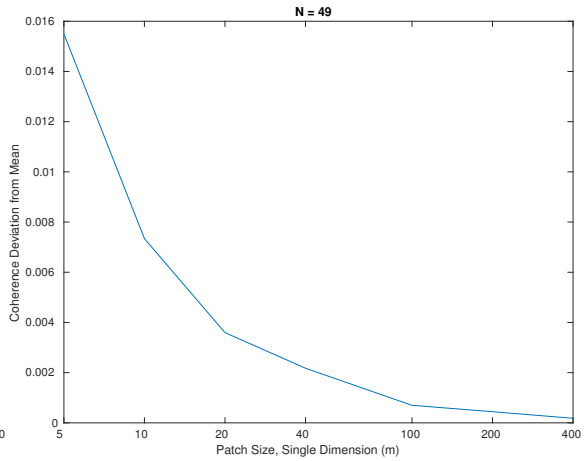

(d) Deviation from mean coherence, N=49

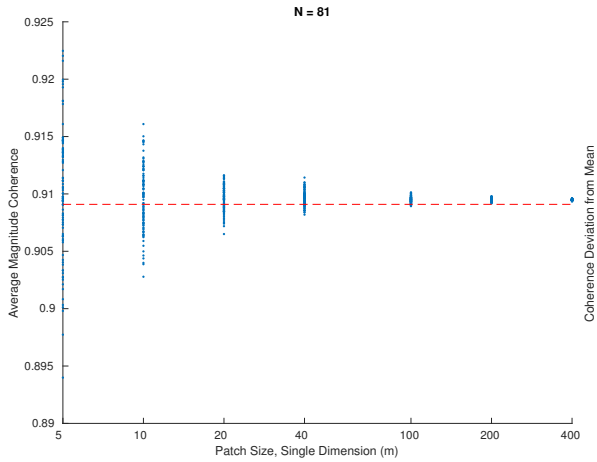

(e) Scatter plot of estimated coherence, N=81

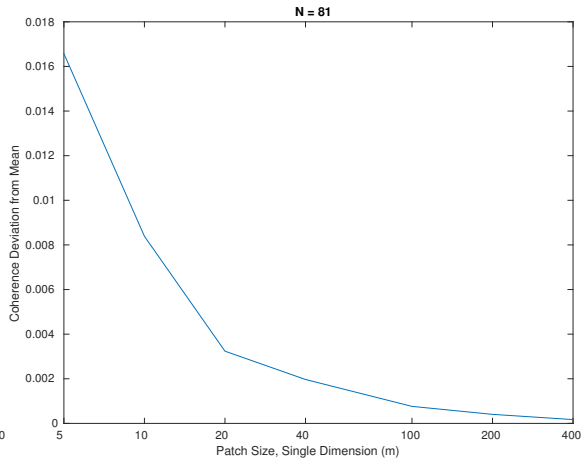

(f) Deviation from mean coherence, N=81

Figure 4.2: Simulation of the effect of the local averaging window size and image size upon the bias and variance of the average magnitude coherence sample mean estimator.

the coherence estimator is influenced by changes. An excellent model for SAR images containing general terrain features is circular white Gaussian noise (CWGN) [4, 4]. Under this model, the coherence estimator can be modeled according to the following probability density function (PDF) [17]:

$$p(\hat{\mu}|\mu_o, L) = 2(L-1)(1-\mu_o^2)^L \hat{\mu}(1-\hat{\mu}^2)^{(L-2)} {}_2F_1\left(L, L; 1; \hat{\mu}^2\mu_o^2\right), \tag{4.4}$$

where $\hat{\mu}$ is the estimated coherence value (and random variable), μ_o is the true coherence, L is the effective number of looks, and ${}_2F_1$ is a hypergeometric function. Note that the coherence estimator PDF in equation (4.4) depends only upon the true coherence, μ_o and the effective number of looks, L. If no change is present from one image to the other, its true coherence will be a value of 1. If a completely decorrelated change is present, its true coherence will be a value of 0. Whether the number of effective looks is the same or not, the true coherence value for each case has defined two separate PDFs. These PDFs are somewhat unique in that the independent variable, true coherence, μ_o, and the dependent variable, estimate of coherence, $\hat{\mu}$, are both limited to the interval $[0, 1]$. An example of these two PDFs are plotted in Figure 4.3a.

To distinguish between a change and a no change area in CCD products, essentially there must be adequate separation between these two PDFs. Adequate is a very relative term that depends on what is desired to be observed, and how the image is scaled. For this dissertation's purposes a non-specific, general and quantitative measure is the best choice to compare relative performance, because fundamentally it is the separation between the change and no change PDFs that determine the limit to identifying change for any detector.

A straightforward approach to measure the difference between the change and no change cases is to compute the difference between the peak or mean values for each PDF. Or, more directly, the difference between the peak or mean coherence value of each region in the image. In theory, the larger the difference between the two numbers, the better the dis-

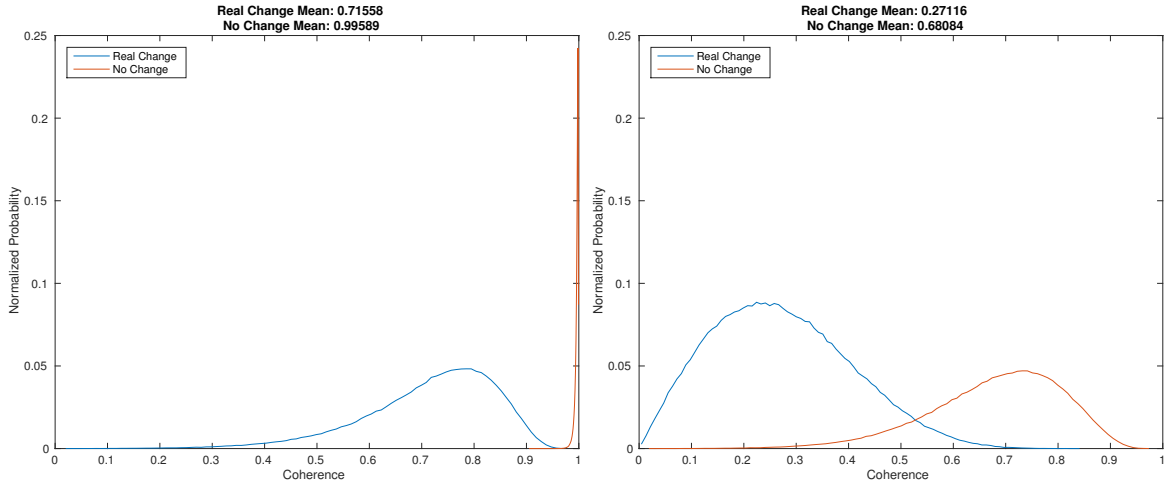

(a) No mitigation applied **(b)** Notch mitigation applied

Figure 4.3: Comparison between coherence PDFs for change and no change cases for (a) when no mitigation is applied and (b) a notching mitigation is applied to 27% of samples.

tinction between the change and no change cases. Figure 4.3 shows an example where the better contrast is actually indicated by the lower difference between peak and mean coherence values. In Figure 4.3a the difference between mean values is 0.27808 and there is an extremely clear distinction between the changed PDF and the no change PDF coherence values because there is very little overlap in their coherence values. However, in Figure 4.3b the difference between the mean values increases to 0.41 although it is not clear if coherence values between 0.4 and 0.6 represent changes or the absence of change. This example illustrates that the peak or mean value is not sufficient to characterize the overlap between the PDFs and another approach is necessary.

To truly quantify the separability between change and no change, the metric needs to account for both a changing mean and variance values. Adopting the scene change model in [47,48], the case where no change occurs between images is called the null hypothesis, H_0, and the case where change occurs is the alternative hypothesis, H_1. To simplify evaluation of each distribution, it is assumed that the change case has a true coherence value of 0 and the no change case has a true coherence of 1. Fitting the coherence estimator PDF to a histogram of CCD image values makes it possible to quantify the PDF overlap region

above or below any given threshold value by integration of the PDF. The problem becomes choosing the right threshold in the interval $[0,1]$ to compare all mitigation methods.

A single threshold value is not sufficient because all that matters in making comparisons between interference methods is the separation of the two PDFs despite changing peak/mean values and changing variance. Radar engineers address this issue by setting a constant false alarm rate from which to calculate a threshold. The threshold set by the constant false alarm rate is robust against mean and variance changes for the individual distributions. Again, the same problem for choosing a threshold appears in choosing a probability of false alarm. The probability of a false alarm, P_{fa}, is the area of the no change PDF between zero and the threshold value; this should be minimized. The probability of detection, P_d, is the area of the change PDF between zero and the threshold value; this should be maximized. Ideally each PDF would exist completely on either side of the threshold value so that $P_d = 1$ and $P_{fa} = 0$, but this is not always the case. To get around the limitation of choosing a particular threshold value and preserve the generality of the comparison, it is possible to express the P_d as a function of P_{fa}; this plot is called a receiver operating characteristic (ROC) curve. It relates two PDFs by the area of each PDF according to a varying threshold. Computing the ROC begins with the PDF of the null hypothesis, the probability of a false alarm is

$$P_{fa} = \int_0^{\gamma} p\left(\hat{\mu}|\mu_0, L\right) d\hat{\mu}, \tag{4.5}$$

where the limits of this expression at first glance may seem backwards from the typical P_{fa} expression that integrates from a threshold value, γ, to ∞. However, these are coherence PDFs so the alternative hypothesis occupies lower values of coherence than the null hypothesis. Also, remember the threshold values are bound within the interval $[0,1]$. The integration of equation (4.5) can be tricky because of the hypergeometric function, ${}_2F_1$, in equation (4.4). One analytical method begins by first transforming the coherence PDF into

the magnitude-squared coherence PDF [49]. The magnitude-squared coherence function is expressed as the square of equation (2.15) [49]

$$|\hat{\mu}|^2 = \frac{\left|\sum_{n=1}^{L-1} x_{1,n} x_{2,n}^*\right|^2}{\sum_{n=1}^{L-1} \left|x_{1,n}\right|^2 \sum_{n=1}^{L-1} \left|x_{2,n}\right|^2}. \tag{4.6}$$

To find the transformation between these PDFs and properly distinguish between the square of the magnitude coherence random variable and the magnitude-squared coherence random variable, the following definitions are made to use different letters for each random variable

$$\begin{aligned} p(x) &= p\left(\hat{\mu}|\mu_o, L\right), \\ p(y) &= p\left(\hat{\mu}^2|\mu_o, L\right). \end{aligned} \tag{4.7}$$

Then the PDFs can be transformed according to

$$p(x) = T\left(p(y)\right), \tag{4.8}$$

where T is some transformation that can be found by equating each random variable's cumulative distribution function (CDF) in the general form

$$p(x) = \frac{d}{dx} \int_{-\infty}^{y=T(x)} p(y) dy. \tag{4.9}$$

Applying the PDF limits of the interval $[0, 1]$ replaces the lower integration limit with zero. Since it was previously defined $x = |\hat{\mu}|$ and $y = |\hat{\mu}|^2$, then $y = x^2$ replaces the upper integration limit. Now the PDF transformation expression becomes

$$p(x) = \frac{d}{dx} \int_{0}^{x^2} p(y) dy. \tag{4.10}$$

Notice that the integral now becomes the CDF of $p(y)$ at the value of x^2, or $P(x^2)$. By

definition, the derivative of a CDF is the PDF, and applying the chain rule to compute the derivative of $P(x^2)$ results in equation (4.10) expressed as

$$p(x) = p(x^2)2x. \tag{4.11}$$

Now substituting back into the expression $x^2 = y$ and rearranging yields the PDF of the magnitude-square coherence to be

$$\begin{aligned} p(y) &= \frac{1}{2x}p(x), \\ p\left(\hat{\mu}^2|\mu_o, L\right) &= (L-1)(1-\mu_o^2)^L(1-\hat{\mu}^2)^{(L-2)}{}_2F_1\left(L, L; 1; \hat{\mu}^2\mu_o^2\right). \end{aligned} \tag{4.12}$$

It may not appear much has been done toward solving the integral in the P_{fa} expression in (4.5), however notice that because of the properties of the magnitude coherence PDF, the expression for P_{fa} is an expression of the magnitude coherence CDF. The CDFs between the magnitude coherence and magnitude-squared coherence can be related by going back to (4.10) and rearranging into

$$\begin{aligned} \int_0^x p(x)dx &= \int_0^{x^2} p(y)dy, \\ \int_0^x p(x)dx &= \int_0^y p(y)dy, \\ P(x) &= P(y). \end{aligned} \tag{4.13}$$

Therefore, the CDF of the magnitude-squared coherence is the same as the CDF of the magnitude coherence. while the CDF of the magnitude coherence is not solved, the CDF of the magnitude-squared coherence is a known expression [49]. Fisher [50] derived the magnitude-squared CDF from the magnitude-squared PDF into a closed-form solution by assuming the number of looks is an integer value. Using the magnitude-squared CDF result

from [50] the P_{fa} expression becomes [49]

$$P_{fa}(\gamma) = \left(\frac{1-\mu_o^2}{1-\mu_o^2\gamma^2}\right)^L \gamma^2 \sum_{k=0}^{L-2} \left(\frac{1-\gamma^2}{1-\mu_o^2\gamma^2}\right)^k {}_2F_1\left(-k, 1-L; 1; \mu_o^2\gamma^2\right). \tag{4.14}$$

According to [48], (4.14) can be simplified further by making the following substitutions

$${}_2F_1\left(-k, 1-L; 1; \mu_o^2\gamma^2\right) = \left(1-\mu_o^2\gamma^2\right)^{k+L} {}_2F_1\left(1+k, L; 1; \mu_o^2\gamma^2\right), \tag{4.15}$$

using the hypergeometric transformation formula 15.3.3 in [51]. Therefore, a final expression of P_{fa} becomes [48]

$$P_{fa}(\gamma) = \gamma^2(1-\mu_0^2)^L \sum_{k=0}^{L-2} (1-\gamma^2)^k {}_2F_1\left(1+k, N; 1; \mu_0^2\gamma^2\right). \tag{4.16}$$

Likewise, the probability of detection can be computed in a similar manner using the alternative hypothesis

$$P_d = \int_0^{\gamma} p\left(\hat{\mu}\,|\mu_1, L\right) d\hat{\mu}, \tag{4.17}$$

where the same limits of integration are used because the alternative hypothesis is the case where change has caused a decrease in coherence and is detected as a change once it is less than the threshold, γ. Therefore, the expression for P_d as a function of threshold is

$$P_d(\gamma) = \gamma^2(1-\mu_1^2)^L \sum_{k=0}^{L-2} (1-\gamma^2)^k {}_2F_1\left(1+k, N; 1; \mu_1^2\gamma^2\right) \tag{4.18}$$

where this is exactly the same expression as (4.16) except the true coherence value of the null hypothesis, μ_0, has been replaced by the true coherence of alternative hypothesis, μ_1.

Now that P_{fa} and P_d are expressions of the threshold value, numerical methods can solve for threshold values according to discrete values of P_{fa}, which can then be used to compute P_d. This creates a relationship between P_d and P_{fa} that can be expressed in a ROC curve. The value of P_d shown for a particular value of P_{fa} represents a constant area of

the null hypothesis, so if there are multiple mitigation techniques, where each technique affecting the PDFs differently, the ability to detect a change is directly comparable by holding the area of the null hypothesis curve at a constant probability (or area). The ROC curve not only evaluates the ability to detect a change at one threshold, but varies over all the possible threshold values as the P_{fa} changes. In this way, if the ROC curve from one method has a higher P_d value, then more of the alternative hypothesis PDF is below the threshold value and the separation between the null and alternative hypothesis PDFs is greater, so the contrast would be better.

The ROC curve does not indicate if a performance level is enough to detect a particular target change signature. First, one would have to have to know the relationship between P_d and P_{fa} for the specific target; as can be seen above, this is a complicated calculation when true coherence values have been assumed to be binary values for change or no change. Second, the coherence values for any mitigation method are dependent upon the total system coherence budget that limits the maximum achievable coherence. A real radar system can change these coherence loss parameters due to many factors thereby limiting the achievable coherence of the system that bounds the coherence estimator's bias and variance [17].

Additionally, the ROC curve cannot quantify the effect of sidelobe level upon detection of any change signatures, but the ROC can quantify the effect of the sidelobe level upon the change and no change case statistics. It should be clear that detecting a change in a CCD image and the statistics represented by the ROC are very different concepts. The detection of change in a CCD image requires a detector to determine if a certain coherence value represents a true change. While for the statistical representation, it is already known that a region of the image contains a change (or does not).

4.3.1 Practical Implementation of Contrast Metric

To implement the contrast metric it is necessary to have the values of true coherence and effective number of looks to construct the PDF for each change and no change case. As it

is uncertain the analytical relationship between the mitigation method upon true coherence and effective number of looks, these values can be estimated from the CCD histogram. The image must be simulated as a model of CWGN over many pixels to obtain a reasonable number of points from which to estimate the histogram and resulting PDF parameter estimates. A single image can be divided into two regions: one of change and another of no change, demonstrated by the resulting CCD in Figure 4.4. Using guard bands to obtain homogeneous statistics, the PDF for each half of the CCD is estimated from the histogram. Then a stochastic search technique can be used to estimate the true coherence and effective number of looks that best fits the estimated PDF. Once those values are known for each change and no change case, numerical evaluation can calculate the ROC curve.

It is important that no interference is present within the CCD used to estimate PDF parameters, because it will affect the histogram statistics. For example, the interference artifacts introduce changes where there should be none, affecting the resulting histogram of the no change case by lowering the coherence separately from the mitigation technique. Essentially the interference itself will have its own PDF with unique parameters, and likely a different distribution than equation (4.4). Remember, the PDF in equation (4.4) is only valid for Gaussian statistics, not the statistics of interference sources.

The restriction of an interference free image/CCD can be overcome by using multiple images during simulation. One image can contain interference, and the calculated mitigation based on that image with interference can be applied to both the image with interference and the image with the change/no change pattern in Figure 4.4. Applying the mitigation to an image without interference is particularly straightforward when the mitigation can be implemented as a weighting vector; this will be demonstrated in following chapters.

It is important to determine how many pixels are required to achieve a stable estimate of the coherence PDF parameters. Once a PDF is estimated by the histogram, the calculation of the PDF parameters are deterministic using numerical methods. It is the image

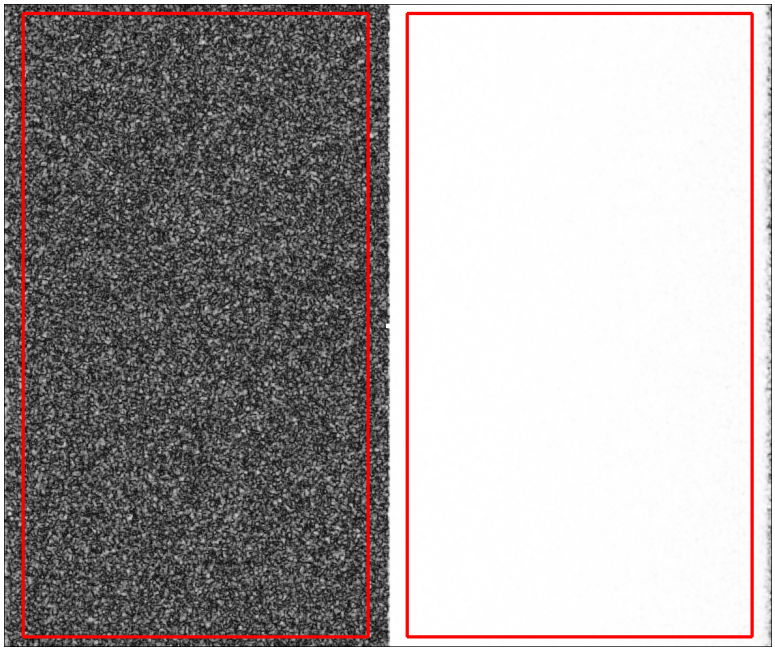

Figure 4.4: CCD image pattern of change and no change regions from which to estimate coherence PDF parameters. Values outside the red rectangles are ignored for the parameter estimation.

size and the number of histogram bins that determine the statistics such that values calculated through PDF parameter estimation are repeatable and stable representations of those statistics. A simulation is created very similar to the simulation in the previous section for determining an acceptable image size to measure average coherence magnitude. Two images were created with CWGN statistics and 10dB SNR, except for half of the image the clutter values were decorrelated as shown in Figure 4.4. Since the previous average coherence magnitude analysis shows an image size greater than 100m by 100m is desirable, this simulation starts with this image size and increases to 300m by 300m. The ROC requires a total of 4 parameter estimates: μ_0, L_0, μ_1, and L_1. Because the coherence estimator is biased and increases variance as the true coherence value decreases, the alternative hypothesis parameters (i.e. change case, μ_1 and L_1) are not evaluated for repeatability. Figure 4.5 shows the results of varying the scene size upon the estimates of the no change case (i.e. null hypothesis) true coherence and effective number of looks for different values of the local averaging window and number of histogram bins. The results are shown in terms of

parameter value deviation from the mean to three standard deviations. Since each value is computed from CWGN regenerated for each trial, each measurement is independent and Gaussian statistics are assumed; therefore these plots show by how much 99.7% of the parameters estimates deviate from the mean value. It turns out that the number of histogram bins, which defines the number of points of the coherence PDF, has little impact upon the value of the parameter estimates. The mean value of the effective number of looks increases with the size of the local averaging window, therefore its deviation value also increases. In summary, the simulations represented in Figure 4.5 indicate despite changing the size of the local averaging window or the number of histogram bins, there is no significant stabilization in values for either the coherence or effective number of looks. If the same criteria used for average magnitude coherence is applied to selecting image size, then the image should be at least 125m by 125m.

The choice for the size of the local averaging window is a trade-off between the desire to resolve change details in the CCD product and reducing bias and variance in the coherence estimator. A larger averaging window results in lower bias and reduced variance for the MLE coherence estimator [17]. While Figure 4.6 shows increasing the local averaging window blurs the disturbance pattern. Three choices have be selected for comparsion, 25, 49, and 81. Odd values are chosen so that the local average window is square and centered upon a pixel, though this is not a requirement.

Given that in this dissertation the relative performance between methods is being measured, the absolute accuracy of the coherence estimate is not required, so long as a stable measurement is made. Since the purpose of the images in Figure 4.6 are qualitative evaluation, the choice is made to use a local averaging window of 5x5 so the CCD disturbance patterns appear sharper.

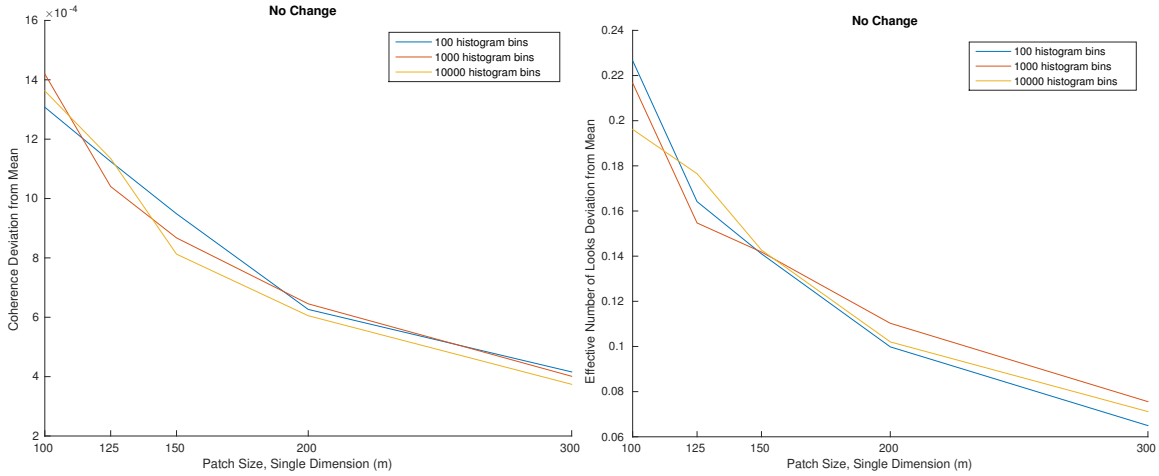

(a) No change coherence (μ_0), N = 25

(b) No change effective number of looks (L_0), N = 25

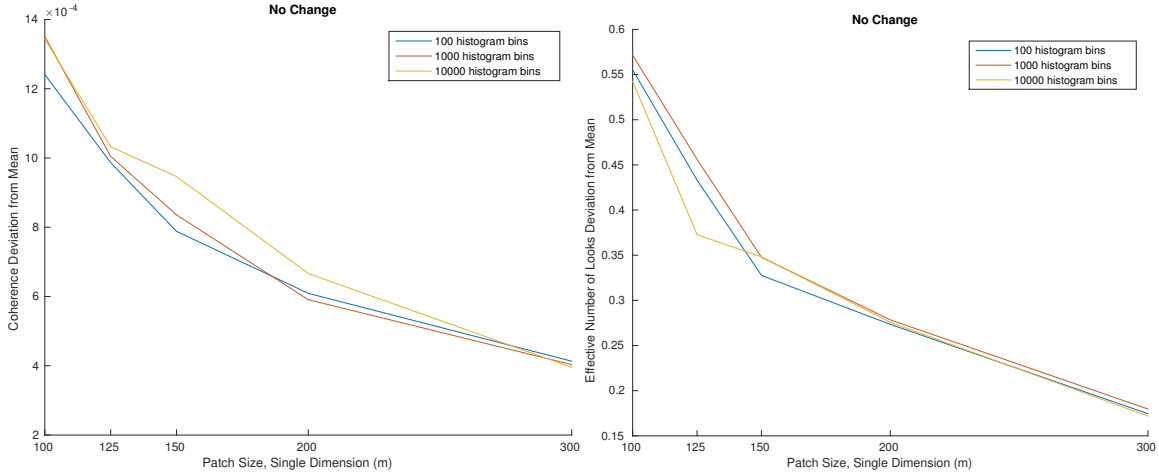

(c) No change coherence (μ_0), N = 49

(d) No change effective number of looks (L_0), N = 49

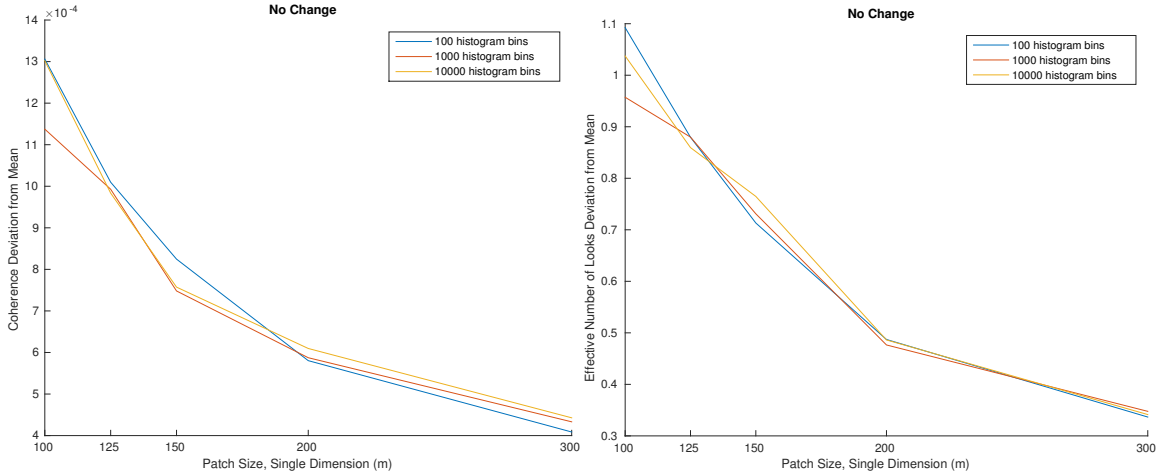

(e) No change coherence (μ_0), N = 81

(f) No change effective number of looks (L_0), N = 81

Figure 4.5: Simulations showing the parameter value deviation at 3σ for estimating coherence PDF parameters as a function of scene size while varying local averaging window size and the number of histogram bins.

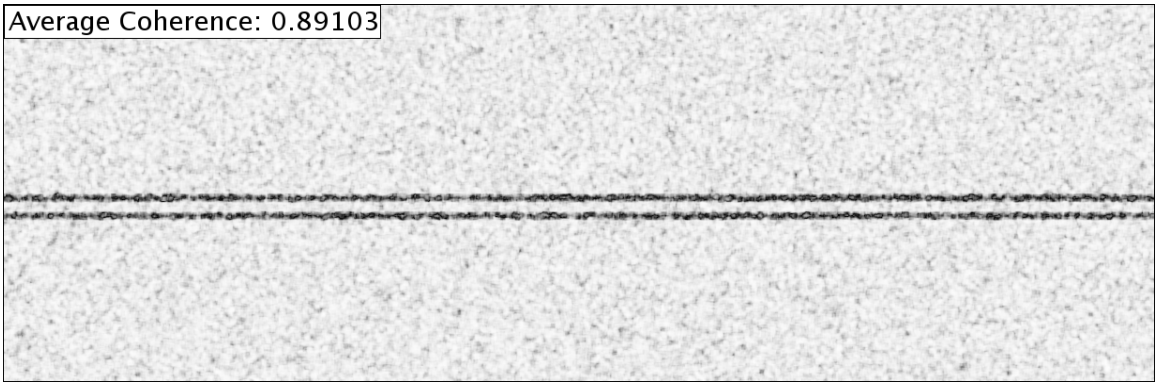

(a) Local averaging window: 5x5

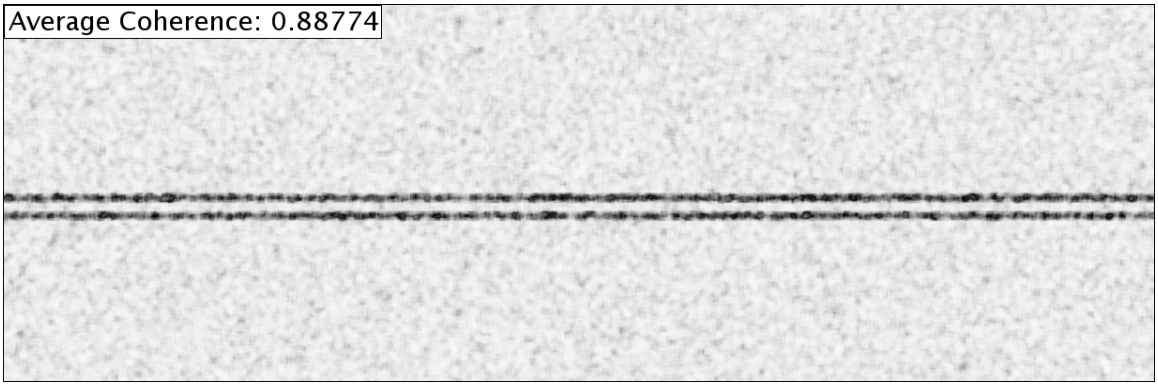

(b) Local averaging window: 7x7

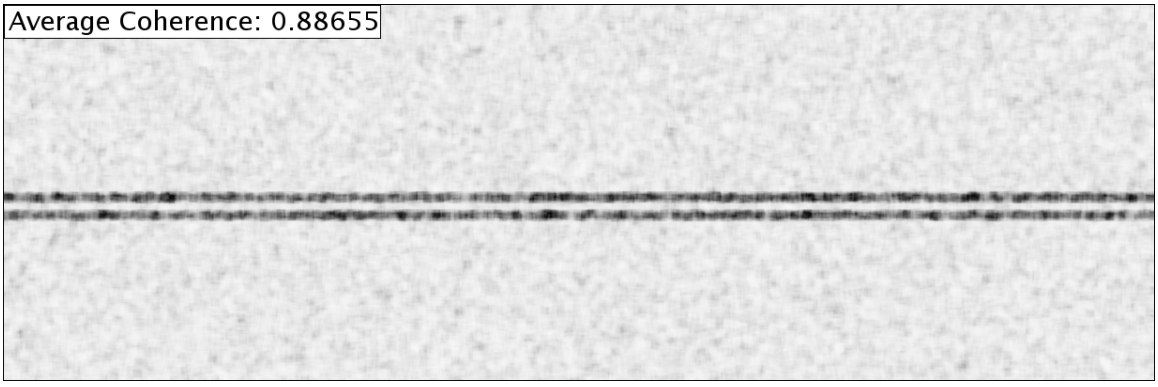

(c) Local averaging window: 9x9

Figure 4.6: Comparison of a disturbance pattern as the size of the local averaging window is increased from 5x5 to 9x9 local pixels.

4.4 Summary

In this chapter three classes of metrics have been introduced to evaluate the impact of different interference mitigation techniques upon image quality, average coherence, and contrast for change detection. It has been shown how each of these methods can and cannot evaluate the effects from various mitigation techniques. The prime concern of this dissertation is evaluation of the performance difference between one mitigation technique against another mitigation technique.

Based upon the results in Figure 4.2, Figure 4.5, and Figure 4.6 a simulation will yield stable measures of average coherence and PDF parameter estimates for an image size of 100m by 120m, 100 histogram bins, and a local averaging window size of 5x5. A non-square image size is chosen to help aide in debugging throughout image and signal processing.

It should be noted that any application to a real radar system depends upon the specific interference source upon a specific radar system and its mission. Ultimately, it is up to the radar system engineer to determine if an interference mitigation meets specifications. Some of the factors affecting the radar system engineer's decision have been summarized into the metrics described in this chapter, but these by no means should be the only factors in selecting an interference mitigation technique.

CHAPTER 5

A NEW APPROACH TO POWER EQUALIZATION

The concept of power equalization of phase history data is used by [40,52,53] to remove the effects of interference from SAR images. Each of these methods differ in implementation and the resulting effects are unique to each algorithm. A novel approach is presented that is better suited for deramp SAR applications.

The reason phase history equalization is desirable can be attributed to the ideal response for the radar system. The deramp radar, in essence, samples a tone in time that represents an echo of the transmitted radar pulse from a single scatterer. Many of these tones are combined according to the principle of superposition to create a SAR image. Considering the case of a single scatterer, from deramp processing the frequency of the tone sampled in time determines the single scatterer's relative position to the radar. Typically a Fourier transform can be used to measure the frequency value of the tone to resolve the range of the single scatterer. Because this tone is only sampled for a finite period of time, the Fourier transform operates upon a time-limited sinusoid and the result is a sinc function. This is also called the impulse response (IPR) of the radar system. A sinc function by definition has -13dB sidelobe level and for SAR images it is generally accepted that suppressing these -13dB sidelobes results in a more aesthetically pleasing image [10]. To reduce sidelobe level, typically SAR processors use a window function to shape the amplitude of the sampled signal before the Fourier transform is applied. The amplitude envelope of the single scatterer tone directly affects the IPR shape. When interference appears in the phase history, it distorts the amplitude envelope of the phase history, so the natural tendency would be to flatten the amplitude envelope to return the phase history data to the ideal case.

The interference actually combines with the single scatterer tone by superposition so the Fourier transform can be considered as operating on each signal separately so there is no change in the single scatterer IPR, however the artifacts from the resulting Fourier transform upon the interference signal add to the IPR. The power of the interference signal relative to the scatterer signal combined with the signal processing and radar hardware specifications determine the point at which the interference effects are no longer benign within the image. The power equalization technique seeks to equalize the power of the interference signal to that of the radar signal such the interference effects are minimized, however the interference energy is never completely removed. When the interference is band-limited and narrower than the radar bandwidth, the integration gain of the Fourier transform upon the interference signal is greatly reduced from the integration gain upon the scatterer signal. Thus when the interference energy is of similar amplitude to the phase history and narrow in bandwidth relative to the phase history, after the Fourier transform the amplitude of the image artifacts are greatly reduced.

The following section describes a novel equalization algorithm used to estimate the interference energy level and equalize the phase history amplitude. Then a series of simulations shows how the algorithm is applied to phase history data and two test cases to evaluate its performance against the standard notch.

5.1 Algorithm

The primary issue for power equalization is determining the true radar signal energy level to equalize the interference data values. The algorithm can avoid estimating the true radar signal energy by creating an envelope of the phase history magnitude, including interference, to then equalize the entire phase history. Because the envelope is computed by low-pass filtering with a median filter, the choice of the median filter parameters are paramount to its performance.

The calculation of an envelope for each phase history pulse is unique from [52] where

a single average value for each range-compressed pulse is used to normalize the data. Since deramp interference spreads across all the range-compressed pixels, Zhu et al.'s [52] method adjusts not only the interference artifacts but the clutter/terrain values, too. The normalization process in [52] does not change the signal to interference power ratio unlike the median filtered envelope.

The median filtered envelope is more flexible than the approach used by Lamont-Smith [40] where an internal/loopback calibration path provides a reference signal for equalization. The Lamont-Smith [40] equalization averages together several pulses of data so any interference sources that are stationary from pulse to pulse will be represented in the envelope while the variance of the radar signal smooths the envelope. However, if the interference changes rapidly from pulse to pulse, even if frequency stable, the amplitude over several pulses can be reduced. In contrast, the median filtered envelope is able to adjust independently to the characteristics of the interference as it changes, if necessary, for each pulse. But it also has the flexibility to be applied over any number of local pulses or pulses throughout the aperture.

Following the block diagram in Figure 5.1, the algorithm begins with a single pulse of phase history data after deramp processing and sampling in the form

$$A_{si} = |A_s| e^{j\theta_s} + |A_i| e^{j\theta_i}, \tag{5.1}$$

where A_s is a complex signal describing the reflected radar energy from the scene, A_i is a complex signal describing the interference energy received by the radar, and A_{si} is the combination of both signals that make up the phase history data for a single pulse. The magnitude of the data, $|A_{si}|$, is low-pass filtered to create an envelope (or smoothed version) of itself, $|\tilde{A}_{si}|$. Then to normalize the power level, the mean of the envelope, $\mu_{|\tilde{A}_{si}|}$, is divided out to yield

$$|\tilde{A}_{sio}| = \frac{|\tilde{A}_{si}|}{\mu_{|\tilde{A}_{si}|}}, \tag{5.2}$$

which is inverted to produce a weighting vector,

$$w_{pe} = \frac{1}{|\tilde{A}_{sio}|}, \tag{5.3}$$

that can be applied to the original data to get the power equalized data,

$$A_{pe} = A_{si} w_{pe}. \tag{5.4}$$

The inversion of the low-pass filtered envelope, $|\tilde{A}_{sio}|$, makes it convenient to apply the correction envelope as a multiplication instead of a point-by-point division.

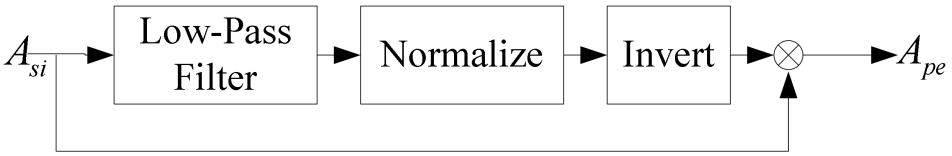

Figure 5.1: Block diagram of power equalization implementation.

Another equalization method by Fan et al. [53] uses median filtering, however its application is different. Fan et al. [53] applies a detector to select only the samples containing interference to be median filtered with adjacent data samples. The median filter width is twice that of the band containing interference so assuming there are no adjacent bands of interference energy, the magnitude value of the resulting median filtered samples will be at most half of the original the interference energy. Also, the variance of the phase history data determines the RCS value. Smoothing a section of the data will alter the variance characteristics of the data. An extreme example is if a section of the phase history is flattened completely; that produces a false point target at the scene center. The 'resolution' of the point target depends upon the width of the flattened phase history data. And the resulting image IPR is distorted (in a similar method as observed earlier after applying the standard notch) because the zero variance within the flattened phase history affects all components of the image.

The low-pass filter minimizes the phase history variance. Ideally, the correction en-

velope should be as smooth as possible. Any reductions in the median filter size that try to account for sharp variations in amplitude from interference trade-off any interference suppression gains against reducing the phase history variance.

5.1.1 Calibration Effects

Although the amplitude of the phase history is equalized such that the bandlimited interference is the same power level as the rest of the phase history, the total power in the phase history, including the interference is preserved, so that the clutter RCS values in the image have actually increased due to the interference energy. This happens because the envelope is normalized by $\mu_{|\tilde{A}_{si}|}$, which is the average value of the reflected radar energy plus the interference energy. The interference energy is preserved by amplifying the entire phase history.

In practice it is difficult to separate the interference signal from the radar signal (otherwise mitigation would be a simple coherent subtraction), but if the proper energy level, $\mu_{|A_s|}$ was known through some means, replacing its value into equation (5.2) would still not return the correct clutter RCS. A portion of the signal has been reduced in magnitude by the interference via the correction envelope, so a correction factor is necessary to account for that magnitude reduction. Ideally the total power in the phase history would be comprised of the original signal power plus the reduced magnitude interference power.

One possible work-around if the image contains a point target and mild to moderate interference is to measure the RCS of the point target before mitigation. From Figures 2.11a and 2.11b it is known that the RCS of a point target is relatively stable if interference energy is significantly below the peak value. The RCS of the point target can be adjusted after equalization to return its peak value to its original value before equalization.

5.2 Simulations

Below, simulations are made to compare the performance of the equalization technique against the standard notch technique. Fundamentally the detector for each method is different. The equalization combines the detection of interference into the calculation of the equalization envelope by the median filter. If the interference is of shorter duration than the median filter, then the median filter results in an envelope value that is less than the interference, thus it is not completely suppressed by the equalization. In contrast the standard notch is compatible with a multitude of detector implementations, but requires a binary decision whether a sample contains interference or not. That binary decision is not possible within the described equalization algorithm.

It is critical the mitigation methods have the same detector. Interference sources can vary greatly in structure and each detector will vary in the data samples identified to contain interference. Every detector has a certain amount of interference energy leakage; this leakage will impact coherence measurements and may skew the results for or against a mitigation technique when it is really the detector influencing the results.

The way to compare the equalization method to the standard notch is to use a rect function as an ideal envelope for the interference. The width of the rect function will determine the performance of the standard notch, while the performance of the equalization will vary with the height of the rect function that represents the SIR.

5.2.1 1D Simulation

To illustrate how the equalization technique works, a 1D simulation is created conforming to the parameters below in Table 5.1. The technique begins with fast-time data samples from a single pulse, shown in Figure 5.2a, that contains the radar return signal and an interference signal. The interference signal is band-limited Gaussian noise adjusted to a SIR of -5dB where its additional energy is obvious in Figure 5.2a as the large increase in signal

amplitude between fast-time sample numbers 400 and 550. For this simulation, instead of using a low-pass filter, an idealized envelope is created from the known band-limited parameters of the interference signal. The normalized and inverted weighting vector is shown in Figure 5.2b. Once the weighting is applied to the fast-time samples, Figure 5.2c verifies the resulting data values are relatively constant and any interference energy is seemingly removed.

Typically, flattening the phase history improves IPR, in a similar way window functions shape the mainlobe/sidelobe structure. The constant amplitude, constant frequency tone from a single scatterer yields an ideal sinc function after the Fourier transform is applied during image processing. However, the addition of interference energy to the data, despite flattening the magnitude of the combination of the radar signal and the interference, actually shapes the envelope of the radar return signal. Because this is a simulation, it is straightforward to apply the equalization weighting to the original phase history data without the interference signal. Figure 5.2d verifies the phase history of the radar signal is in fact not equalized. The radar signal may not be equalized but the attenuated signal improves the IPR response and reduces distortion compared to the standard notch. Also, the interference image artifacts are greatly reduced in value, reducing their appearance in the image and reducing their SINR loss contribution to coherence.

Center Frequency	16.8GHz
Resolution	0.1524m (6”)
Scene Size	100m
Image Oversample Factor	1.5
Window Function	Taylor $\bar{n} = 4$ -35dB SLL
Point Target RCS	25.5dB
Clutter RCS	-28dB
Noise RCS	-38dB

Table 5.1: 1D equalization simulation parameters

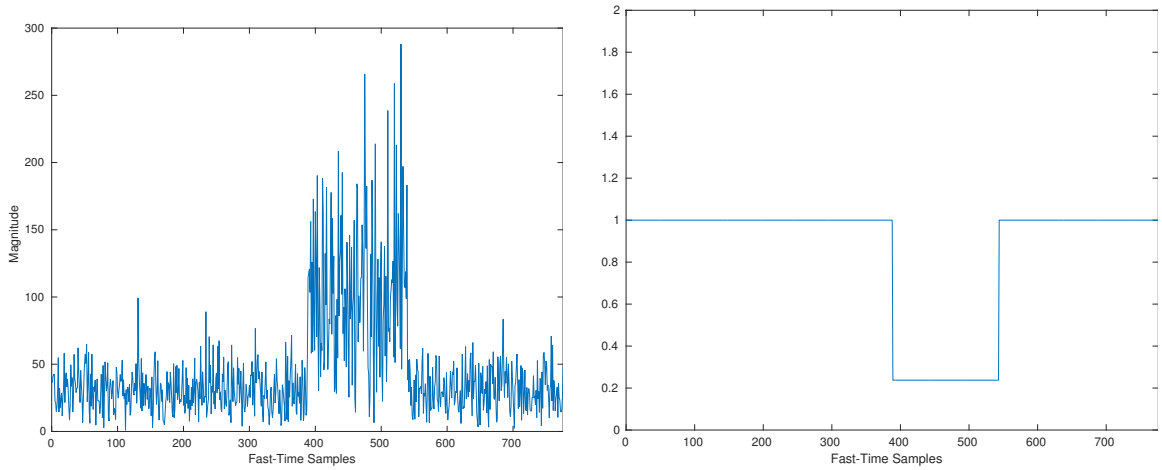

(a) Original data with interference

(b) Correction weighting

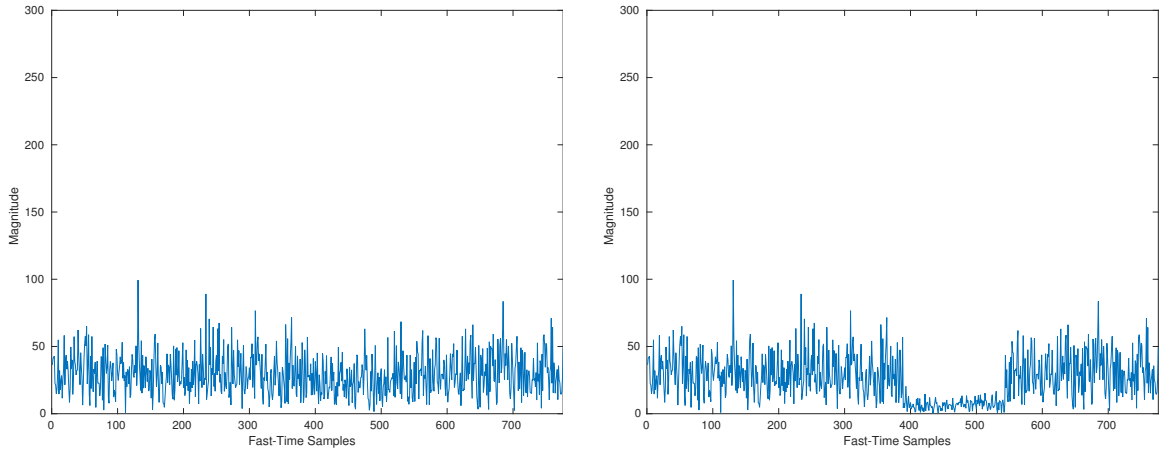

(c) Envelope applied to data

(d) Envelope applied to radar signal only

Figure 5.2: Fast-time phase history data for simulation parameters in Table 5.1 to illustrate how the equalization mitigation works for a simulated interference power of -5dB SIR.

5.2.2 Relation to Standard Notch

There is a limit to the effectiveness of equalization in that as the interference magnitude increases, the signal within the interference will be further suppressed, approaching a condition close to notch filtering. IPR metrics can be used to examine when equalization becomes equivalent to the standard notch. It should be noted that by evaluating IPR, the effects of the residual interference energy due to the detector differences are ignored. The mitigation methods differ in that the standard notch is capable of completely suppressing the interference energy only if it is detected, while the equalization method makes no binary decision when equalizing data and residual interference energy is always present. This becomes important later for comparing average coherence where the residual interference energy from equalization for a low SIR case contributes a coherence loss by lowering the SINR.

Figure 5.3a shows a plot of ISLR as a function of SIR for the simulation parameters in Table 5.1. The interference occupies 20% of the fast-time samples and is centered at 3/5 of the length of the fast-time samples, as shown in Figure 5.2a. As expected the ISLR of the standard notch is constant because changing the SIR does not change the mitigated data. The ILSR of the equalization mitigation increases (i.e. gets worse) as a function of SIR, until it approaches the standard notch. For visual verification, the IPR of the standard notch is plotted in Figure 5.3b. The equalization IPR at 5dB SIR in Figure 5.3c shows a moderately increased sidelobe level at a distance of 10 pixels with a large increase in sidelobe energy very close to the mainlobe. At a -25dB SIR, Figure 5.3d shows the equalization IPR is a match for the standard notch IPR with nearly identical shape, 3dB width, ISLR, and PSLL.

Therefore, based on the IPR characteristics, as SIR decreases the equalization method image distortion approaches that of the standard notch.

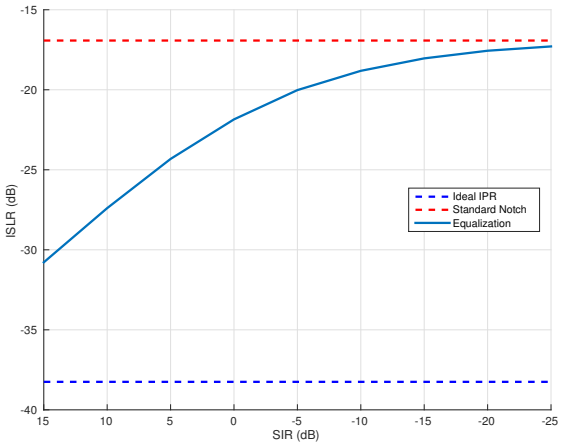

(a) ISLR as function of SIR

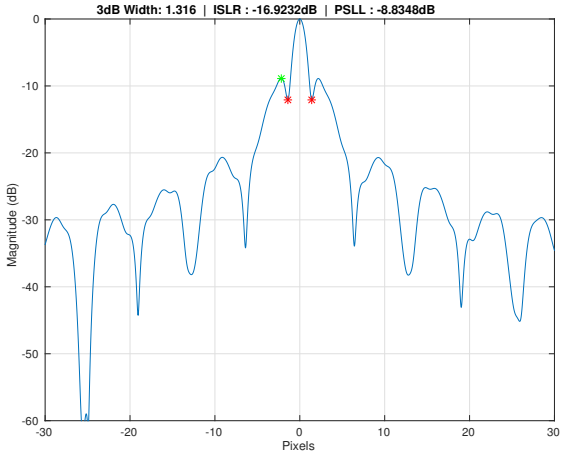

(b) Standard notch IPR

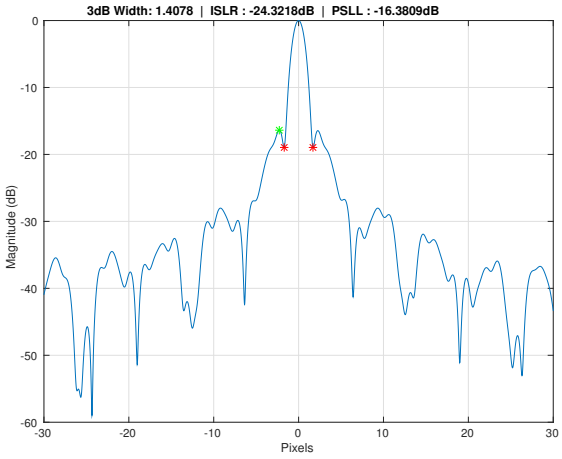

(c) Equalization IPR at 5dB SIR

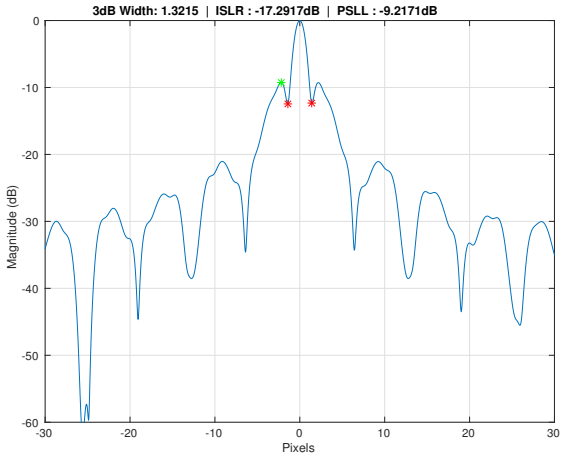

(d) Equalization IPR at -25dB SIR

Figure 5.3: Simulation showing the IPR distortion due to equalization mitigation increases as SIR decreases.

5.2.3 2D Simulation

A simulation is made with images of simulated point targets and terrain to evaluate the average coherence magnitude differences between equalization and the standard notch. Unlike the IPR analysis above, these simulations will include the effects of residual interference energy from equalization. This residual interference energy is the difference between Figure 5.2c and Figure 5.2d. The residual interference source is a CWGN noise windowed by a rect function in the spatial-frequency domain to represent band-limited interference. The variance of the CWGN is modified to achieve the desired SIR. A rect function repre-

sents the ideal correction envelope to calculate the equalization weighting and the output of an ideal detector for the standard notch. All parameters from Table 5.1 are used with the addition of an azimuth patch dimension of 120m. The interference is centered within the fast-time sample data for two different widths of 5% and 25% of the number of fast-time data samples. Both simulation cases vary the SIR level to change the performance of the equalization mitigation.

Figures 5.4a and 5.5a show the average coherence as a function of SIR for a notch width of 5% and 25%, respectively. In both cases at high SIR the equalization method is better than applying no mitigation or the standard notch, but as the interference energy increases (i.e. SIR decreases), the average coherence of the equalization becomes worse than the standard notch. There are two reasons for this behavior. The first is that as was observed in Figure 5.3a, as SIR decreases the IPR distortion approaches that of the standard notch, which decreases the average coherence to the level of the standard notch. The second reason is the residual interference energy, the difference between Figure 5.2c and Figure 5.2d, contributes to the noise power and reduces the average coherence by equation (3.1). If it were not for the residual energy the equalization performance would approach that of the standard notch, as demonstrated in the 1D simulation.

Although the limit of the equalization performance is worse than the standard notch, there is a clear region at high SIR values where the equalization mitigation yields a coherence improvement. To illustrate these regions two SIR values of 10dB and -15dB were chosen to create qualitative images with a disturbance pattern for each simulation case in Figure 5.4 and SIR values of 5dB and -15dB for Figure 5.5. The disturbance pattern approximates tire tracks and is placed in a horizontal direction to exacerbate any possibility of elevated range sidelobes from the mitigation affecting the disturbance.

The SIR region where the equalization mitigation improves over the standard notch increases with the size of the notch, up to 50% of the fast-time data samples. Beyond 50% the interference signal dominates the phase history signal and the equalization has

less effect upon the signal-to-interference ratio as the interference signal approaches 100% of the fast-time data samples. It should be straightforward to consider when interference occupies 100% of fast-time data samples that any weighting modification to the phase history cannot change the signal-to-interference power ratio.

5.3 Summary

In this chapter it has been shown that a novel method for equalizing the fast-time data samples for a deramp SAR can improve coherence in cases where the signal-to-interference ratio is high. However, it was also shown that residual interference energy from high levels of interference energy can contribute to a coherence loss that is worse than the standard notch. Another factor to consider is the interference detector for the equalization is different from the detector used for the standard notch in that it does not require a binary decision if interference is present or not. This is a weakness in the standard notch (or any mitigation) in that if the detector cannot detect the interference energy, or detects it incorrectly, then residual interference energy can be present. It is important to note that the cases presented here represent an ideal detector whereas the performance for a real detector upon a real interference source can vary.

The primary advantage of the equalization mitigation over the standard notch is when interference energy is low and narrowband, where the standard notch mitigation can be worse than doing no mitigation. But as the interference energy increases, equalization and standard notch are not sufficient so additional mitigation methods are explored in the following chapters.

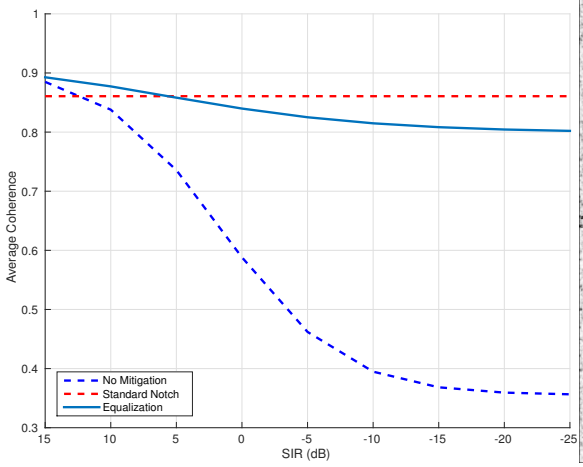

(a) Average coherence

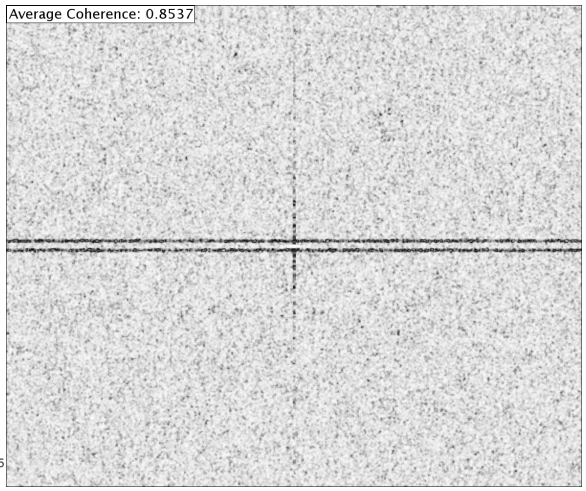

(b) Standard notch CCD

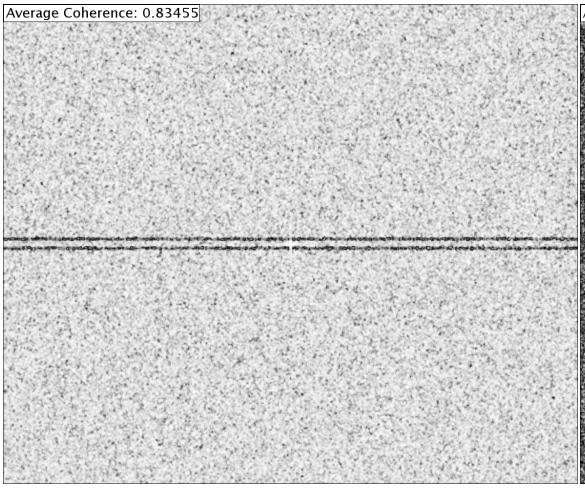

(c) No mitigation CCD 10dB SIR

(d) No mitigation CCD -15dB SIR

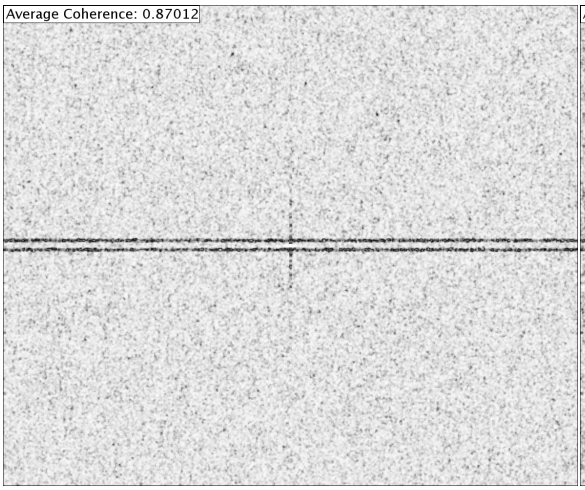

(e) Equalization CCD 10dB SIR

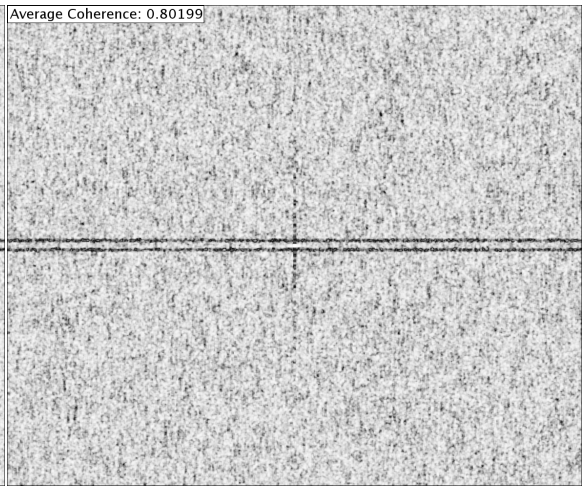

(f) Equalization CCD -15dB SIR

Figure 5.4: 2D simulation comparing average coherence magnitude between equalization and standard notch for a notch width of 5% the fast-time data samples located at the center of fast-time samples.

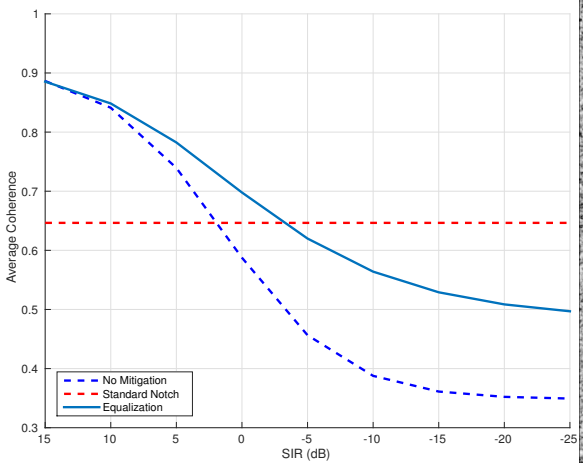

(a) Average coherence

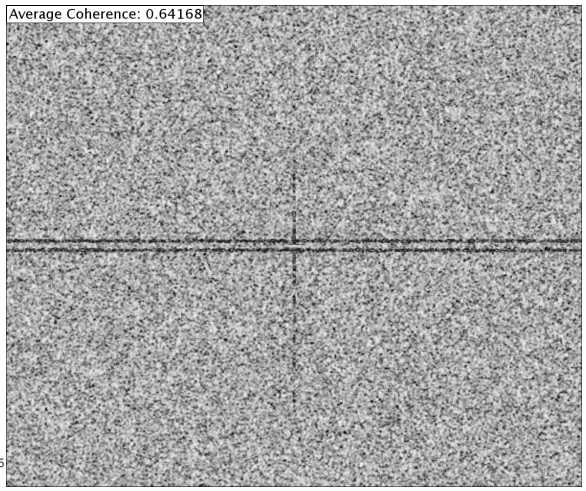

(b) Standard notch CCD

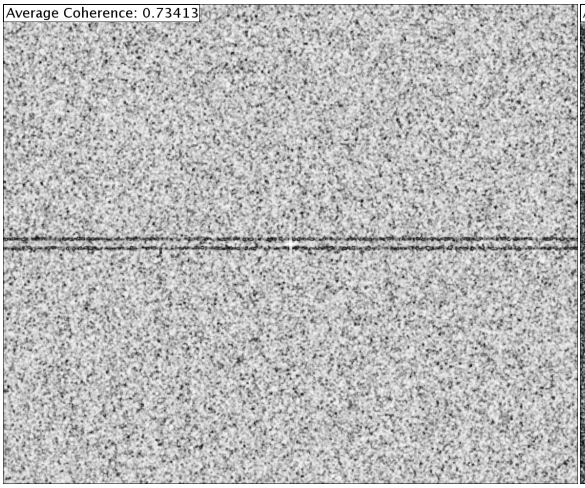

(c) No mitigation CCD 5dB SIR

(d) No mitigation CCD -15dB SIR

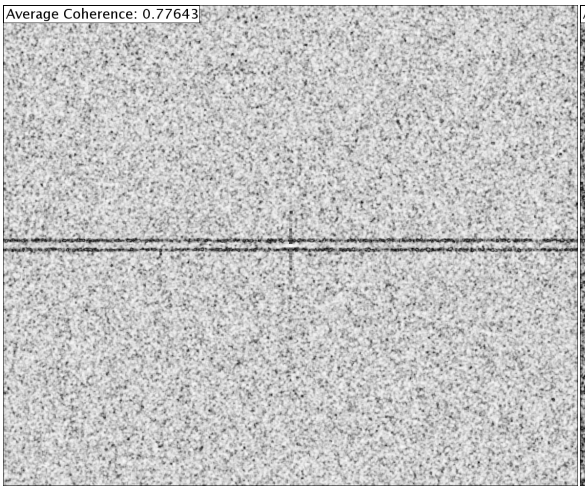

(e) Equalization CCD 5dB SIR

(f) Equalization CCD -15dB SIR

Figure 5.5: 2D simulation comparing average coherence magnitude between equalization and standard notch for a notch width of 25% the fast-time data samples located at the center of fast-time samples.

CHAPTER 6

SINGLE APERTURE INTERFERENCE MITIGATION

As demonstrated in chapter 3, the standard notch mitigation can be a simple and effective method to mitigate interference. It is simple in that data samples are forced to zero value where interference is detected. It is effective in that no residual energy remains from the detected interference. The problem for the standard notch is that as the number of samples notched increases, the image distortion increases and the resolution decreases. It has been shown that both of these effects lower the average coherence of second order SAR image products. This chapter examines interference mitigation techniques that are applied to one image of the coherent pair to improve the average coherence.

Two new interference mitigation algorithms are proposed called spectral notch and split window notch. First, each algorithm is described in detail. Next a simulation quantifies image quality, coherence, and contrast performance for an ideal detector under many conditions. Finally, real data examples validate the simulation results to demonstrate the mitigation method with the most coherence improvement.

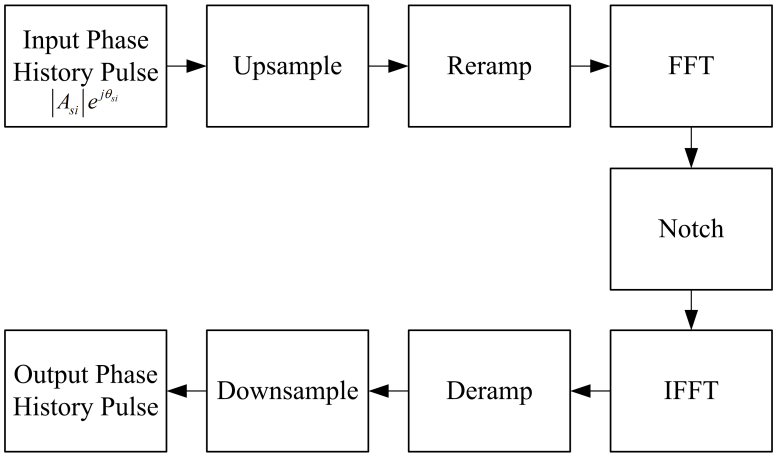

Figure 6.1: Spectral notch block diagram.

6.1 Spectral Notch

Earlier it was explained that typical spectral notching techniques are ineffective for deramp SAR because interference occupies less data samples in the phase history than the radar signal. This fact arises in part from assuming the interference is narrowband relative to the radar's RF bandwidth. To work around the limitations of the deramped data, it is possible to compute the spectrum of the deramp phase history by applying digital signal processing to reramp the phase history data.

The reramping process begins for each pulse of phase history data by upsampling to the RF bandwidth. Then the data is multiplied by a chirp signal with the same chirp rate used to collect the data. Now a Fourier transform resolves the spectrum of the data and any spectral domain filter of choice may be applied. After notching or filtering the RF spectrum it can be inverse-Fourier transformed, deramped, and downsampled back into phase history data. A block diagram of the processing steps is shown in Figure 6.1.

As an example, a deramped phase history of a constant tone interference source is shown in Figure 6.2a and its corresponding spectrum via the Fourier transform is shown in Figure 6.2b. The interference is clearly visible in Figure 6.2a as the increased magnitude from approximately sample number 300 to 500, and contributes evenly across the IF spec-

trum in Figure 6.2b elevating the average magnitude. Upsampling and reramping the data produces Figure 6.2c; this signal is not equivalent to what would have been recorded by the radar if the radar had not used stretch processing and sampled at the RF bandwidth. The interference signal is limited to a portion of the upsampled and reramped signal because the deramp processing has truncated it in time. Upsampling doesn't change the span of time the interference signal is present, it still follows equation (2.19). Multiplying a chirp to the signal only removes the chirp placed on the existing, time limited interference signal by the deramp processing.

Now that the interference signal is returned to its original form, Figure 6.2d shows the Fourier transform resolves its true frequency components, although slightly broadened due to the finite support of the interference signal in the reramped phase history. Since the interference source in this particular example is a constant frequency tone at the radar's center frequency, a spike at the center of the RF bandwidth is shown in Figure 6.2d. Within the RF spectral domain any responses from scatterers within the scene occupy the full radar bandwidth. Therefore any RF sources from transmitters external to the radar system that are less than the RF bandwidth of the radar will appear only within a portion of the RF spectral domain.

At this point any method [21, 42, 43] for spectral domain notching can be applied. If the interference is notched from the RF spectrum, deramped, and downsampled the result is shown in Figure 6.2e. The IF spectrum of the notched data shown in Figure 6.2f is significantly lower magnitude than the interference containing IF spectrum in Figure 6.2b.

6.1.1 Comparison to Standard Notch

The spectral notch may appear to be comparable to the standard notch with deskew correction. For a single tone or narrowband signal the deskew correction removes the residual chirp signal in the phase history domain thus reducing the number of samples that the interference energy occupies. After the deskew correction, the time sample location of

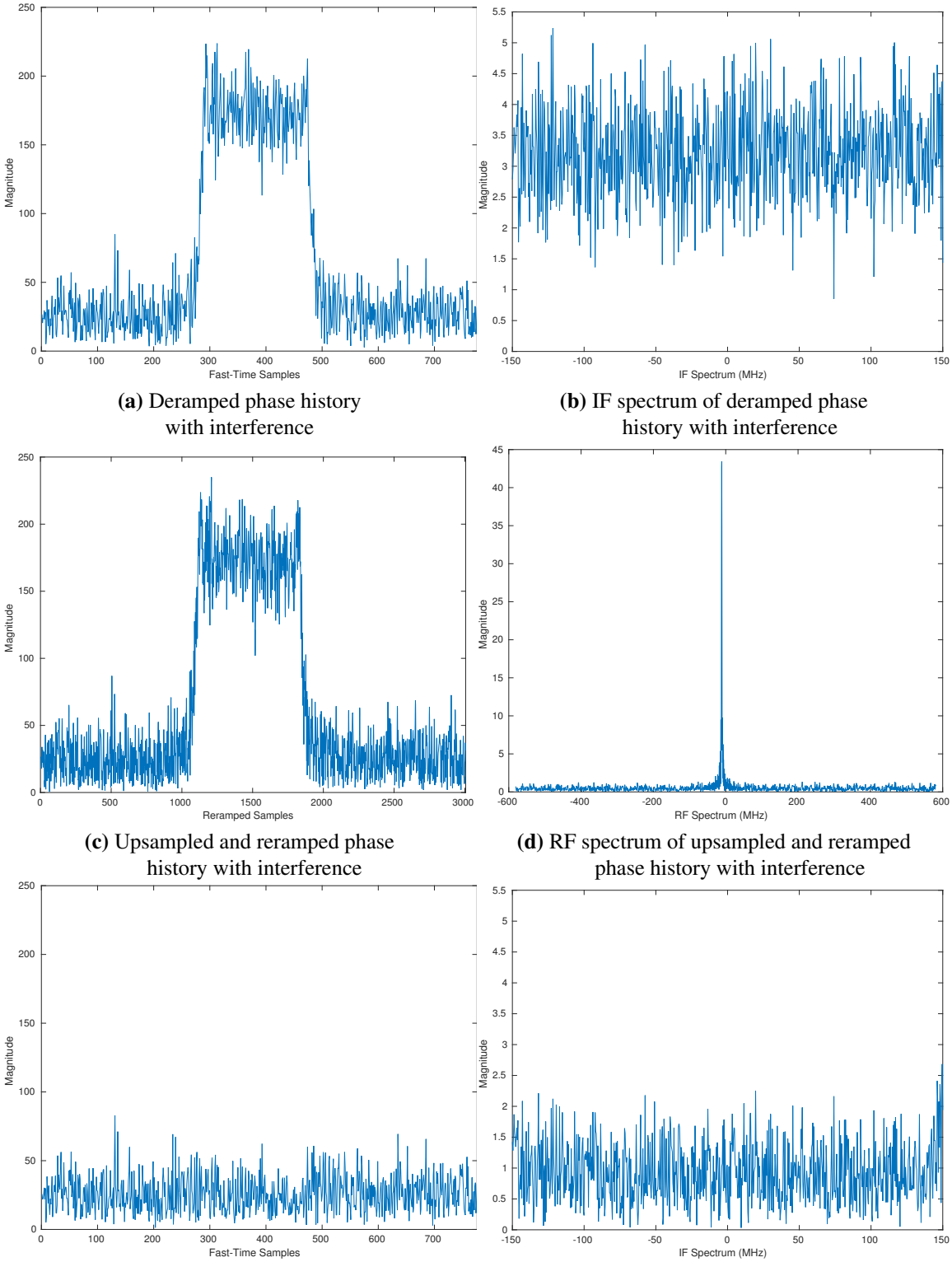

(a) Deramped phase history with interference

(b) IF spectrum of deramped phase history with interference

(c) Upsampled and reramped phase history with interference

(d) RF spectrum of upsampled and reramped phase history with interference

(e) Deramped and downsampled phase history after notching RF spectrum

(f) IF spectrum of deramped and downsampled phase history after notching RF spectrum

Figure 6.2: Example of spectral notch processing.

the interference signal is determined by equation (2.18) that relates the frequency difference between the tone and the radar center frequency to time by the radar's chirp rate. So in a sense, the phase history itself is a representation of the RF spectrum through this mapping. One may consider notching a certain percentage of samples in the phase history domain as equivalent to notching the same percentage of samples from the RF spectrum.

After deskew processing a single tone interference source may appear as a spike in the phase history, but its Fourier transform still spreads across the entire RF bandwidth because it is now very limited in duration and approximates a delta function. Any notches in the phase history introduces magnitude and phase discontinuities into the sinusoids representing the scatterers. Since the sinusoids from all of the scatterers in the scene exist throughout the entire phase history, a notch in the phase history disturbs every scatterer in the scene.

By notching the RF spectrum, only the frequencies of the interference are removed from the data. Every scatterer in the scene is represented by all frequencies across the RF bandwidth, so not all the frequencies that makeup the scatterer's response are disturbed. Once those frequencies are notched or filtered in the RF spectrum, the matched filter is applied via the deramp process such that the resulting sinusoids in the phase history do not have the same magnitude and phase discontinuities as the phase history notch.

6.2 Split Window Notch

Typically SAR image processing applies a window function to reduce the sidelobe levels of bright objects to create a more aesthetically pleasing image [10]. However, once the data has been notched typical window functions no longer create desirable sidelobe levels and the result is what has been classified in this dissertation as IPR distortions. It is the discontinuity in the phase history that causes the increased sidelobe level. In fact, it has been shown that under the constraint of maintaining a narrow mainlobe and large peak-to-sidelobe ratios that the IPR cannot be repaired by shaping any window over the entire aperture [54]. An example of the typical window function, modified by the standard notch

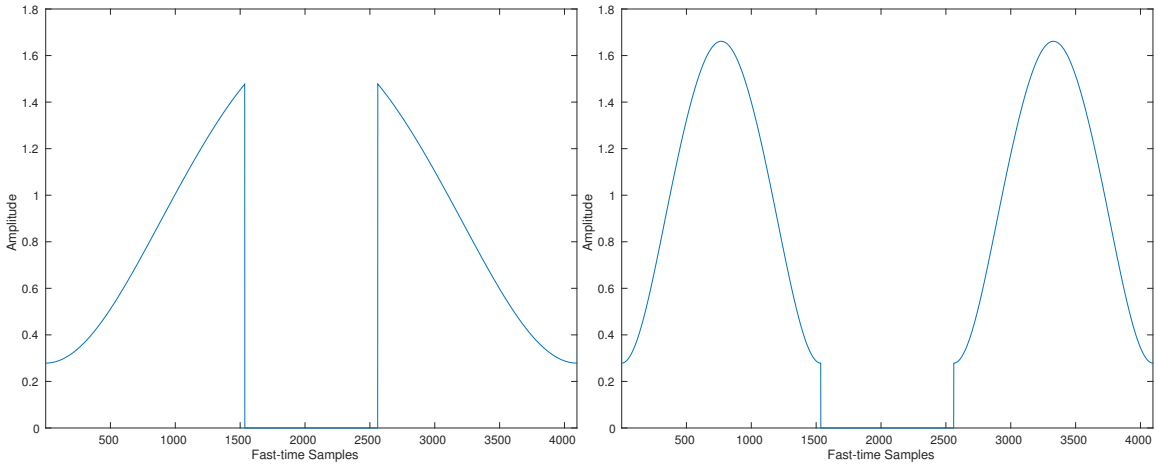

(a) Typical window applied after standard notch **(b)** Split window applied after standard notch

Figure 6.3: Comparison between (a) typical image processing window function and standard notch and (b) splitting the window function by the notch.

can be observed in Figure 6.3a where the discontinuity is clear. The split window notch seeks to reduce the sidelobe levels caused by the discontinuity in the phase history from notching regardless of mainlobe characteristics.

Practically, this approach requires a particular detector that can identify the interference into a contiguous region. A window function is calculated for each remaining region that is detected to not contain interference, while the regions containing interference are zeroed to eliminate any interference artifacts from the final image. To illustrate the difference, Figure 6.3 shows an example of a notched phase history that is windowed by a typical window and an example of the split window applied to the same notched phase history.

Smoothing discontinuities in the phase history data is not a novel concept. A seemingly related mitigation algorithm tunes an FIR filter to the interference frequency [25, 43]. The split window mitigation is unique in that no adaptive algorithm is used to modify the interference amplitude because notching the data values to zero eliminates all interference energy. Both techniques could rely upon the same detector mechanism, but the adaptive algorithms require an optimization constraint that is not required for the split window notch. Furthermore, the split window algorithm is implemented in the fast-time phase history domain, not upon the true data frequency spectrum as in [25, 43] which requires

more processing.

6.2.1 IPR Comparison

A pair of a point target IPRs are shown in Figure 6.4 for when 20% of data samples are notched from the center of the fast-time data and then a -35dB, $\bar{n} = 4$ Taylor window is applied across the apertures as indicated in Figure 6.3. The IPR in Figure 6.4a uses a window applied across the entire aperture and yields an ISLR of -16.2dB, which is substantially higher than the ideal IPR ISLR of -36.1dB (from Figure 2.6). However, notice the 3dB width of the IPR in Figure 6.4a is much narrower than it should be, particularly when considering the resolution loss from notching spectrum should have increased the 3dB width. The red dots in Figure 6.4 identify the nulls where the mainlobe is defined from the sidelobe from which to calculate the ISLR. Since the mainlobe is not accurate, then the location of the first nulls may also be incorrect, therefore due to the IPR distortion the ISLR calculation is not able to accurately discriminate between the true mainlobe and sidelobes to calculate an accurate energy ratio between the two. Consequently, it is difficult to use ISLR in this case to quantify the IPR distortion.

What is of particular importance for the distorted IPR is the level of the sidelobes far away (> 10 pixels) from the center. The IPR in Figure 6.4b at more than 10 pixels away has sidelobes that are more than 15dB below that of Figure 6.4a. The lower sidelobes mean less instances of false decorrelations because the number of neighboring pixels affected by the poor IPR is reduced. Later it will be shown that the fact that the sidelobe level is lower means the split windowed notch yields improved image products.

6.3 Performance Comparison by Simulation

With the introduction of two unique mitigation methods, simulations are useful to compare the performance differences between them and the standard notch because parameters can be very precisely controlled and repeatable. Simulations bypass issues in real data that

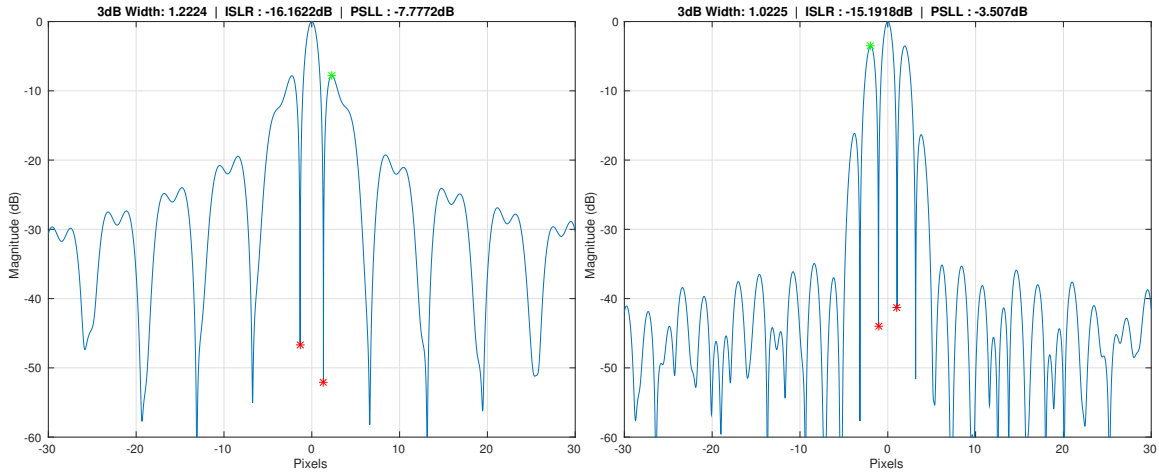

(a) Standard notch IPR **(b)** Split window notch IPR

Figure 6.4: Comparison of the IPR for point targets after applying (a) standard notch and (b) split window notch mitigation techniques for 20% of data samples notched from the center of the fast-time data.

include mis-registration, non-ideal IPR, autofocus, and inhomogeneous scattering mechanisms (e.g. shadows introduce decorrelation amongst correlated terrain). These simulations are for the single aperture mitigation algorithms, therefore all CCD products and coherence measures are computed with a reference image free of any interference or mitigation effects. Because the reference image is 'clean,' average coherence values are indicative of image quality. The simulation parameters in Table 6.1 have been modeled after the parameters of the real data set used in the following section and parameters from chapter 4.

Center Frequency	16.8GHz
Resolution	0.1524m (6")
Scene Size	100m Range 120m Cross-Range
Image Oversample Factor	1.5
Window Function	Taylor $\bar{n} = 4$ -35dB SLL
Terrain RCS	-28dB
Point Target RCS	25.5dB
Noise RCS	-38dB

Table 6.1: Coherence comparison simulation parameters

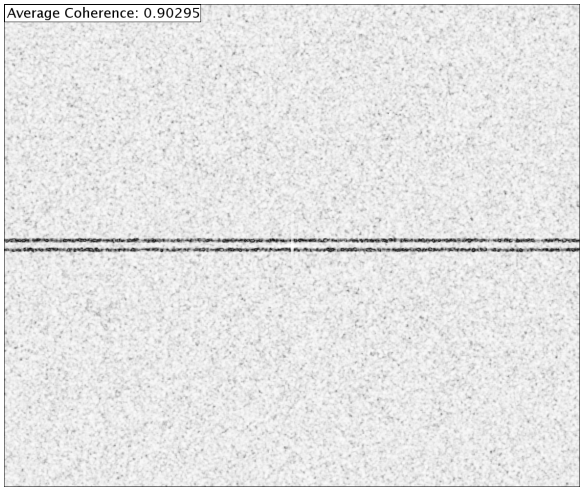

Figure 6.5: Ideal case for the qualitative simulation image without interference or interference mitigation. The decorrelation pattern approximates tire tracks. Image contains a single point target at the center.

The performance metrics of merit have been identified and explained in chapter 4. To measure the performance metrics the simulation requires three images to be simultaneously processed. To measure average coherence, one image is composed entirely of clutter (i.e. terrain) without any changes to clutter other than thermal noise. A second image is required to estimate the PDF parameters of the change and no change regions of a CCD to generate ROC curves. As explained in chapter 4, this image does not contain an interference signal to preserve the PDF characteristics of the coherence values. This image does include a point target in the center of the scene, but it doesn't affect the PDF characteristics because the guard bands for PDF estimation around each change and no change region exclude the pixels of the point target. Any distortions to the IPR from interference mitigation spread in the range direction and do not intersect into either change or no change regions. A third image includes a pattern of disturbances and a point target at the center for a qualitative check of the average coherence and contrast performance. Figure 6.5 shows the qualitative CCD image used in all simulation cases without interference or mitigation techniques applied; this is the ideal CCD image. The decorrelation pattern chosen approximates tire tracks and is placed along a horizontal direction in the image to increase any IPR distortion effects in the vertical direction from applying mitigation techniques that increase range sidelobes.

6.3.1 Simulation Results

This simulation will compare the results of using different methods to implement the notch as it varies in size at different locations in the fast-time data. The location of the notch within the fast-time samples affects the amount of distortion [15]. For example, the same notch size located at the edge of the data will result in less IPR distortion than locating the notch at the center of the data [15]. For comparison a case without interference and using the standard notch are each included in simulation results as a benchmark to bound results.

Figures 6.6, 6.7, and 6.8 show simulation results for centering the notch at 3 different locations, the edge, the center, and in-between the edge and center, respectively. Since the IPR is symmetrical, there is no reason to simulate the notch at the other edge. Technically, the notch isn't centered at the edge, it starts at the edge and continues to the number of samples corresponding to the notched percentage. Therefore, Figures 6.6a and 6.7a converge to the same coherence values when the notch reaches a width of 50% of samples.

The overall coherence decreases as the center of the notch moves towards the center of the data samples, due to the increasing IPR distortion predicted by [15]. Overall the spectral notch maintains the best coherence for the same percentage of samples notched. Examination of the contrast ratio via the ROC in all simulations show the spectral notch CCD has superior contrast. Figures 6.6e and 6.6f indicate the contrast ratio is nearly the same as the case without interference.

Although the split window notch results in the lowest coherence for all cases, the qualitative images in Figures 6.6d, 6.7d, and 6.8d show there is no observable coherence loss due to IPR sidelobes of the point target unlike the other mitigation cases. The notch operation generally increases the sidelobe level, however, applying the split window notch is able to better control the sidelobe levels so they are less noticeable. Because the first image doesn't have a mitigation applied, the change in sidelobe level (and shape) causes the vertical decorrelation streak (at the center of the image) observable in the CCD for both the standard notch and spectral notch cases in all simulations.

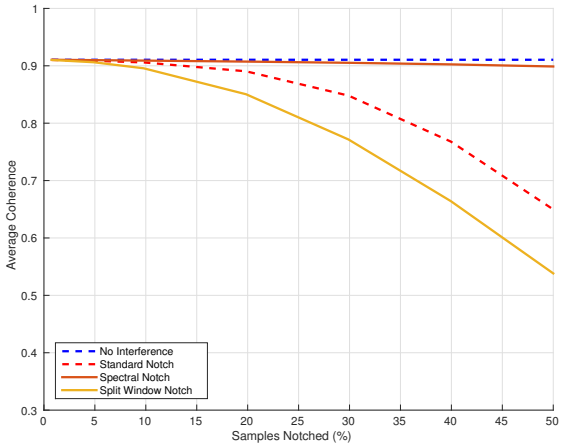

(a) Average coherence comparison

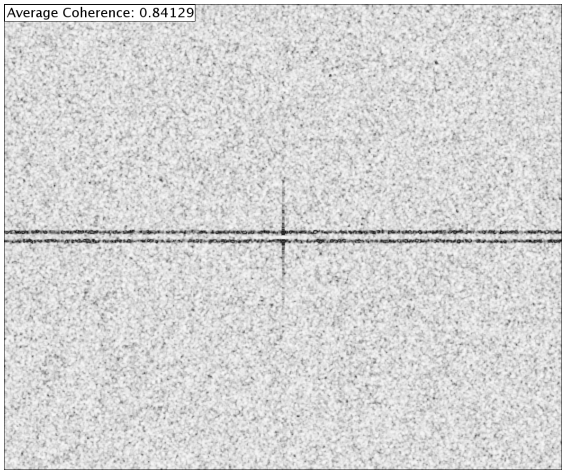

(b) Standard notch CCD (30% samples notched)

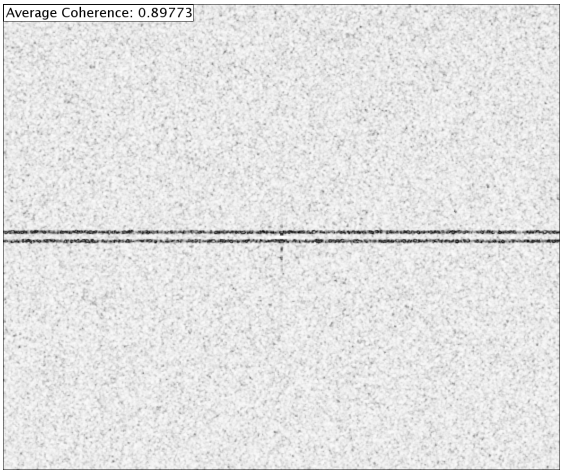

(c) Spectral notch CCD (30% samples notched)

(d) Split window notch CCD (30% samples notched)

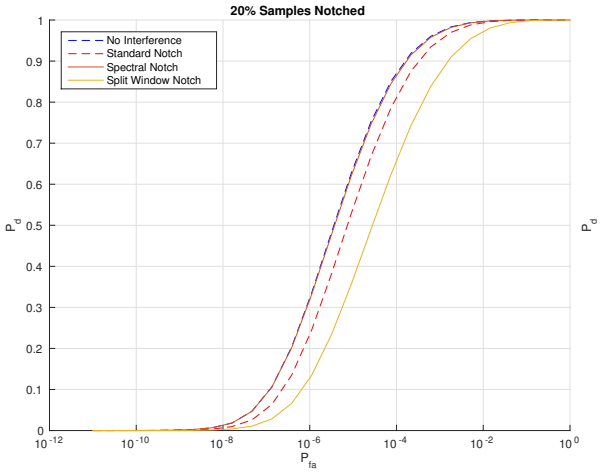

(e) ROC for 20% samples notched

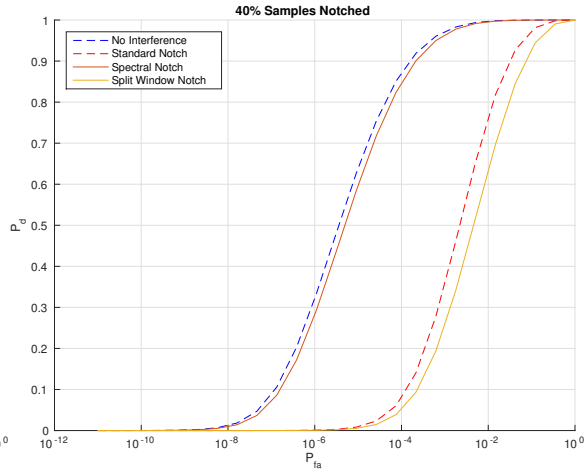

(f) ROC for 40% samples notched

Figure 6.6: Comparison of standard notch, spectral notch, and split window notch where the same percentage of samples have been notched from the edge of fast-time data samples.

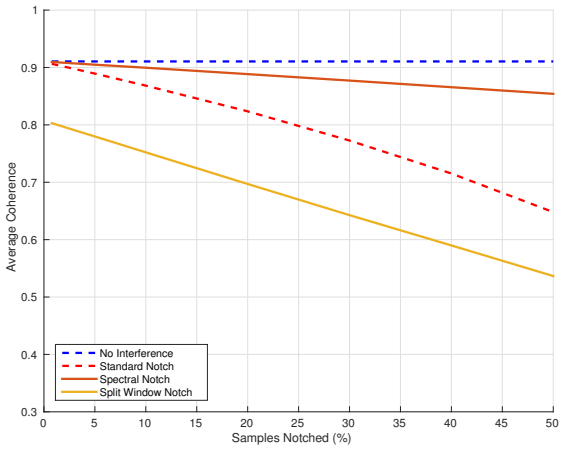

(a) Average coherence comparison

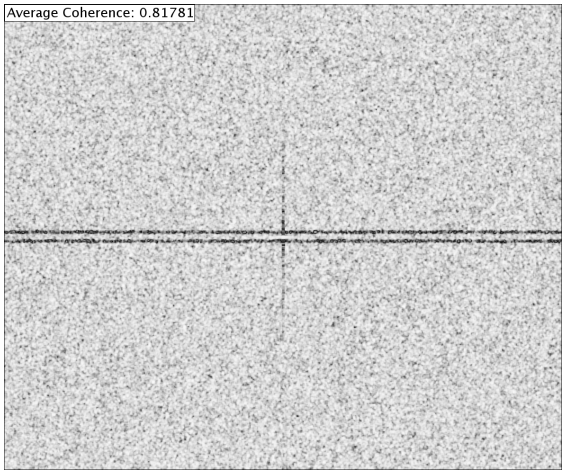

(b) Standard notch CCD (20% samples notched)

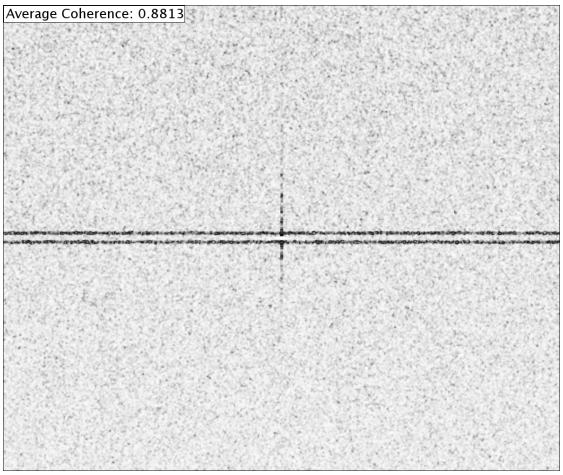

(c) Spectral notch CCD (20% samples notched)

(d) Split window notch CCD (20% samples notched)

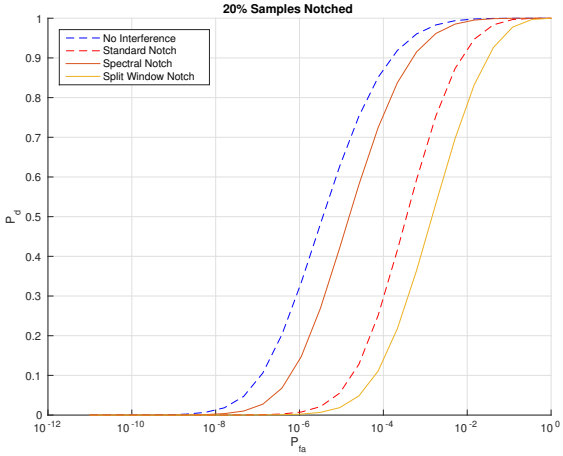

(e) ROC for 20% samples notched

Figure 6.7: Comparison of standard notch, spectral notch, and split window notch where the same percentage of samples have notch centered between the edge and center point of fast-time data samples.

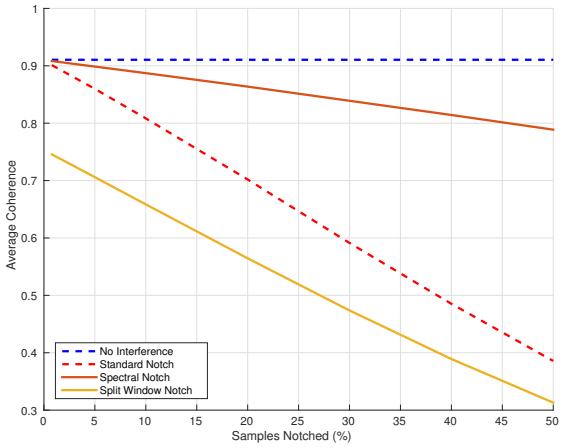

(a) Average coherence comparison

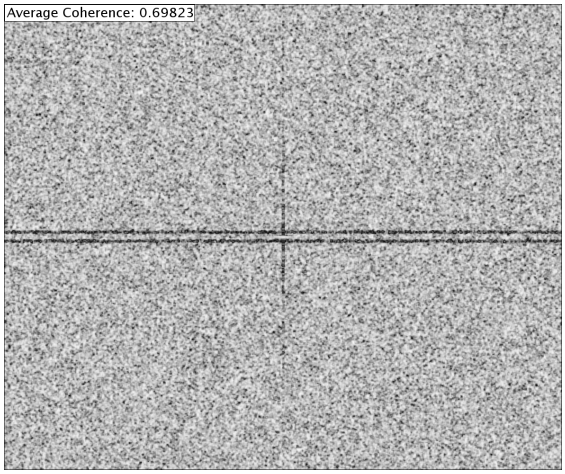

(b) Standard notch CCD (20% samples notched)

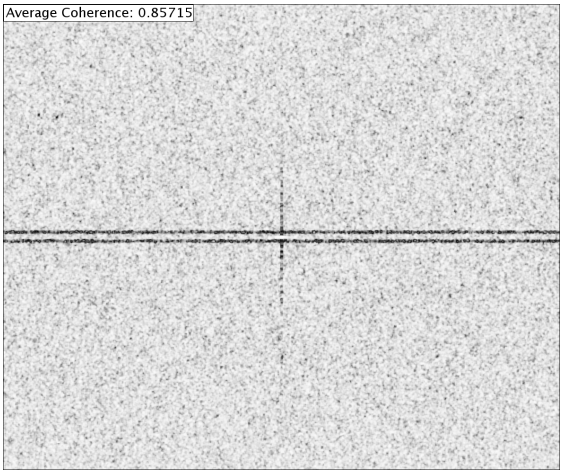

(c) Spectral notch CCD (20% samples notched)

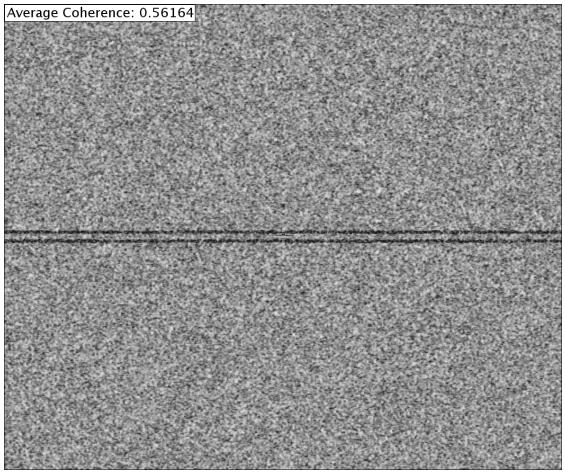

(d) Split window notch CCD (20% samples notched)

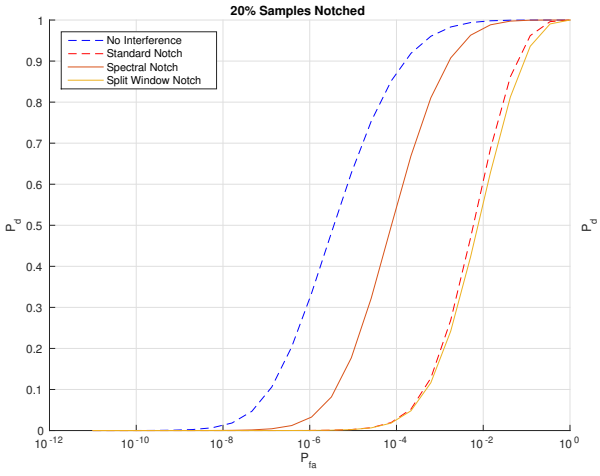

(e) ROC for 20% samples notched

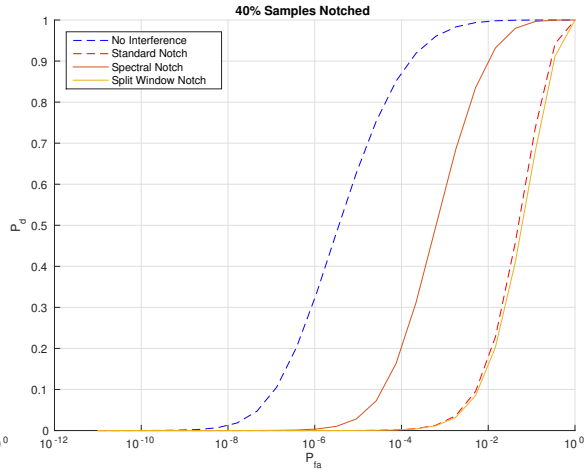

(f) ROC for 40% samples notched

Figure 6.8: Comparison of standard notch, spectral notch, and split window notch where the same percentage of samples have been notched from the center of fast-time data samples.

6.4 Real Data Examples

The simulations use a CWGN model as an approximation for terrain. This section will use real SAR data of terrain to test the impact of the different mitigation methods upon average coherence and present some qualitative examples. The contrast cannot be measured for this data because there is no single homogeneous region of change or no change from which to estimate statistics.

An interference source is not used within this example. Any type of interference source would require some form of detector to identify the data samples containing interference. Any implemented detector cannot perform identically for the spectral notch, standard notch, and the split window notch. If the detectors for each mitigation technique are not identical, then interference energy not detected by the detector is present within the image products and lowers the coherence estimate, obscuring the coherence effects due solely to the mitigation method.

Instead of an interference source and detector, these examples place a notch centered within the fast-time data and vary the width of the notch up to 50% of the fast-time data length to correspond to the simulation results in Figure 6.8. Representative images and CCDs are shown in Figure 6.9 to illustrate the visual effects of each mitigation technique upon the image and CCD products for when 20% of data samples are notched. Figure 6.9a shows the spectral notch yields the best coherence as the simulation in Figure 6.8 predicted. Visually, the spectral notch CCD in Figure 6.9f appears dramatically improved over the standard notch and split window notch in Figures 6.9d and 6.9h, respectively. It is interesting to note that although the split window average magnitude coherence is the lowest in all cases, its image in Figure 6.9g appears good because it does not have the high sidelobe levels that create the vertical streaking artifacts present in the other images.

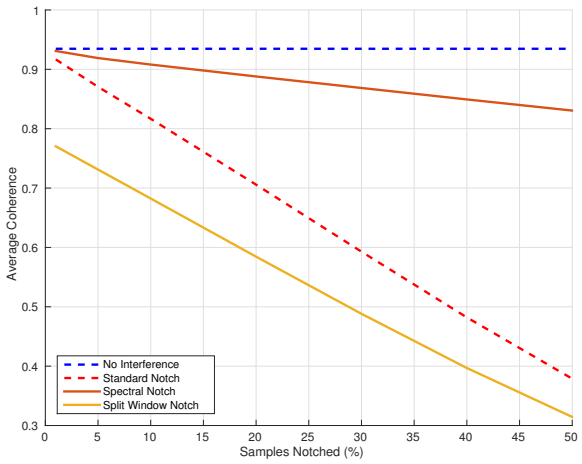

(a) Average coherence comparison

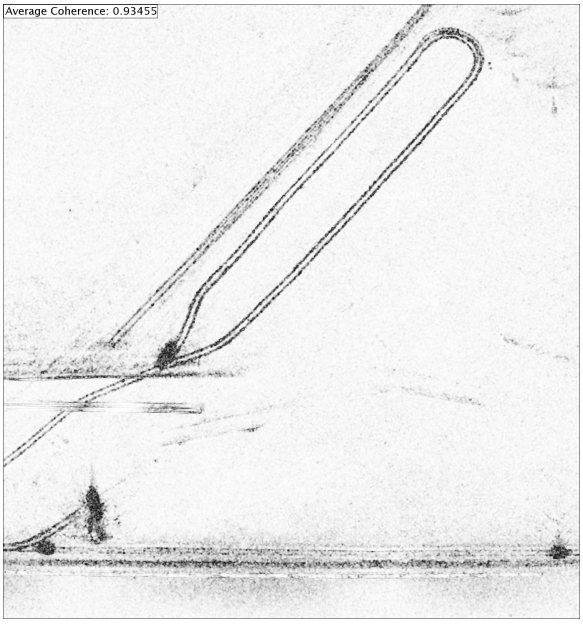

(b) Original CCD - no interference

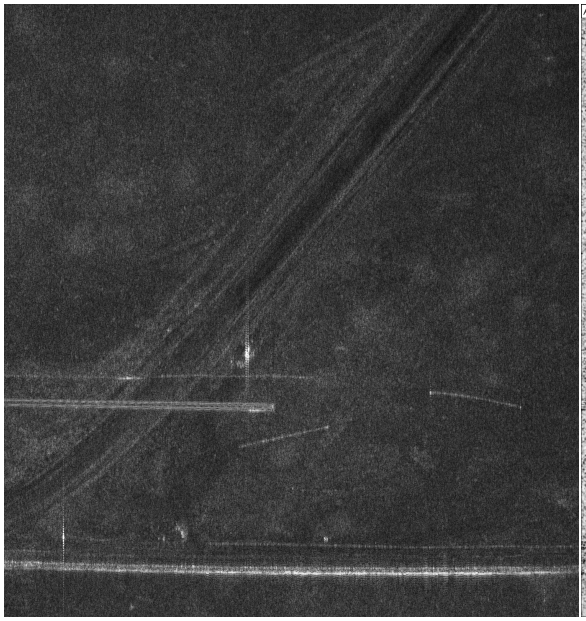

(c) Standard notch image
(20% samples notched)

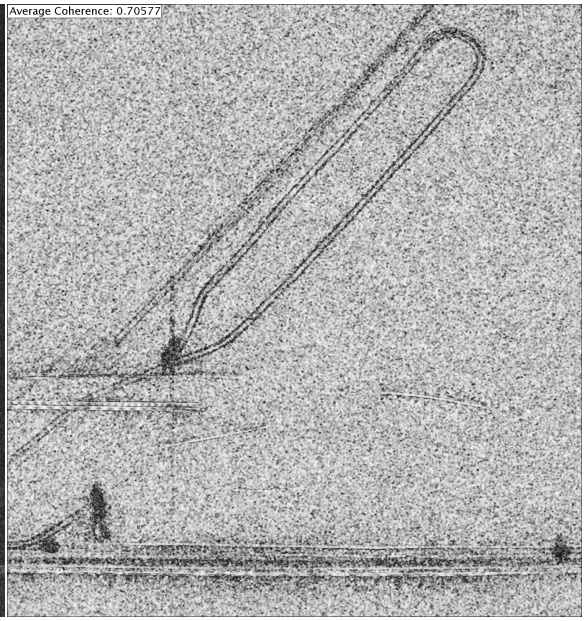

(d) Standard notch CCD
(20% samples notched)

Figure 6.9: Evaluation of standard notch, spectral notch, and split window notch mitigation techniques at prescribed notch widths centered within fast-time data. *(continued on next page)*

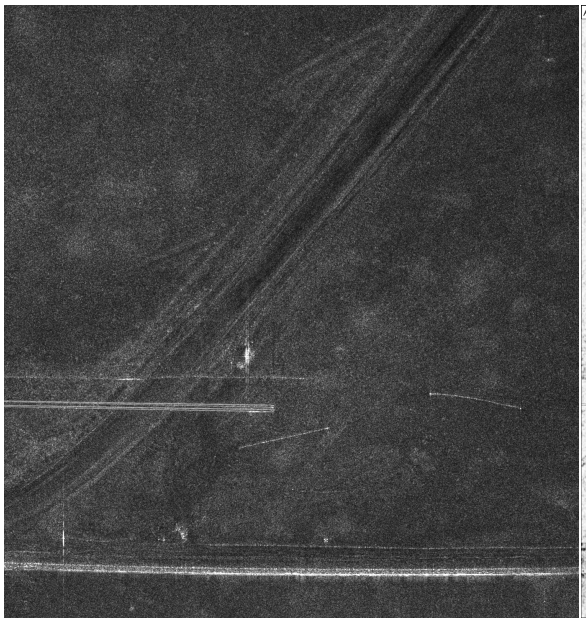

(e) Spectral notch image
(20% samples notched)

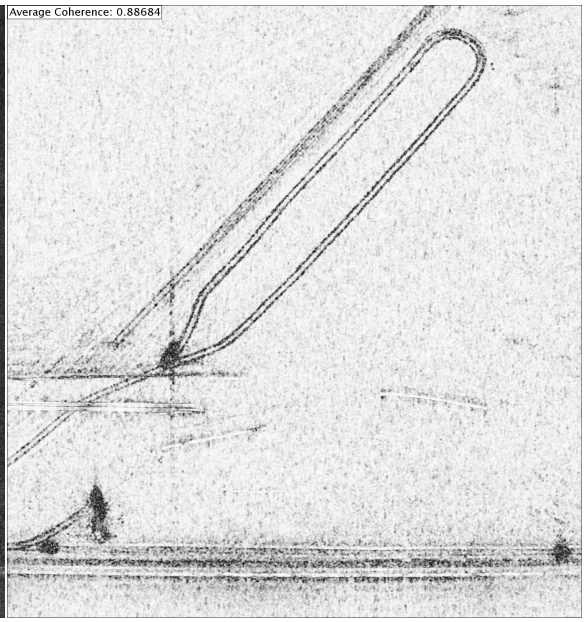

(f) Spectral notch CCD
(20% samples notched)

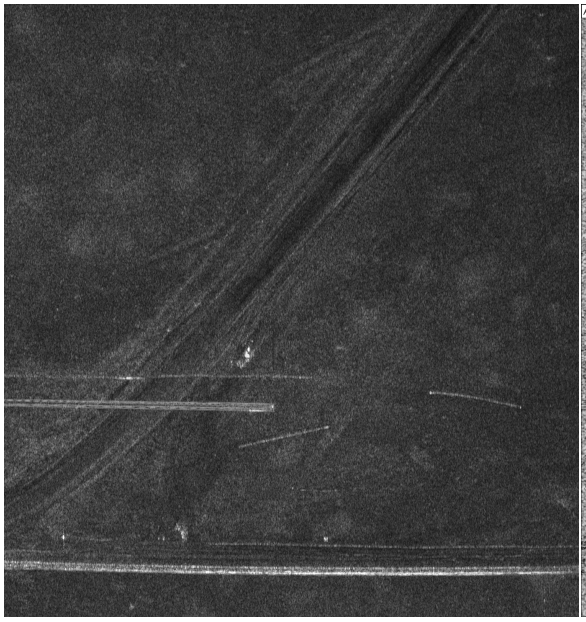

(g) Split window notch image
(20% samples notched)

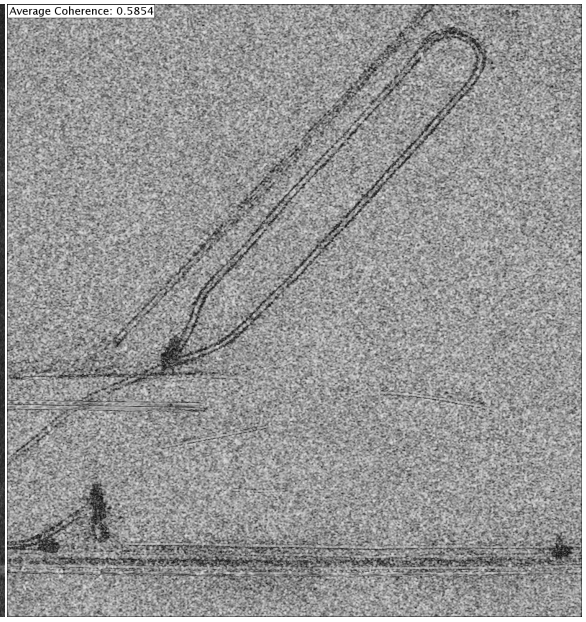

(h) Split window notch CCD
(20% samples notched)

Figure 6.9: Evaluation of standard notch, spectral notch, and split window notch mitigation techniques at prescribed notch widths centered within fast-time data.

6.5 Summary

The performance of two novel mitigation algorithms called spectral notch and split window notch has been evaluated against the standard notch when applied to one of the images in the coherent pair. It has been shown that mitigation at the center of the data samples is the most damaging to coherence, as IPR distortion predicted in [15]. It has also been shown that notching the RF spectrum via the spectral notch technique is the least damaging to the IPR by evaluating the average coherence. However, it should be noted that the qualitative image quality of the split window notch appears to be superior due to the overall lower sidelobe level, even when compared to the spectral notch.

This chapter has limited the corrections to only one of the images in the coherent pair. While this expresses image quality into the average coherence measurement, it has ignored the fact that maximum coherence arises from spectral overlap between the coherent pair of images [17, 18, 55]. The next chapter will evaluate methods that maximize the spectral overlap between the coherent pair of images.

CHAPTER 7

MULTIPLE APERTURE INTERFERENCE MITIGATION

Throughout this dissertation, it has been assumed that the radar is a single-channel system whereby second order image products are created from subsequent passes, or collections. This chapter examines the case where interference mitigation manipulates both apertures. Previously, in the single aperture techniques a reference image without interference was used to make CCD products. The average coherence of the CCD encapsulated the image quality resulting from the applied mitigation algorithm. However, when evaluating multiple aperture techniques the average coherence no longer indicates image quality. Multiple aperture techniques make it possible to remove the IPR/spectrum mismatch that occurs from notching a single image of the coherent pair by corrupting both apertures in the same way. It is well known that aperture alignment of the phase histories of a CCD/IFSAR product is critical to maximizing coherence [17, 18, 55]. Only applying a notch to one image exacerbates the spectral mismatch, but if the notch is applied to both apertures, for the same spectrum then any coherence loss due to the IPR mismatch is removed. There are disadvantages to applying the notch to both apertures, such as poor image quality.

In this chapter, two novel methods are introduced to mitigate interference that requires making adjustments to both apertures of the CCD/IFSAR product. The first technique, called co-notch, combines the concept of aperture alignment with the standard notch to mitigate interference by identically notching both data collections of the coherent image pair, regardless if only one aperture contains interference. The second technique, called split window co-notch, is a modification of the standard window function where instead of applying a single window function across the entire data span, the window function is

split at the notch to smooth the transition between the notched and retained data spectrum. Each technique is explained in detail with an analysis of the image quality and coherence performance.

7.1 Co-Notch

The concept of aperture alignment is not new for coherent data processing and it is well documented in many sources [17, 18, 55] that deviations in the flight path can cause frequency and azimuth shifts in the spectrum between successive data collections. Applying this concept to interference mitigation means that both phase histories of the coherent data pair must be notched in the same way. Notching interference is an effective way to remove all possible image artifacts resulting from the interference signal. However, the amplitude/phase discontinuity from notching results in a poor image IPR. When only one image in the coherent pair has a poor IPR, a coherence loss occurs. Aperture trimming will remove the loss associated from the IPR mismatch by essentially corrupting both IPRs. If the IPRs for each image are identical the average coherence will increase over the cases (in the previous chapter) where only one image is notched, (or when the two images are notched differently).

7.1.1 Algorithm

The challenge is to align the phase history's spectrum between collections. For a real SAR data collection frequency and phase shifts occur between data collections due to non-stationary objects, radar motion, or error of the estimated motion. These frequency and phase shifts, if not properly aligned, can cause decorrelation in point targets and clutter, including decorrelation in the sidelobes.

The radar can be very precise when measuring the phase of its backscattered signal. At 16.8GHz (Ku band) the wavelength is 17.8mm, which means the radar phase can only distinguish between changes in range within a wavelength. If the radar changes its position

by more than a wavelength, then the radar must use other means than the phase to estimate its position or the position of the scatterer. Any unknown errors in these other measures result in unknown phase shifts (including unknown multiples of 2π) between collections.

By whatever means the radar uses to estimate its position, if it is not exactly in the same location for each pulse transmission and reception there will be a phase offset from pass to pass. A constant phase offset doesn't affect coherence, but how the phase offset varies between pulses may affect the coherence [17]. Real-time motion compensation changes the chirp rate and center frequency of each pulse based upon the estimated location of the radar at that point in time. Assuming the estimated location of the radar is accurate, the radar may not be in exactly the same position for each collection. Fundamentally, if the collection angles don't precisely align, the data describes different signals, so coherence is not going to be perfect. The aperture collection plane is a 3 dimensional surface that is a function of spherical coordinates of azimuth angle, grazing angle, and frequency (in radial direction) [9]. There are acceptable tolerances that allow coherent data processing, but technically the signal is not identical unless the collection angles and bandwidth are identical.

Another way to understand this is to consider a resolution cell for terrain consists of many small scatterers randomly distributed within the resolution cell. The backscattering coefficient for randomly distributed scatterers is a random process without correlation from one angle to another so the signal from different angles is a different signal. If the collection angles are repeated, then the backscattering coefficient, though a random process, returns the same backscattering signal.

All of the technicalities of motion mentioned above mean that care must be taken when aligning apertures, and that simulation results may not match results from real data (see discussion in section 7.2 on IPR sidelobe coherence). It turns out that motion doesn't have to be identical between apertures to achieve high coherence due in part to the coherence estimator.

For the reasons aforementioned regarding aperture alignment, mainly not-identical motion between apertures, an excellent place in the image formation process to notch the phase history data is after the phase history is interpolated from polar to rectangular coordinates. The rectangular grid for both apertures is defined based upon a nominal set of coordinates that should be identical for repeat pass data collections. This allows for the actual measurements of position, bandwidth, etc. to vary for each collection as they need to while the interpolation brings these values into coincident data indices that make it easy to notch both apertures.

A block diagram of the processing flow for the co-notch is presented in Figure 7.1. After resampling, a detector of choice can be applied to each aperture to identify the data samples to be notched. The index values from each detector are applied to both images before proceeding to create a coherent data product.

7.1.2 Limitations

The coherence loss from non-overlapping apertures may be eliminated, but because less spectrum is available, the overall coherence value is lower than if there was no notching and no interference. Bickel [17] discusses how increasing resolution increases coherence because there is more spectral overlap.

A related limitation is that if interference is present in both apertures, at similar frequencies, the performance gain of co-notching over notching each aperture may be small.

7.1.3 Applying a Split Window for Improvement

Where the interference occupies a large percentage of the bandwidth, the IPR degradation can be extreme as examples have demonstrated previously in this dissertation. Alternatively, for image formation the range window can be modified as previously described in section 6.2, except now the same split window is applied to the phase history for each image in the CCD pair.

Like in the single aperture case, applying the split window requires a modification of the detector output to identify contiguous regions of interference. For multiple apertures this process gets more complicated by using the detector outputs of both apertures to identify contiguous regions.

7.2 Simulation Performance

Using the metrics described in chapter 4, simulations were created to compare the performance differences from co-notching with a window across the entire aperture (i.e. co-notch) and splitting the range window for each section of contiguous data (i.e. split window co-notch). The simulation parameters and test cases are identical to the single aperture simulations in the previous chapter (section 6.3). For these simulations it is assumed the first aperture of the coherent data product does not contain interference, and the second aperture does contain some kind of interference. The key difference in this chapter is that the mitigation applied to the second aperture is now identically applied to the first aperture even though it does not contain interference. Although this may sound counter-intuitive, as explained earlier, coherent data products must be spectrally aligned to achieve the best coherence [17, 18, 55].

The first set of simulations evaluate the performance of each mitigation with an ideal detector for simulated clutter. The ideal detector detects all samples containing interference. Because these mitigation techniques notch all data samples containing interference to zero value, there is no residual interference signal energy present in the final image products. These simulations show the effects of increasing the number of samples notched for a single notch location in fast-time data. The notch location is varied from the edge, center, and in-between while the size of the notch is increased from 1% to 50% in each location.

From the simulations in Figures 7.2, 7.3, and 7.4, it is clearly shown that applying the same mitigation method to both apertures (using either co-notch or split window co-notch) maintained the average coherence to the level of the no mitigation case. However, there

is an important difference between the co-notch and split window co-notch mitigation for all three cases: IPR. Referring to the standard notch CCD in Figure 7.4b, the point target at the center of the image shows decorrelation as a dark vertical streak because the IPR distortion due to the notch mitigation does not match the IPR of the original image. This phenomenon is present in the other cases in Figures 7.2b and 7.3b, but is most pronounced in the case the notch is centered in the fast-time data samples for Figure 7.4b. When both images are notched the same, the IPR, although distorted, no longer is different between the two images and correlates to create the vertical white streak shown in Figure 7.4c. In this case the sidelobes are correlated because this is a simulation. The phase history response of a point target is exactly identical in both apertures because the simulated motion is exactly the same. The point target response is identical between the two apertures, including the sidelobes. Because the sidelobe level is higher than the surrounding clutter, it is visible as a white streak. Real motion throughout a synthetic aperture data collection is not going to be identical between passes; this subtle position difference changes the recorded range to a point target and its associated phase measurement so the IPR between the two image is not going to be strictly identical. In the following section, real SAR data is used to show the point target sidelobes in the co-notch CCD are not correlated and visible as black streaks. Also, notice the sidelobe structure of the split window co-notch in Figure 7.4d is greatly reduced from that of the co-notch in Figure 7.4c. The smaller sidelobe correlation (or decorrelation for real data) is desirable for CCD images because it limits the contribution the point target has upon its neighboring pixel values. Because the point target can have more energy than the surrounding clutter its coherence may obscure any changes within the CCD. Likewise, for height maps the phase of the point target may prove problematic for 2D phase unwrapping algorithms or falsely influence the height measurements of the neighboring pixels. In all cases, it is desirable to limit the spread of any scatterers throughout the image as much as possible. This average coherence impact of sidelobes is negligible in the simulation case because there is only one point target so any sidelobe

correlation (or decorrelation) is only a small contribution to the average coherence. Later, real data examples provide a clearer distinction in average coherence performance.

Notice that the ROC in Figure 7.4e shows the probability of detection is higher for the split window and co-notch mitigations than the no interference case while the other ROC curves at 20% notch in Figures 7.4e and 7.4e do not indicate that any mitigation method results in a higher probability of detection than the no interference case. To explain this difference, first remember the ROC curves are measuring the separability between the coherence values for the change and no change PDF, not the probability of detecting any feature. It turns out after estimating the coherence and effective number of looks that there is a very slight change in the overlap regions of the change and no change case histograms for the ROC in Figure 7.4e. This slight change in overlap is most likely due to the error estimating the PDF parameters. To show how similar the estimated values for the no interference, co-notch, and split window co-notch are Table 7.1 displays the estimated coherence values. Considering the coherence estimator increases its bias and variance as the true coherence decreases [17], and the coherence estimator is used to create the CCD from which the values are used to estimate the parameters in Table 7.1. There is some error in estimating the change PDF parameters for the split window case that slightly increases its coherence value. The coherence value estimated for all the mitigations should be zero, but as stated before the coherence estimator is biased at low coherence values. The change in the μ_{change} values for different mitigation methods is consistent with the increased variance in the coherence estimator for low coherence values. So actually the split window most likely doesn't have a superior contrast to applying no mitigation, it is more likely the contrast is very similar to the no mitigation case. The results of this ROC show that despite notching the center of the phase history, where IPR distortion is the worst, the separation between the change and no change case values remains as well as when no notching is applied.

	μ_{change}	L_{change}	$\mu_{nochange}$	$L_{nochange}$
No Mitigation	0.1537	9.7961	0.9092	8.1141
Standard Notch	0.1358	11.6791	0.6879	8.5181
Co-Notch	0.1589	10.7911	0.9091	8.5911
Split Window Co-Notch	0.1648	10.0501	0.9096	8.1741

Table 7.1: Estimated coherence PDF values for Figure 7.4e

7.3 Real Data Examples

As the case with the single aperture mitigation comparisons, no interference source has been added to the data in these examples so only the performance of the mitigation technique is observed in the results by eliminating any possibility of residual interference energy contributions to coherence loss. Any residual interference energy is an indication of the detector performance, not the mitigation performance.

The real data example for multiple aperture mitigation uses the same data and parameters as the single aperture real data example in Figure 6.9 and mirrors the simulation in Figure 7.4. Figure 7.5a shows average coherence plotted as a single notch of varying width (from 1% to 50% of the data vector length) centered within the fast-time data. Overall, applying the same notch mitigation to both images results in nearly restoring the original average coherence value before mitigation with a slight average coherence degradation increasing with the percentage of samples notched that was not observed in simulations due to sidelobe decorrelation. The most notable difference between the co-notch mitigation in Figure 7.5c and the split window co-notch in Figure 7.5d is the effects of the IPR sidelobe decorrelation discussed in section 7.2. The bright targets in the scene produce a distorted IPR with sidelobe levels that appear as dark vertical streaks in Figure 7.5c (less noticeable in Figure 7.5b due to the overall lower coherence) and affect pixels over a large portion of the image. Notice in particular the dark vertical streaks along the bright return from the fence line at the bottom of the image appear decorrelated due to subtle difference in aircraft/radar motion between the two collections. Another, effect from high sidelobe lev-

els to observe is the bright targets that have changed positions between collections created decorrelated (dark) vertical streaks throughout much of the image in Figure 7.5c because the target has moved there is no poor sidelobe structure to correlate so average coherence decreases. The high correlation of the clutter in Figure 7.5c shows that the IPR sidelobes, not the mainlobe response, are causing decorrelation which is consistent with simulation results that showed high correlation for clutter in Figures 7.2b, 7.3b, and 7.4b. Overall, Figure 7.5d shows that even though resolution has been lost by the notch, the lower sidelobe level from applying the split window co-notch greatly reduces the extent of the sidelobe decorrelation effects and results in a clearer, higher coherence CCD. When Figure 7.5d is directly compared to the original CCD, (without interference), in Figure 6.9b there is little difference between the two.

7.4 Summary

Two novel interference mitigation techniques have been introduced to restore coherence. It turns out that spectrally aligning both apertures in the coherence pair may not yield the best coherence. Because in a multiple pass data collection objects can appear and disappear from the images and motion isn't identical between passes, the sidelobe decorrelation can become problematic. Therefore the split window co-notch shows it is best to apply a mitigation equally to both apertures that minimizes the sidelobe level, even at the expense of mainlobe broadening and distortion.

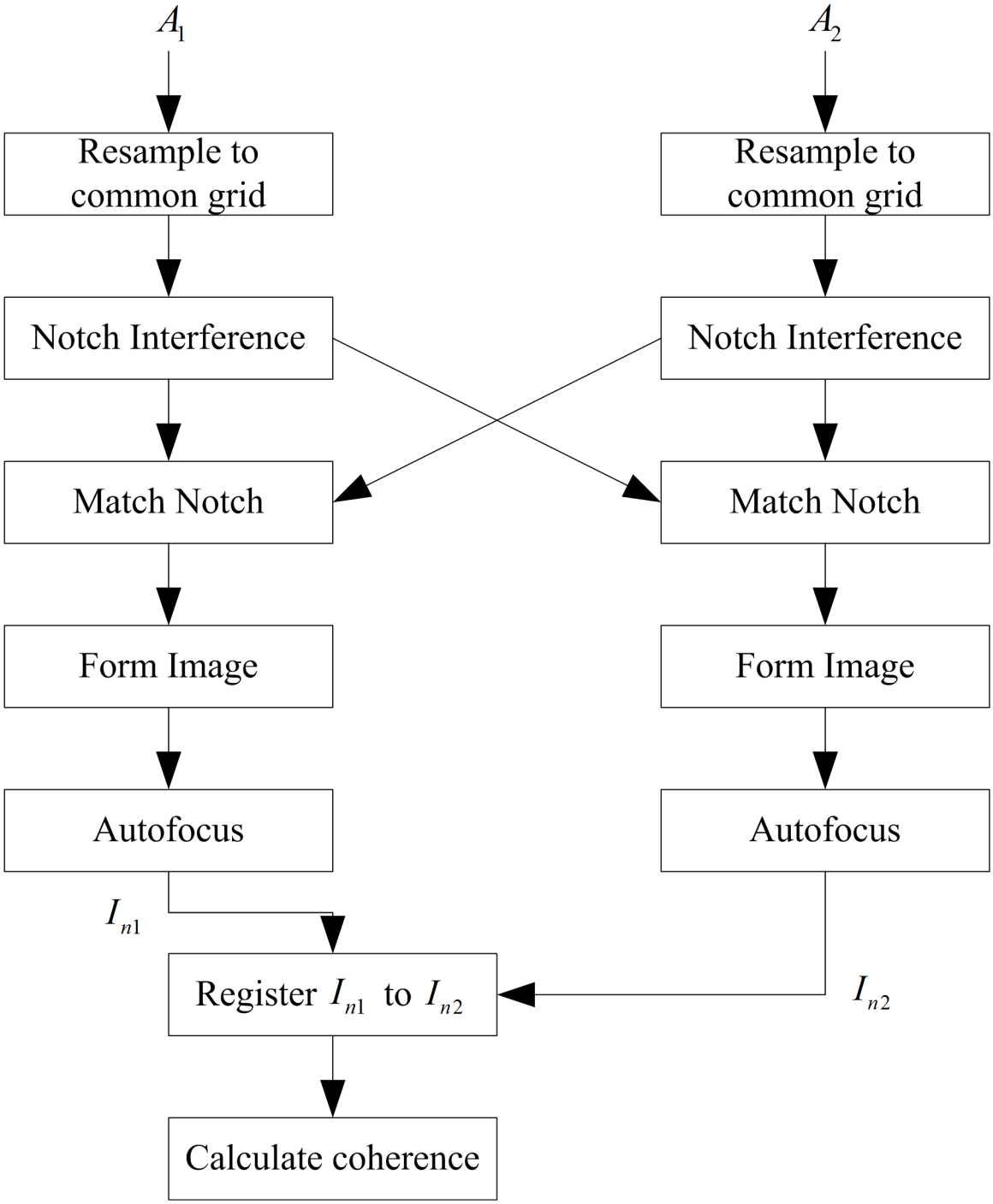

Figure 7.1: Block diagram of co-notch algorithm.

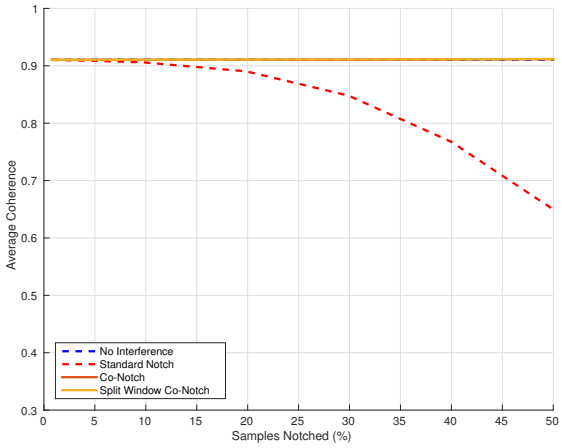

(a) Average coherence comparison

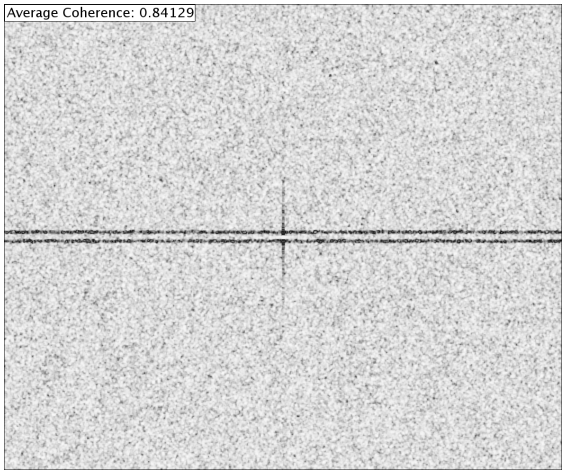

(b) Standard notch CCD
(30% samples notched)

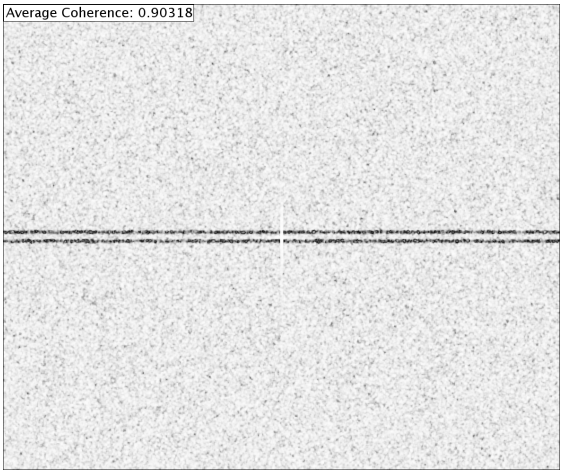

(c) Co-notch CCD
(30% samples notched)

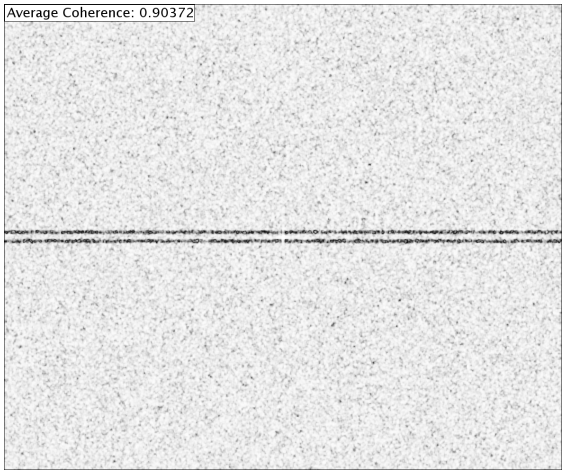

(d) Split window co-notch CCD
(30% samples notched)

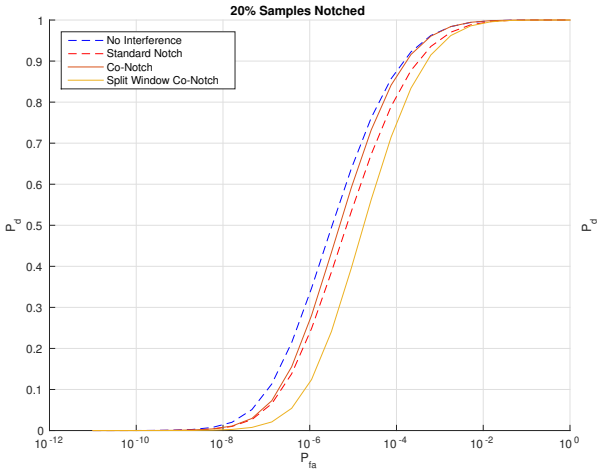

(e) ROC for 20% samples notched

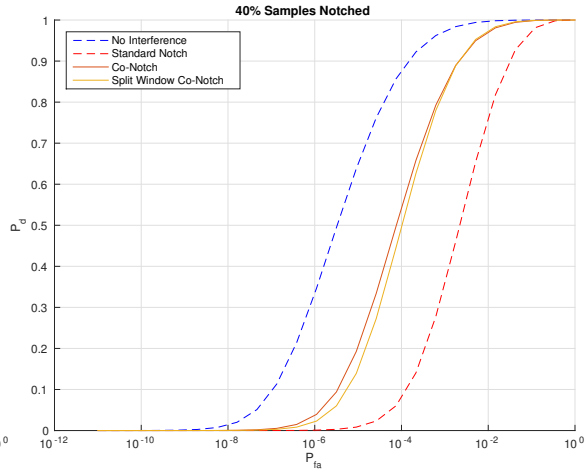

(f) ROC for 40% samples notched

Figure 7.2: Comparison of standard notch, spectral notch, and split window co-notch where the same percentage of samples have been notched from the edge of fast-time data samples.

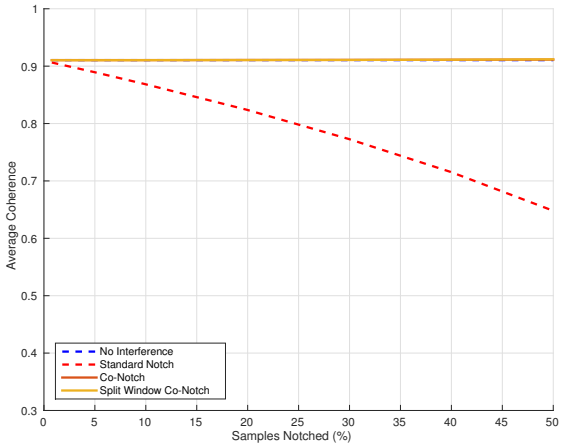

(a) Average coherence comparison

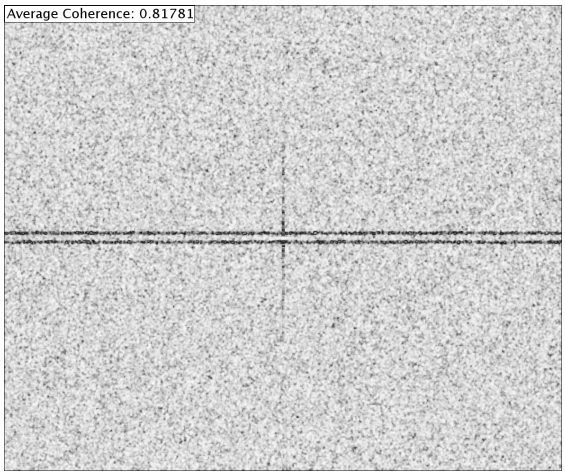

(b) Standard notch CCD
(20% samples notched)

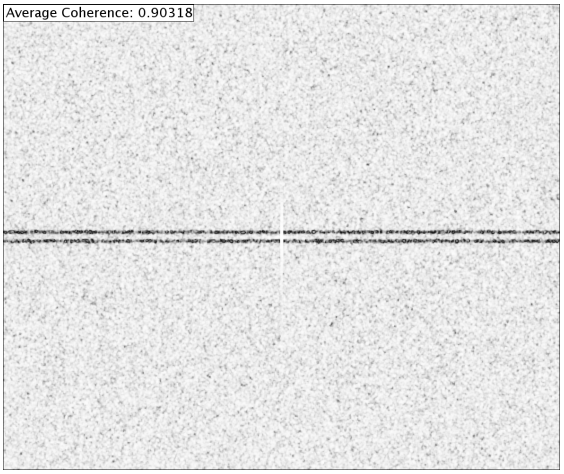

(c) Co-notch CCD
(20% samples notched)

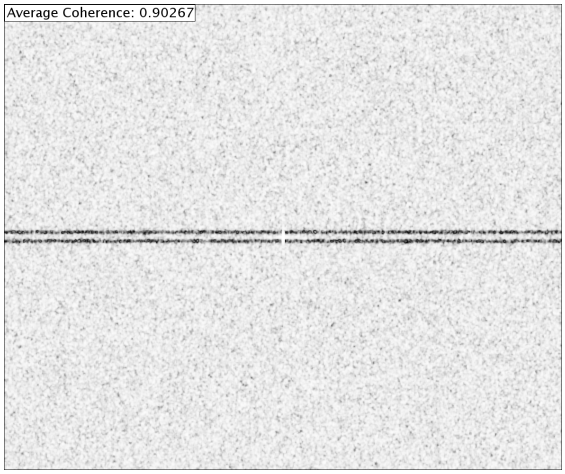

(d) Split window co-notch CCD
(20% samples notched)

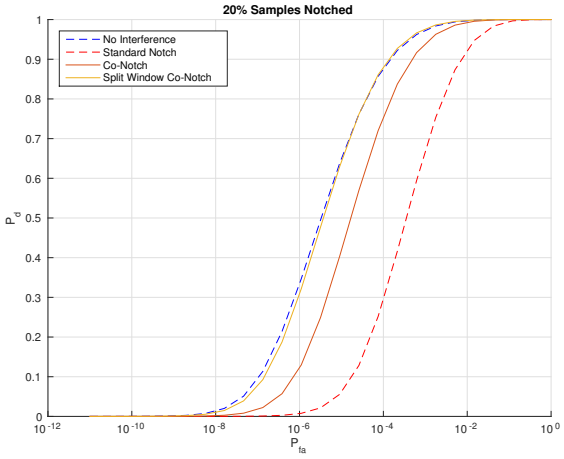

(e) ROC for 20% samples notched

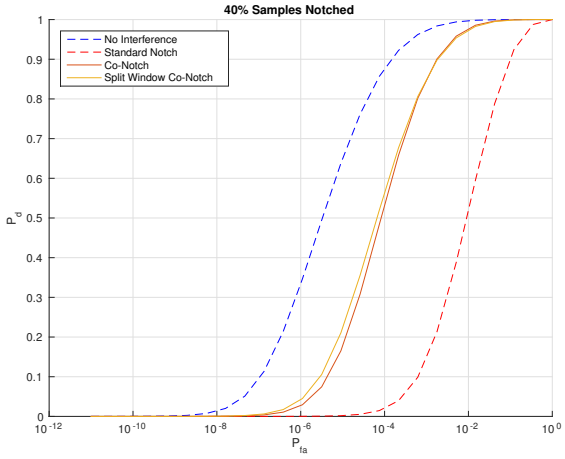

(f) ROC for 40% samples notched

Figure 7.3: Comparison of standard notch, co-notch, and split window co-notch where the same percentage of samples have been notched centered between the edge and center of fast-time data samples.

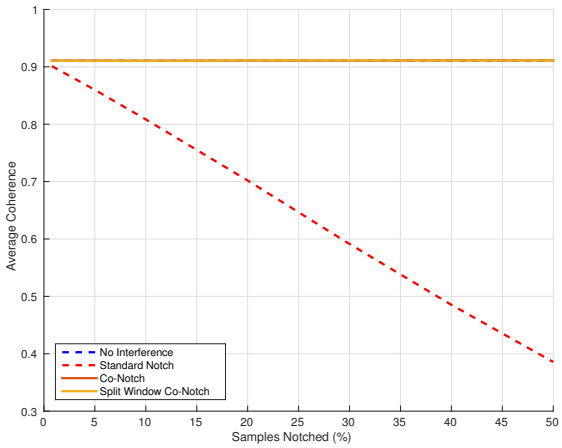

(a) Average coherence comparison

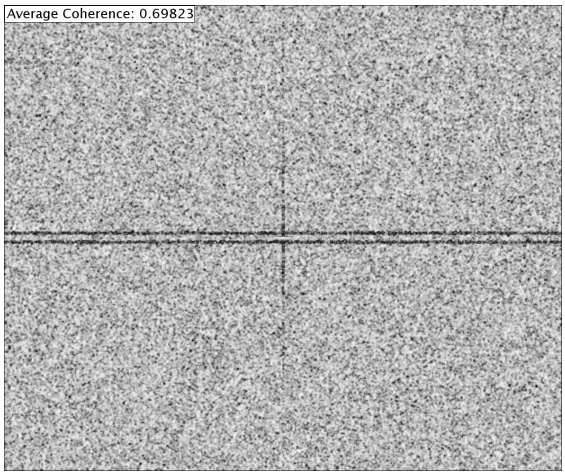

(b) Standard notch CCD
(20% samples notched)

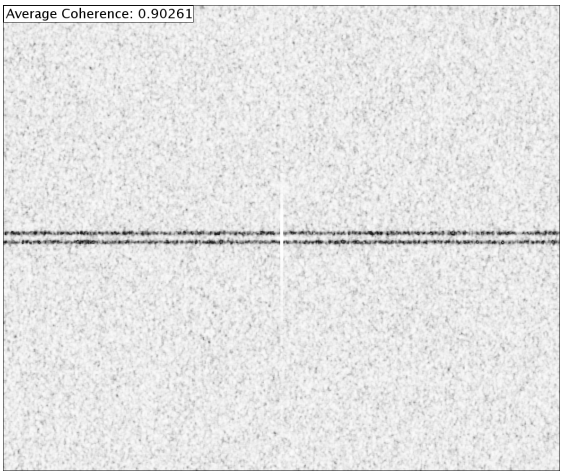

(c) Co-notch CCD
(20% samples notched)

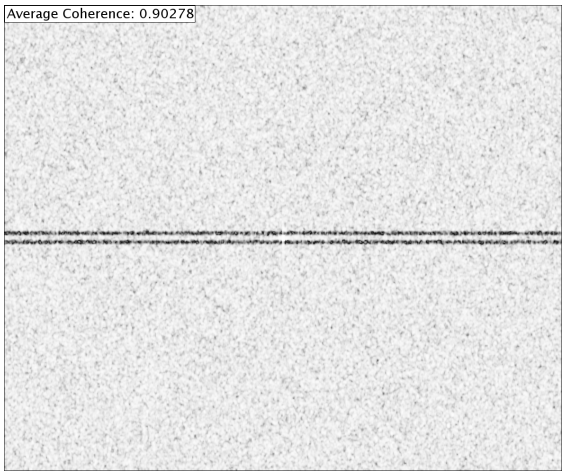

(d) Split window co-notch CCD
(20% samples notched)

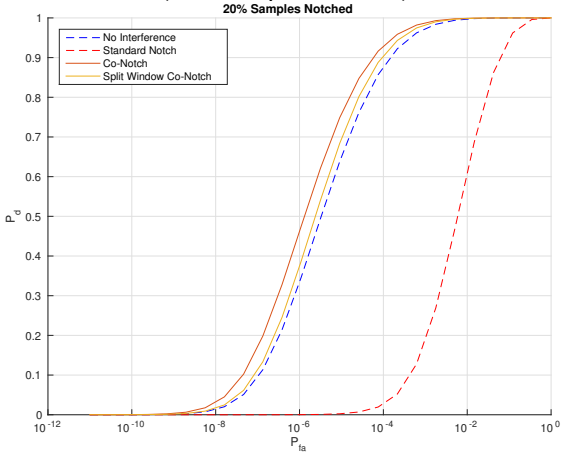

(e) ROC for 20% samples notched

Figure 7.4: Comparison of standard notch, spectral notch, and split window co-notch where the same percentage of samples have been notched from the center of fast-time data samples.

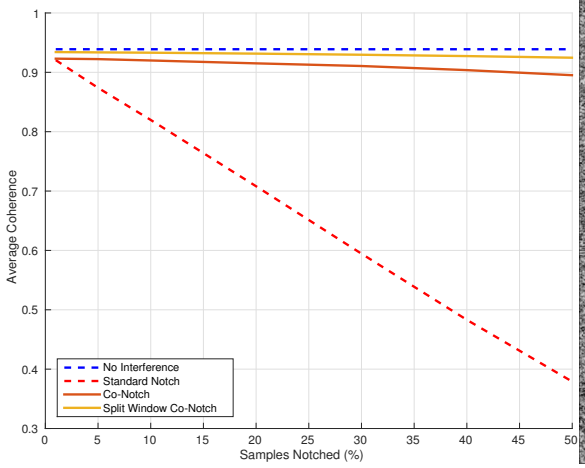

(a) Average coherence comparison

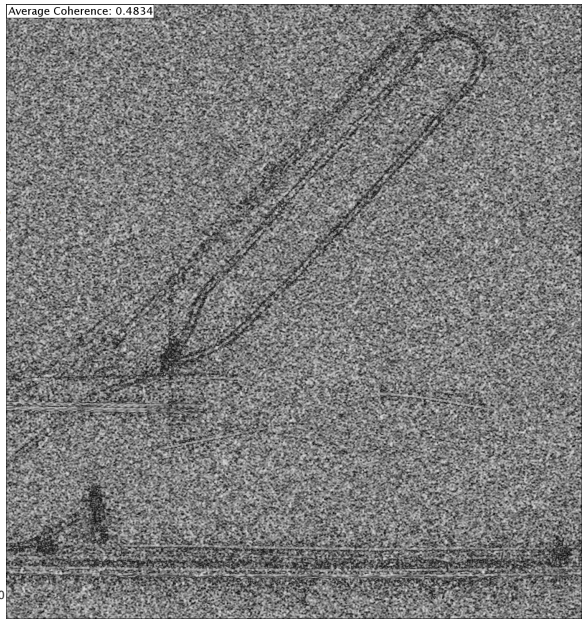

(b) Standard notch CCD
(40% samples notched)

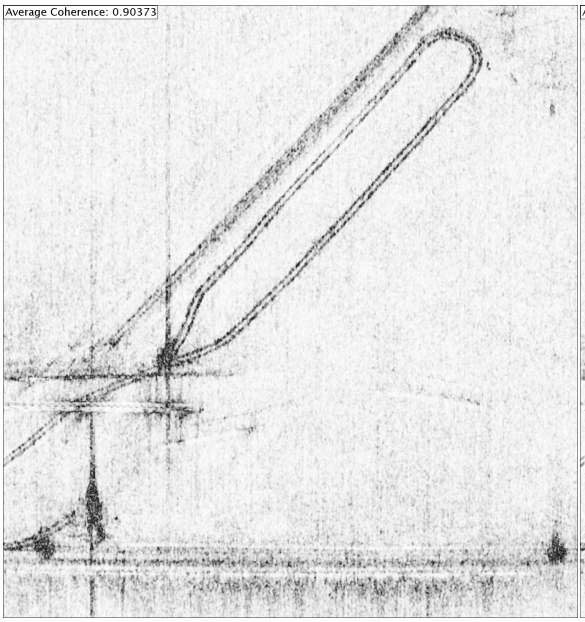

(c) Co-notch CCD
(40% samples notched)

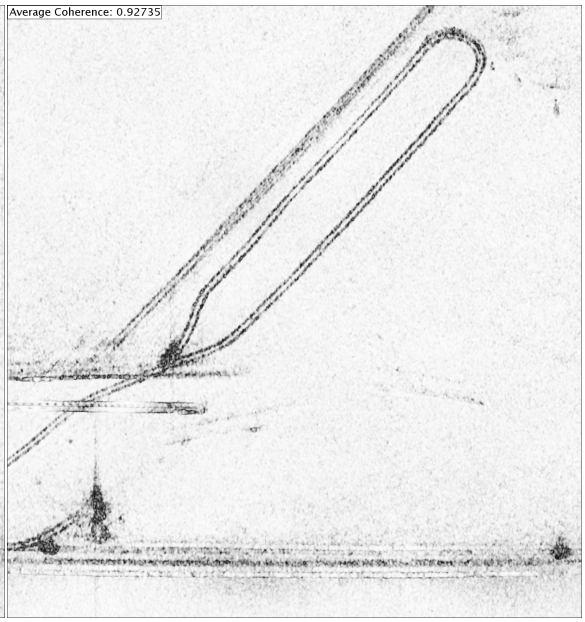

(d) Split window co-notch CCD
(40% samples notched)

Figure 7.5: Evaluation of the (b) standard notch, (c) co-notch, and (d) split window co-notch interference mitigation techniques applied to both apertures of a coherent data pair at prescribed notch widths centered within fast-time data. For the original CCD without interference see Figure 6.9b.

CHAPTER 8

CONCLUSION

For many SAR systems, the coherent data product is the most important product of the radar. Whether making a height map of terrain or coherent change detection a synthetic aperture radar will do that job through clouds, rain, at night, or at long stand-off distances. In the increasingly co-operative RF environment the synthetic aperture radar must continue to do its job despite RF interference. It has been shown for deramp radars most existing interference mitigation methods cannot apply or do not preserve the coherent data product in all conditions.

8.1 Current Results

In total four novel methods have been demonstrated throughout this dissertation to improve coherence under particular conditions. For cases when SIR is high, equalization can improve coherence. For cases where only one image receives interference mitigation, the spectral notch can yield a performance improvement over the standard notch. Although, if the image product is all that is desired, for substantially less computation the split window notch works well. If it is possible to process both images at the same time, then co-notching or split window co-notch for both images yields the highest coherence.

This dissertation has reinforced aperture alignment is key to maximizing coherence, but has revealed that it is not enough. While most mitigation techniques have been concerned with repairing the IPR to an ideal response or minimizing the mainlobe to sidelobe energy levels, this dissertation shows that it is really the sidelobe level that makes the most difference in the average coherence. The two mechanisms causing sidelobe decorrelation in

coherent data products come from objects that appear and disappear in the time between collections and the unique motion between collects that influence subtle differences in the sidelobe structure between collections.

Despite the need to trim both apertures the same, the single aperture mitigation case is very important to consider for any mitigation technique. Coherence is a powerful metric to evaluate the effectiveness of a mitigation technique, particularly techniques that attempt to coherently remove the interference signal or reconstruct missing data samples. If the mitigation technique was truely successful at either task, the IPR of the image (point targets and clutter) would be restored to ideal conditions. But IPR measurements require a point target to make effective measurements, whereas the change in the clutter IPR can be better approximated with coherence. Even if the mitigation was not absolutely perfect, in many cases the sidelobes from point targets and clutter may be below the clutter level and their decorrelation would not be noticeable in the CCD product.

Another novel contribution of this dissertation was applying the ROC to measure the contrast in the CCD product as a result of applying an interference mitigation method. It is conceivable that a mitigation method, particularly ones that use multiple apertures of data, can artificially increase the average coherence to appear to outperform other mitigation methods. However, measuring the contrast via the ROC ensures that adequate separability is maintained between regions of change and no change.

Many interference mitigation techniques do not apply image quality metrics to evaluate the results of the mitigation technique. Very few mitigation techniques [21,27,43] consider coherence impacts of the mitigation itself. This dissertation is novel in that is uses several quantifiable metrics to evaluate the performance of mitigation techniques and compare them. These novel metrics include IPR, average coherence, and CCD contrast.

8.2 Future Work

It has been shown [54] that it is not possible to achieve a desirable mainlobe to sidelobe ratio by applying a window function across the entire span of data when it contains a notch. Future investigations should focus upon selecting an aperture weighting that can be equally applied to both apertures while minimizing the sidelobe level, at the expense of the mainlobe width.

Another topic for study is the effect of mitigation techniques upon the change detection target signatures. A simple contrast metric was used in this dissertation to quantify the distinction between change and no change cases in the CCD. What really is needed is an analysis of the true coherence for a particular target signature and how its coherence changes with respect to mitigation method. Furthermore, depending on the shape characteristics of the target signature, its detector may require a particular contrast ratio that can then be used as a threshold to select a mitigation method.

The next step to implementing the results of this dissertation for practical interference mitigation is to combine this analysis with a detector. The performance of a detector varies according to the types of interference; this is why a detector is not used in this general evaluation of interference mitigation methods.

REFERENCES

[1] T. Rappaport, W. Roh, and K. Cheun, "Mobile's millimeter-wave makeover," *IEEE Spectrum*, vol. 51, no. 9, pp. 34–58, Sep. 2014.

[2] "DoD Releases Electromagnetic Spectrum Strategy," Feb. 2014. [Online]. Available: http://www.defense.gov/releases/release.aspx?releaseid=16547

[3] "Electromagnetic Spectrum Strategy," Tech. Rep., 2013. [Online]. Available: http://www.defense.gov/news/dodspectrumstrategy.pdf

[4] D. Bickel and W. H. Hensley, "Design, Theory, and Applications of Interferometric Synthetic Aperture Radar for Topographic Mapping," Tech. Rep. SAND96-1092, 1996.

[5] L. M. H. Ulander and P.-O. Forlind, "Precision processing of CARABAS HF/VHF-band SAR data," in *Geoscience and Remote Sensing Symposium, 1999. IGARSS '99 Proceedings. IEEE 1999 International*, vol. 1, 1999, pp. 47–49 vol.1.

[6] A. Golden Jr, S. A. Werness, M. A. Stuff, S. R. DeGraaf, and R. C. Sullivan Jr, "Radio frequency interference removal in a VHF/UHF deramp SAR," in *SPIE's 1995 Symposium on OE/Aerospace Sensing and Dual Use Photonics*. International Society for Optics and Photonics, 1995, pp. 84–95.

[7] T. Koutsoudis and L. A. Lovas, "RF interference suppression in ultrawideband radar receivers," in *SPIE's 1995 Symposium on OE/Aerospace Sensing and Dual Use Photonics*. International Society for Optics and Photonics, 1995, pp. 107–118.

[8] M. A. Richards, *Fundamentals of Radar Signal Processing*. McGraw Hill Professional, Jun. 2005.

[9] C. V. Jakowatz, *Spotlight-Mode Synthetic Aperture Radar: A Signal Processing Approach*. Springer, Jan. 1996.

[10] W. G. Carrara, R. S. Goodman, and R. M. Majewski, *Spotlight Synthetic Aperture Radar: Signal Processing Algorithms*. Artech House, Incorporated, Jan. 1995.

[11] A. W. Doerry, "Wavefront curvature limitations and compensation to polar format processing for synthetic aperture radar images," Sandia National Laboratories, Tech. Rep., 2007.

[12] N. Levanon and E. Mozeson, *Radar Signals*. John Wiley & Sons, Sep. 2004.

[13] D. Wahl, D. A. Yocky, C. V. Jakowatz, P. Thompson, I. Erteza, and N. Doren, "Interesting Aspects of Spotlight-Mode Image Formation for an L/S-Band High-Resolution SAR," in *Proceedings of the Workshop on Synthetic Aperture Radar Technology*, Redstone Arsenal, AL, 2002.

[14] F. Harris, "On the use of windows for harmonic analysis with the discrete Fourier transform," *Proceedings of the IEEE*, vol. 66, no. 1, pp. 51–83, Jan. 1978.

[15] A. W. Doerry, F. M. Dickey, and L. A. Romero, "Windowing functions for SAR data with spectral gaps," in *Proceedings of SPIE*, vol. 5095, 2003, pp. 54–65.

[16] A. Doerry, "Performance Limits for Synthetic Aperture Radar - second edition," Sandia National Laboratories, Tech. Rep. SAND2006-0821, 2006.

[17] D. Bickel, "SAR Image Effects on Coherence and Coherence Estimation," Sandia National Laboratories, Tech. Rep. SAND2014-0369, 2014.

[18] A. W. Doerry, "SAR data collection and processing requirements for high quality coherent change detection," K. I. Ranney and A. W. Doerry, Eds., Apr. 2008, pp. 694 706–694 706–12.

[19] tandemX, "DLR - Institut fr Hochfrequenztechnik und Radarsysteme - TanDEM-X - A New High Resolution Interferometric SAR Mission," 2014. [Online]. Available: http://www.dlr.de/hr/desktopdefault.aspx/tabid-2317/3669_read-5488/

[20] M. Lopez, "RTV Synthetic Aperture Radar – Sandia National Laboratories," Aug. 2014. [Online]. Available: http://www.sandia.gov/radar/rtv.html

[21] F. Meyer, J. Nicoll, and A. Doulgeris, "Correction and Characterization of Radio Frequency Interference Signatures in L-Band Synthetic Aperture Radar Data," *IEEE Transactions on Geoscience and Remote Sensing*, vol. 51, no. 10, pp. 4961–4972, 2013.

[22] B. H. Ferrell, "Interference suppression in UHF synthetic aperture radar," in *SPIE's 1995 Symposium on OE/Aerospace Sensing and Dual Use Photonics*. International Society for Optics and Photonics, 1995, pp. 96–106.

[23] M. Braunstein, J. M. Ralston, and D. A. Sparrow, "Signal processing approaches to radio frequency interference (RFI) suppression," vol. 2230, 1994, pp. 190–208.

[24] T. Miller, L. Potter, and J. McCorkle, "RFI suppression for ultra wideband radar," *IEEE Transactions on Aerospace and Electronic Systems*, vol. 33, no. 4, pp. 1142–1156, 1997.

[25] G. Cazzaniga and A. Guarnieri, "Removing RF interferences from P-band airplane SAR data," in *Geoscience and Remote Sensing Symposium, 1996. IGARSS '96. 'Remote Sensing for a Sustainable Future.', International*, vol. 3, May 1996, pp. 1845–1847 vol.3.

[26] X. Huang and D. Liang, "Gradual RELAX algorithm for RFI suppression in UWB-SAR," *Electronics Letters*, vol. 35, no. 22, pp. 1916–1917, 1999.

[27] A. Potsis, A. Reigber, and K. Papathanassiou, "A phase preserving method for RF interference suppression in P-band synthetic aperture radar interferometric data," in *Geoscience and Remote Sensing Symposium, 1999. IGARSS '99 Proceedings. IEEE 1999 International*, vol. 5, 1999, pp. 2655–2657 vol.5.

[28] K. Abend and J. W. McCorkle, "Radio and TV interference extraction for ultrawide-band radar," vol. 2487, 1995, pp. 119–129.

[29] S. DeGraaf, "SAR imaging via modern 2-D spectral estimation methods," *IEEE Transactions on Image Processing*, vol. 7, no. 5, pp. 729–761, May 1998.

[30] D. Andre, "Sidelobe rotation and apodization," in *2006 IEEE Conference on Radar*, Apr. 2006, pp. 5 pp.–.

[31] H. Stankwitz, R. J. Dallaire, and J. Fienup, "Nonlinear apodization for sidelobe control in SAR imagery," *IEEE Transactions on Aerospace and Electronic Systems*, vol. 31, no. 1, pp. 267–279, 1995.

[32] S. DeGraaf, "Sidelobe reduction via adaptive FIR filtering in SAR imagery," *IEEE Transactions on Image Processing*, vol. 3, no. 3, pp. 292–301, May 1994.

[33] A. W. Doerry, "Apodized RFI Filtering of Synthetic Aperture Radar Images," Sandia National Laboratories, Tech. Rep., 2014.

[34] J. Tsao and B. Steinberg, "Reduction of sidelobe and speckle artifacts in microwave imaging: the CLEAN technique," *IEEE Transactions on Antennas and Propagation*, vol. 36, no. 4, pp. 543–556, Apr. 1988.

[35] L. Nguyen and T. Tran, "Robust and adaptive extraction of RFI signals from ultra-wideband radar data," in *Geoscience and Remote Sensing Symposium (IGARSS), 2012 IEEE International*, 2012, pp. 7137–7140.

[36] C. Le, S. Hensley, and E. Chapin, "Adaptive filtering of RFI in wideband SAR signals," in *Seventh Airborne Geoscience Workshop*, 1998.

[37] X. Luo, L. M. H. Ulander, J. Askne, G. Smith, and P.-O. Frolind, "RFI suppression in ultra-wideband SAR systems using LMS filters in frequency domain," *Electronics Letters*, vol. 37, no. 4, pp. 241–243, 2001.

[38] V.-T. Vu, T. Sjogren, M. Pettersson, L. Hkansson, A. Gustavsson, and L. M. H. Ulander, "RFI Suppression in Ultrawideband SAR Using an Adaptive Line Enhancer," *IEEE Geoscience and Remote Sensing Letters*, vol. 7, no. 4, pp. 694–698, 2010.

[39] F. U. Khan, "RFI Suppression in Low Frequency UWB SAR Using the RLS Algorithm," Ph.D. dissertation, Blekinge Institute of Technology, 2010.

[40] T. Lamont-Smith, R. D. Hill, S. D. Hayward, G. Yates, and A. Blake, "Filtering approaches for interference suppression in low-frequency SAR," *Radar, Sonar and Navigation, IEE Proceedings* -, vol. 153, no. 4, pp. 338–344, Aug. 2006.

[41] S. Haykin, *Adaptive Filter Theory*. Prentice Hall, 1986.

[42] S. Buckreuss and R. Horn, "E-SAR P-band SAR subsystem design and RF-interference suppression," in *Geoscience and Remote Sensing Symposium Proceedings, 1998. IGARSS '98. 1998 IEEE International*, vol. 1, Jul. 1998, pp. 466–468 vol.1.

[43] A. Reigber and A. Ulbricht, "P-band repeat-pass interferometry with the DLR experimental SAR (ESAR): first results," in *Geoscience and Remote Sensing Symposium Proceedings, 1998. IGARSS '98. 1998 IEEE International*, vol. 4, 1998, pp. 1914–1916 vol.4.

[44] M. Davis, "Frequency allocation challenges for ultra-wideband radars," *IEEE Aerospace and Electronic Systems Magazine*, vol. 28, no. 7, pp. 12–18, 2013.

[45] R. Hanssen and R. Bamler, "Evaluation of interpolation kernels for SAR interferometry," *IEEE Transactions on Geoscience and Remote Sensing*, vol. 37, no. 1, pp. 318–321, Jan. 1999.

[46] H. Zebker and J. Villasenor, "Decorrelation in interferometric radar echoes," *IEEE Transactions on Geoscience and Remote Sensing*, vol. 30, no. 5, pp. 950–959, 1992.

[47] M. Preiss, D. Gray, and N. J. S. Stacy, "Detecting scene changes using synthetic aperture Radar interferometry," *IEEE Transactions on Geoscience and Remote Sensing*, vol. 44, no. 8, pp. 2041–2054, 2006.

[48] D. Bickel, "Preliminary note on receiver operating characteristics for CCD," Jan. 2015.

[49] G. Carter, C. Knapp, and A. H. Nuttall, "Estimation of the magnitude-squared coherence function via overlapped fast Fourier transform processing," *IEEE Transactions on Audio and Electroacoustics*, vol. 21, no. 4, pp. 337–344, Aug. 1973.

[50] R. A. Fisher, "The General Sampling Distribution of the Multiple Correlation Coefficient," *Proceedings of the Royal Society of London A: Mathematical, Physical and Engineering Sciences*, vol. 121, no. 788, pp. 654–673, Dec. 1928.

[51] M. Abramowitz and I. A. Stegun, *Handbook of Mathematical Functions: with Formulas, Graphs, and Mathematical Tables*. Dover, 1970.

[52] G. Zhu, Z. Yuan, F. He, and X. Huang, "RFI suppression method based on amplitude equalization in ultra-wide band through-wall radar," in *2012 International Conference on Microwave and Millimeter Wave Technology (ICMMT)*, vol. 4, 2012, pp. 1–4.

[53] C. Fan, X.-T. Huang, T. Jin, J.-G. Yang, and D. X. An, "Novel pre-processing techniques for coherence improving in along-track dual-channel low frequency SAR," *Progress In Electromagnetics Research*, vol. 128, pp. 171–193, 2012.

[54] F. M. Dickey, L. A. Romero, and A. W. Doerry, "Window functions for imaging radar: a maximum energy approach to contiguous and notched spectrums," *Optical Engineering*, vol. 42, no. 7, pp. 2113–2128, 2003.

[55] P. H. Eichel, D. Ghiglia, C. Jakowatz, P. Thompson, and D. Wahl, "Interferometric Processing of Coherent Spotlight Mode SAR Images," in *Proceedings of the Interferometric SAR Technology and Applications Symposium*, Ft. Belvoir, VA, Apr. 1993, pp. 253–274.

VITA

Cameron H. Musgrove

Candidate for the Degree of

Doctor of Philosophy

Dissertation: INTERFERENCE MITIGATION EFFECTS ON SYNTHETIC APERTURE RADAR COHERENT DATA PRODUCTS

Major Field: Electrical Engineering

Biographical:

Publications:

C. Musgrove and J. West, "Application of equalization notch to improve synthetic aperture radar coherent data products," Proc. of SPIE Vol. 9461A, 2015.
C. Musgrove, R. Naething, and J. Schilling, "Arbitrary scene simulation for synthetic aperture radar," Proc. of SPIE Vol. 9077, 2014.
C. Musgrove and R. Naething, "A method to evaulate residual phase error for polar formatted synthetic aperture radar systems," Proc. of SPIE Vol. 8714, 2013.

Experience:

Sandia National Laboratories, Albuquerque, NM from 2008 to present.
Discover and create methods to improve synthetic aperture radar image products and data collection modes.

Education:

Doctor of Philosophy in Electrical Engineering at Oklahoma State University in July, 2015.
Master of Science in Electrical Engineering at Oklahoma State University in December, 2007.
Bachelor of Science in Electrical Engineering at Oklahoma State University in December, 2005.

Professional Memberships: SPIE and IEEE.